Final Report

INNOVATIVE SENSOR FOR PIPELINE CRAWLERS: ROTATING PERMANENT MAGNET INSPECTION

To

DEPARTMENT OF ENERGY

NATIONAL ENERGY

TECHNOLOGY LABORATORY

And

PIPELINE RESEARCH

COUNCIL INTERNATIONAL, INC

December 2006

INNOVATIVE SENSORS FOR PIPELINE CRAWLERS: ROTATING PERMANENT MAGNET INSPECTION

Final Report

Reporting Period Start Date: October 1, 2003
Reporting Period End Date: September 30, 2006

Principal Authors: J. Bruce Nestleroth, Richard J. Davis, and Stephanie Flamberg

Report Issued: December 2006

DEPARTMENT OF ENERGY
NATIONAL ENERGY TECHNOLOGY LABORATORY
Contract No. DE-FC26-03NT41881
Battelle No. G004858

And

PIPELINE RESEARCH COUNCIL INTERNATIONAL, INC
Contract No. PR-003-03155
Battelle No. N006116

BATTELLE
505 King Avenue
Columbus, Ohio 43201-2693

Table of Contents

Page

Table of Contents (continued)

Page

List of Figures

Table of Contents (continued)

Page

Table of Contents (continued)

Page

List of Tables

ABSTRACT

Internal inspection of pipelines is an important tool for ensuring safe and reliable delivery of fossil energy products. Current inspection systems that are propelled through the pipeline by the product flow cannot be used to inspect all pipelines because of the various physical barriers they may encounter. To facilitate inspection of these "unpiggable" pipelines, recent inspection development efforts have focused on a new generation of powered inspection platforms that are able to crawl slowly inside a pipeline and can maneuver past the physical barriers that limit internal inspection applicability, such as bore restrictions, low product flow rate, and low pressure.

The first step in this research was to review existing inspection technologies for applicability and compatibility with crawler systems. Most existing inspection technologies, including magnetic flux leakage and ultrasonic methods, had significant implementation limitations including mass, physical size, inspection energy coupling requirements and technology maturity. The remote field technique was the most promising but power consumption was high and anomaly signals were low requiring sensitive detectors and electronics. After reviewing each inspection technology, it was decided to investigate the potential for a new inspection method.

The new inspection method takes advantage of advances in permanent magnet strength, along with their wide availability and low cost. Called rotating permanent magnet inspection (RPMI), this patent pending technology employs pairs of permanent magnets rotating around the central axis of a cylinder to induce high current densities in the material under inspection. Anomalies and wall thickness variations are detected with an array of sensors that measure local changes in the magnetic field produced by the induced current flowing in the material. This inspection method is an alternative to the common concentric coil remote field technique that induces low-frequency eddy currents in ferromagnetic pipes and tubes.

Since this is a new inspection method, both theory and experiment were used to determine fundamental capabilities and limitations. Fundamental finite element modeling analysis and experimental investigations performed during this development have led to the derivation of a first order analytical equation for designing rotating magnetizers to induce current and positioning sensors to record signals from anomalies. Experimental results confirm the analytical equation and the finite element calculations provide a firm basis for the design of RPMI systems.

Experimental results have shown that metal loss anomalies and wall thickness variations can be detected with an array of sensors that measure local changes in the magnetic field produced by the induced current flowing in the material. The design exploits the phenomenon that circumferential currents are easily detectable at distances well away from the magnets. Current changes at anomalies were detectable with commercial low cost Hall Effect sensors. Commercial analog to digital converters can be used to measure the sensor output and data analysis can be performed in real time using PC computer systems. The technology was successfully demonstrated during two blind benchmark tests where numerous metal loss defects were detected. For this inspection technology, the detection threshold is a function of wall thickness and corrosion depth. For thinner materials, the detection threshold was experimentally

shown to be comparable to magnetic flux leakage. For wall thicknesses greater than three tenths of an inch, the detection threshold increases with wall thickness. The potential for metal loss anomaly sizing was demonstrated in the second benchmarking study, again with accuracy comparable to existing magnetic flux leakage technologies.

The rotating permanent magnet system has the potential for inspecting unpiggable pipelines since the magnetizer configurations can be sufficiently small with respect to the bore of the pipe to pass obstructions that limit the application of many inspection technologies. Also, since the largest dimension of the Hall Effect sensor is two tenths of an inch, the sensor packages can be small, flexible and light. The power consumption, on the order of ten watts, is low compared to some inspection systems; this would enable autonomous systems to inspect longer distances between charges.

This project showed there are no technical barriers to building a field ready unit that can pass through narrow obstructions, such as plug valves. The next step in project implementation is to build a field ready unit that can begin to establish optimal performance capabilities including detection thresholds, sizing capability, and wall thickness limitations.

1 Introduction

Internal inspection of pipelines is an important tool for ensuring safe and reliable delivery of fossil energy products. Current inspection systems that are propelled through the pipeline by the product flow cannot be used to inspect all pipelines because of the various physical barriers they may encounter. To facilitate inspection of these "unpiggable" pipelines, recent inspection development efforts have focused on a new generation of powered inspection platforms that are able to crawl slowly inside a pipeline and can maneuver past the physical barriers that limit internal inspection applicability, such as bore restrictions, low product flow rate, and low pressure.

In this project, a new inspection method was developed. This patent pending technology, called rotating permanent magnet inspection (RPMI), employs pairs of permanent magnets rotating around the central axis of a cylinder to induce high current densities in the material under inspection. Anomalies and wall thickness variations are detected with an array of sensors that measure local changes in the magnetic field produced by the induced current flowing in the material. This inspection method is an alternative to the common concentric coil remote field technique that induces low-frequency eddy currents in ferromagnetic pipes and tubes. This electromagnetic technology is being developed for pipeline inspection platforms that crawl slowly inside a pipe to maneuver past physical barriers that limit inspection using existing technologies. These devices move down the pipeline independent of the product flow, and potentially stop for detailed defect assessment.

This report starts with a review of existing inspection technology for applicability and compatibility with crawler systems. Most existing inspection technologies, including magnetic flux leakage and ultrasonic methods, had significant implementation limitations including mass, physical sizing, inspection energy coupling requirements and technology maturity. The remote field technique was the most promising but power consumption was high and anomaly signals were low requiring sensitive detectors and electronics. After reviewing each inspection technology, it was decided to investigate the potential for a new inspection method.

The report continues with a description of the results attained in the development of the RPMI method. Since this is a new inspection method, both theory and experiment were used to determine fundamental capabilities and limitations. Fundamental finite element modeling analysis and experimental investigations performed during this development have led to the derivation of a first order analytical equation for designing rotating exciters and positioning sensors. Experimental results confirm the analytical equation and the finite element calculations provide a firm basis for the design of RPMI systems. Experiments have demonstrated that this inspection method has the potential for detecting and sizing metal loss corrosion. In addition, the rotating permanent magnet design allows for the potentially broader application of inspecting "unpiggable" pipelines because the sensor configurations can be small in physical size. Many laboratory prototypes were built to develop the RPMI method. The final section of the report describes the initial design and subsequent fabrication of a working rotating magnet prototype that can collapse to a third of the inspection diameter.

2 Applicability of Established Pipeline Inspection Technologies to Crawlers

To detect problems prior to incidents, inspection equipment is required to interrogate the energy pipeline infrastructure for degradation mechanisms. In-line inspection equipment is commonly used to perform these inspections because they can examine large portions of pipeline systems in a relatively short amount of time. However, these technologies have had a limited amount of commercial success for inspecting the shorter runs of distribution pipe and pipelines with severe restrictions primarily because of:

- Sensors that are too large and/or heavy to negotiate common obstructions and constraints
- Inspection systems often require more power than can be practically carried by an inspection vehicle
- Low pipeline pressures and flows that necessitate means other than product flow to propel the inspection vehicle through the pipeline
- Conditions that make inspection of these pipelines unique, thus eliminating the economies of scale.

The following sections provide a review of pipeline inspection sensors and their applicability for crawler systems.

2.1 Inspection Technologies for Pipelines

In-line inspection of pipelines is commercially performed using magnetic and ultrasonic methods. The basic principles, attributes, and limitations of these inspection methods are summarized in the following sections.

2.1.1 Magnetic Flux Leakage

Magnetic flux leakage (MFL) was first commercially used to inspect pipelines in 1964. Today it is the most commonly used in-line inspection method [1,2] for pipelines. MFL technology can successfully overcome the physical and practical inspection challenges presented by transmission pipelines. The systems can be designed to remain functional in an abusive pipeline environment for long distances and at product flow speeds. The permanent magnets used in this inspection technology need no energy source during an inspection, and the sensors and data recorders require reasonably low power to operate. The magnetic flux naturally enters the pipe material and distributes evenly to produce a full volumetric inspection. Often corrosion anomaly detection and sizing limitations of MFL systems are highlighted, but the attributes described above keep MFL at the forefront of pipeline inspection technologies. There are two widely used implementations of MFL that can be differentiated by the orientation of the magnetization in terms of axial or circumferential direction. These implementations are discussed further in the subsequent sections.

2.1.1.1 Axial MFL

Axial MFL is the oldest and still the most common implementation of the MFL inspection method. The term axial, describing the orientation of the magnetizing field as illustrated in Figure 1, was added only after other implementations, such as circumferential MFL, were

developed. The phrase MFL tool when used alone almost always refers to the axial implementation.

Axial MFL tools are most sensitive to volumetric or metal-loss defects with a significant circumferential extent or width. They are much less sensitive to cracks and axially oriented metal loss. Most axial MFL tools magnetically saturate the pipe wall to reduce the effects of material variations and stress on the signal. As a result, the tools are less sensitive to defects in which the most significant characteristic is a change in material or magnetic properties (e.g., hard spots and microstructural damage near gouges). Nearly all axial MFL systems provide uniform magnetic fields at each sensor around the pipe. This approach, when combined with high magnetization strength, minimizes signal conditioning and compensation requirements in the analysis process.

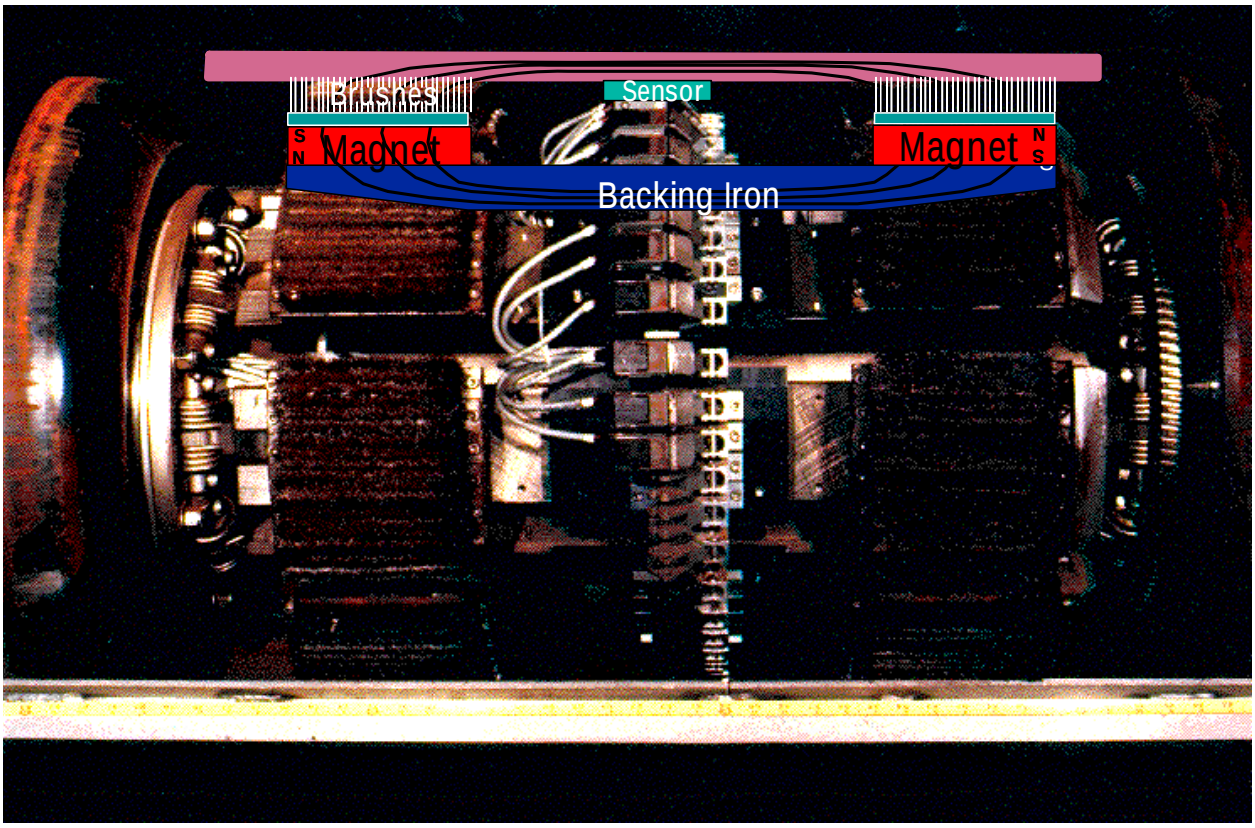

Figure 1. An axial MFL magnetizer

Some early axial MFL systems used electromagnets for magnetization, but most tools now use very strong permanent magnets. Nearly all current axial MFL systems have the capability to magnetically saturate the pipe at wall thicknesses on the order of 30 mm (1.2 inches) in pipe diameters greater than 24 inches – above this wall thickness, the inspection results are less accurate. For smaller diameters, the space available for the magnets is constrained; consequently, less magnetization force can be carried. As a result, the inspection results are more sensitive to wall thickness.

Most MFL systems use steel brushes to couple the magnetic energy into the pipe and provide flexibility at intrusions into the internal diameter, such as a weld drop-through. The brushes enable an MFL tool to pass through a pipe that has a local deformation (e.g., dent) of up to 10 percent of the pipe diameter. Reduced port valves, severe dents and other restrictions are problematic for MFL tools because they can create restrictions that will cause the tool to become stuck. An additional limitation of MFL tools is that the magnetic holding forces and friction caused by the brushes can significantly increase propulsion requirements.

Many axial MFL inspection systems are advertised as high resolution. Early axial MFL systems stored data on modified 24-channel audio tape recording equipment. High resolution was initially defined as indicating the use of more sensors than on one of these early systems. A more scientific definition involves the circumferential extent of defects to be sized. Applying the Nyquist sampling theorem to the flux leakage from small pit defects, the circumferential sensor spacing must be less than half the circumferential extent of the pit to be assessed. Wall thickness also affects minimum spacing. For example, pits less than two times the wall thickness are more difficult to size, regardless of the number of sensors used. For defects with a diameter less than the wall thickness, most of the flux spreads circumferentially around the defect rather than leaking from the pipe, making detection difficult.

For high-resolution axial MFL tools, there is a theoretical minimum sensor spacing for most applications that is on the order of the wall thickness. Since the tools must cover a range of wall thicknesses, a practical definition of sensor spacing for a high-resolution tool is between 6 and 12 mm (0.25 to 0.5 inch). Circumferential sensor spacing closer than 6 mm (0.25 inch) does not provide a significant advantage in metal-loss defect sizing, although it does improve the ability to detect some pinhole and crack-like defects. The distance between measurements in the axial direction can be much less, and is governed by the minimum axial length that the tool must detect and size. Typical measurement spacing is between 2.5 to 5 mm (0.1 to 0.2 inches).

MFL sensors measure one component of the flux leakage field at a point, but flux leakage is a vector quantity with three directional components. Most axial MFL tools measure only the axial component (for circumferential MFL, the circumferential component is commonly measured). The other components (radial and circumferential for axial tools) can provide some additional information that can be useful for sizing. The information from each component is somewhat correlated; in experiments on patch corrosion defects at Battelle's Pipeline Simulation Facility, the information content in two sensor components was found to be about twenty percent larger than that in one component. Thus, a modest increase in sizing accuracy is possible with tools that measure more than one component of the flux leakage field.

The velocity of an axial MFL tool through a pipeline significantly affects defect signals at speeds over 2.5 m/s (5.6 mph) in 12-inch diameter pipe (inspection speed affects nearly all electromagnetic inspection methodologies). These effects are reported to be manageable for larger diameter tools at speeds up to 4 m/s (9 mph). Below these speeds, velocity effects are small, making sizing and detection easier. Some tools have a minimum acceptable speed on the order of 1.0 m/s (2.2 mph), because of sensor configuration; a coil sensor output is directly proportional to velocity. A second velocity effect is due to low pressure; below about 27.5 bar (400 psi), the gas column act like a weak spring and significant variations in velocity are

common as the tool stops and starts during the run. At higher pressures, the gas column is stiffer allowing more uniform inspection velocity

Axial MFL tools are best suited for volumetric metal-loss defects with a width greater than two wall thicknesses. Axial MFL tools can detect 95 percent of corrosion defects that are greater than 10 percent of the wall thickness. The sizing accuracy is generally specified as +/- 10 percent of the wall thickness with a confidence of 80 percent. Axially aligned defects and deeper defects are not sized as accurately because the flux spreads around the defect rather than leaking from the pipe walls. Axial MFL tools generally have the same performance capability for pipe diameters greater than about 300 mm (12 inches) and at speeds up to 4 m/s (9 mph). Axial MFL tools are available for smaller pipeline diameters, as small as 100 mm (4 inches), with reduced performance capabilities. Generally, these tools perform best at velocities below 2.5 m/s (5.6 mph).

2.1.1.2 Circumferential MFL

Circumferential MFL is a new twist on an old technology. Longitudinal defects, such as SCC, longitudinal corrosion, long seam defects, and axially oriented mechanical damage, are of significant concern to the pipeline industry. These defects tend to increase stress levels in the remaining pipe material. To improve detection and sizing of longitudinal defects, the orientation of the magnetic field was changed from the traditional axial direction to circumferential, as illustrated in Figure 2. As a result, circumferential MFL tools are most sensitive to defects with a significant axial length. They are somewhat sensitive to axially aligned cracks and not sensitive to circumferentially aligned cracks.

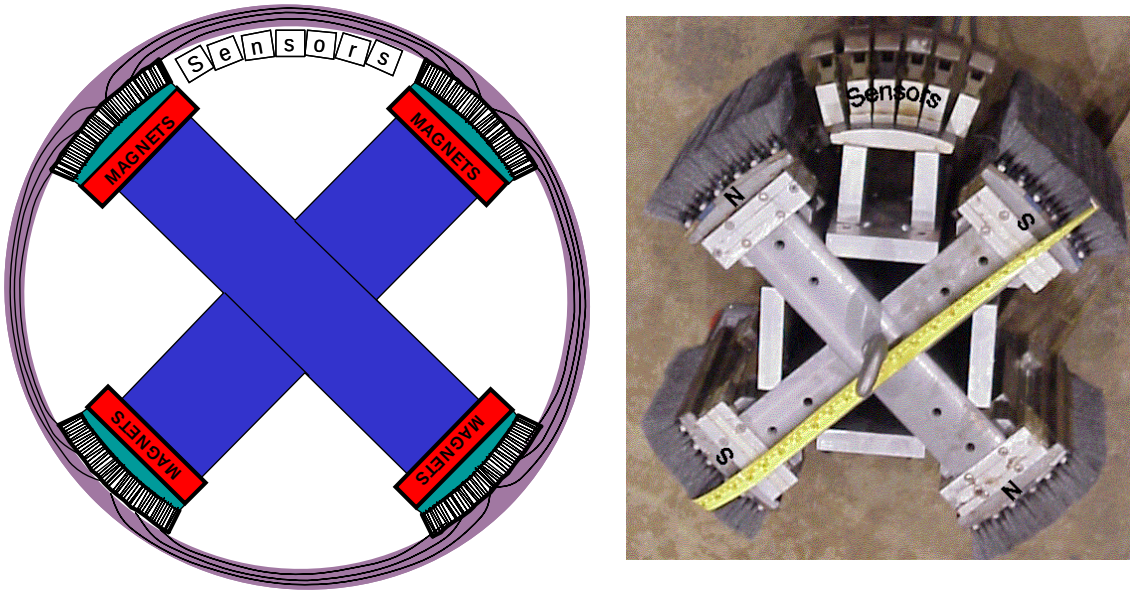

Figure 2. A circumferential MFL magnetizer

Magnetization levels vary significantly with circumferential MFL tools because it is much more difficult to saturate the pipe material in the circumferential direction. The magnetic field strength

is greatest near the magnetizer poles and smallest at the center. The lack of uniformity on the magnetic field makes defect sizing more difficult. A defect near one magnetic pole gives a signal that is different from the signal of the same defect when it is equidistant from the magnet poles. Consequently, compensation methods are used to adjust signal amplitudes and account for the varying magnetic field. This compensation adds a significant amount of complexity to defect detection and analysis procedures. For defects that span one or more poles, compensation methods may mask the defect signal, resulting in a false negative or undersizing of a potentially critical defect.

Velocity effects for circumferential MFL are detectable at much lower speeds and are more significant than for axial MFL. Velocity-induced signal changes can be detected at speeds of 1.0 m/s (2.2 mph). Above this velocity and for defects midway between the poles, the signal amplitude is reduced and compensation for velocity is possible. If the defect is closer to one pole, however, the flux leakage is also distorted, making sizing much more difficult. As velocity increases, the magnetizing field also starts to concentrate at the inner surface of the pipe (i.e., it varies through the thickness as well as around the circumference). This effect also makes sizing and detection of outside-diameter defects more difficult.

More sensors are needed for circumferential MFL than axial MFL to achieve similar accuracies. For circumferential MFL, the flux spreads in the axial direction, which helps reduce the axial sample interval but not the sensor spacing requirements. Therefore, to accurately record the flux leakage, the sensor spacing interval around the pipe is half that of axial MFL, typically between 2.5 to 5 mm (0.1 to 0.2 inch). For example, an axial tool with 250 sensors would have the same flux recording fidelity as a circumferential tool with 500 sensors. The sampling requirement along the pipe (in the axial direction) is helped by flux spreading, but most implementations stay with the same data interval as axial MFL to simplify data display, analysis, and overlay.

As for axial MFL, the manner in which the depth of a defect affects circumferential MFL signals changes with increasing depth. These effects are more significant and begin at shallower depths with circumferential MFL than with axial MFL, strongly affecting sizing accuracy. As a result, circumferential MFL tools are not as accurate at sizing defects as axial MFL tools. The sizing accuracy is generally specified as +/- 15 percent of the wall thickness with a confidence of 80 percent.

2.1.1.3 Propelling MFL Tools

MFL tools are propelled by the product flow. Cups that seal against the pipe wall prevent product from flowing around a tool. As additional product is pumped into the pipe behind the tool, a differential pressure is established. When the differential pressure times the area of the tool is sufficient to overcome the weight and frictional forces, the tool is propelled down the pipeline. Typically, it requires a differential pressure of about 15 to 25 pounds to overcome friction and initiate motion, and 5 to 15 pounds to maintain a consistent velocity. The average speed of the tool is defined by the flow rate. The uniformity in liquid pipelines is excellent since the product is essentially noncompressible; however, in gas pipelines the speed can vary significantly and is dependent on the pressure in the pipe. Higher pressures dampen the velocity excursions.

A 24-inch diameter MFL tool can weigh more than 2400 pounds, about the weight of a compact car. The weight of the MFL tool increases with pipe diameter, as shown in Figure 3. However, the driving force not including friction (the weight divided by the cross sectional area), also shown in Figure 3, is between 4 and 7 pounds per square inch, nearly independent of pipe diameter. Friction at least doubles the driving force requirements. Because of these high formal requirements, differential pressure is clearly an efficient way to propel MFL tools in a pipeline.

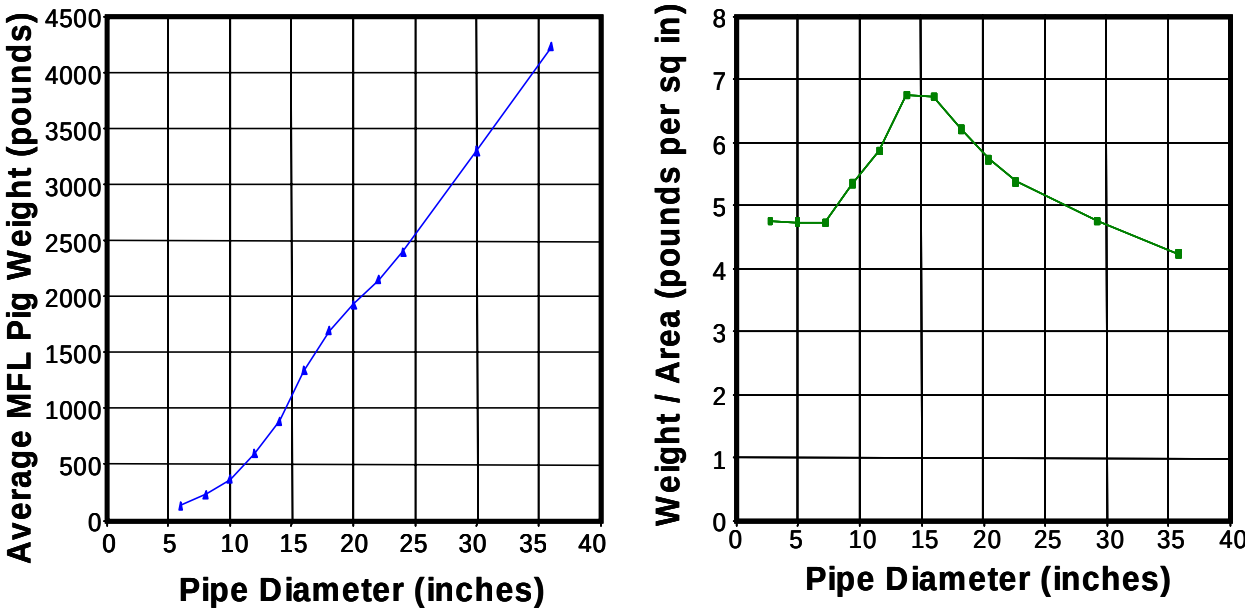

Figure 3. The weight and propelling force requirements for MFL tools

2.1.2 Ultrasonic Inspection Technology

Ultrasonic testing (UT) can be used to measure the wall thickness of pipe to detect corrosion. In another implementation it can detect cracks [3]. The basics of each technology are discussed next.

2.1.2.1 Wall Thickness Measurement

High frequency sound waves have been employed to inspect pipelines from the inside since the mid 1980s [4,5]. The basic principle, illustrated in Figure 4, is similar to handheld ultrasonic equipment used to measure wall thickness and detect cracks. Pulses of ultrasonic energy between 1 and 10 MHz are launched from a piezoelectric transducer. These pulses are reflected by the inside and outside surface of the pipe. By measuring the time between the reflections and knowing the speed of sound in steel pipe (nearly constant for most pipes), it is possible to establish the thickness of the pipe.

The industry standard thickness measurement accuracy for handheld ultrasonic thickness gauges is nominally 0.001 inch (0.025 mm). These gauges use high-frequency transducers with multiple elements and signal averaging to reduce noise. Because of the speed of the product flow, in-line inspection tools use a single signal to assess thickness. They also use lower frequency

transducers (around 5 MHz) to overcome surface roughness challenges. The typical accuracy of an in-line inspection tool is 0.020 inch (0.5 mm).

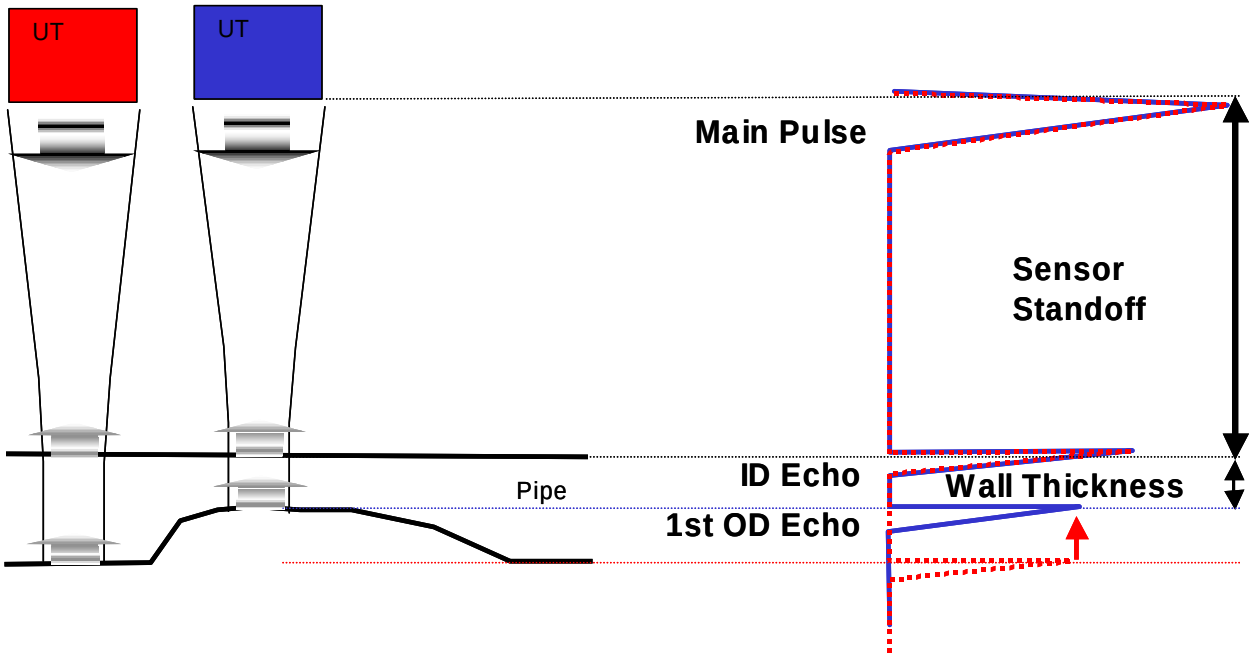

Figure 4. The pulse echo ultrasonic method for measuring wall thickness

While the ultrasonic technique provides sufficient accuracy for assessment of defects, the practical use of this technology is limited. The ultrasonic method requires a liquid to couple the ultrasonic energy from the transducer to the pipe and back. While this is practical for oil and liquid products pipelines, application in gas lines is not as simple. Filling a gas pipeline with a slug of liquid is rarely practical. Also the ultrasonic tools employ a large number of sensors, on the order of 10 per diameter inch. Historically, data processing and storage time have limited the speed of the inspection to around 3.0 mph; however, recent developments in electronics have increased inspection speed capability.

While the wall thickness measurements are accurate in noise free pipe, distinguishing corrosion from other reflectors such as laminations and inclusions has caused some problems. Ultrasonic pigs can miss defects behind laminations and small sharp geometries. Also, the pipeline must be extremely clean without any debris or deposits. In general, if a signal can be recorded, an assessment of wall thickness can be made. Unlike MFL tools, depth accuracies are not a function of wall thickness; thus, errors are expressed in length units, not in percent. To summarize the differences in the two technologies, MFL tools reliably generate signals from metal loss defects but interpretation is often difficult; ultrasonic signals are simple to interpret but attaining a signal is difficult because of the many inspection variables.

2.1.2.2 Ultrasonic Crack Detection

Some attempts have been made to detect cracks using ultrasonic inspection techniques; these differ primarily in the way the ultrasonic energy enters the pipe. Liquid coupled methods, wheel

coupled methods, and electromagnetic acoustic transducers have proven capable of detecting longitudinal cracks, but they all have limitations.

GE-PII developed the first angle-beam ultrasonic tool in the 1970s, and the tool has seen some use in operating pipelines. The tool uses liquid-filled wheels, illustrated in Figure 5, to allow ultrasonic energy to be coupled into the pipe wall of gas-filled lines. The number of sensors is limited by the number of wheels, and sophisticated signal processing is needed to detect and characterize cracks. Generally, the tool has proven effective at detecting and sizing some cracks and crack colonies. Questions about its ability to discriminate between crack signals and non-crack signals remain. In addition, reliable estimates of probabilities of detection and sizing accuracies are not available.

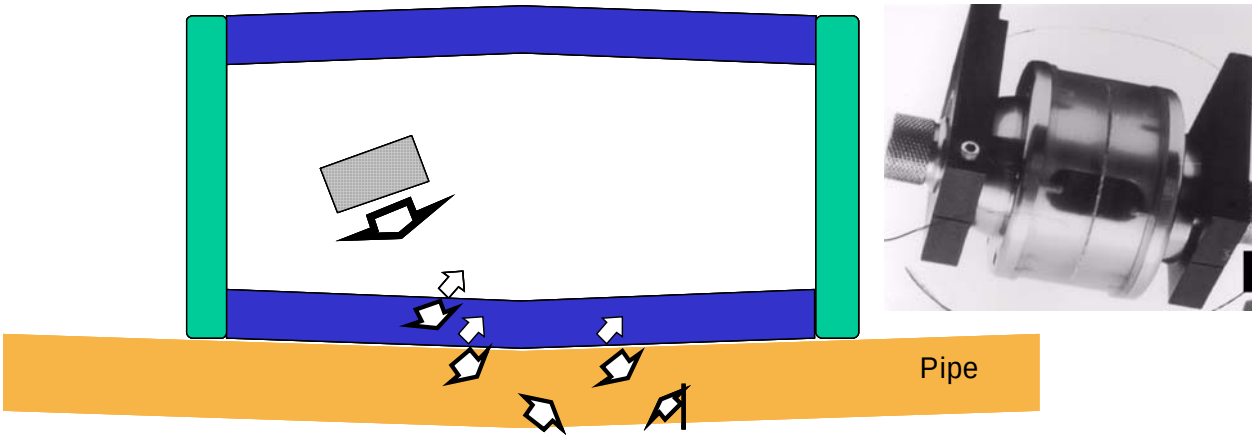

Figure 5. Wheel coupled ultrasonic inspection for cracks in pipelines

Two pipeline inspection companies supply angle-beam ultrasonic tools. These tools, illustrated in Figure 6, operate only in liquid-filled lines. The liquid couples the ultrasonic energy into the pipe wall, negating the need for a wheel. The liquid coupled tool has many more sensors than the wheeled tool, and it is reported to have greater sizing and detection accuracies. Liquid coupled angle beam tools have the same difficulties encountered with wall thickness tools, including speed restrictions and problems distinguishing cracks from laminations and inclusions.

Several attempts have been made to develop a commercial electromagnetic acoustic transducer (EMAT) inspection system for cracks. EMAT is an ultrasonic inspection technique that operates at a lower frequency, typically 200 to 800 KHz, as compared to piezoelectric ultrasonic, which typically operates at a frequency of 1 to 20 MHz. The waves generated by EMATs are bounded by the inner and outer diameter of the pipe. Wave types include

- Raleigh wave — ultrasonic waves bounded by one surface – surface waves
- Lamb waves — ultrasonic waves in bounded medium such as plates
    - Symmetric — both surfaces move in together
    - Antisymmetric — both surfaces move in opposition
- Shear horizontal plate waves.

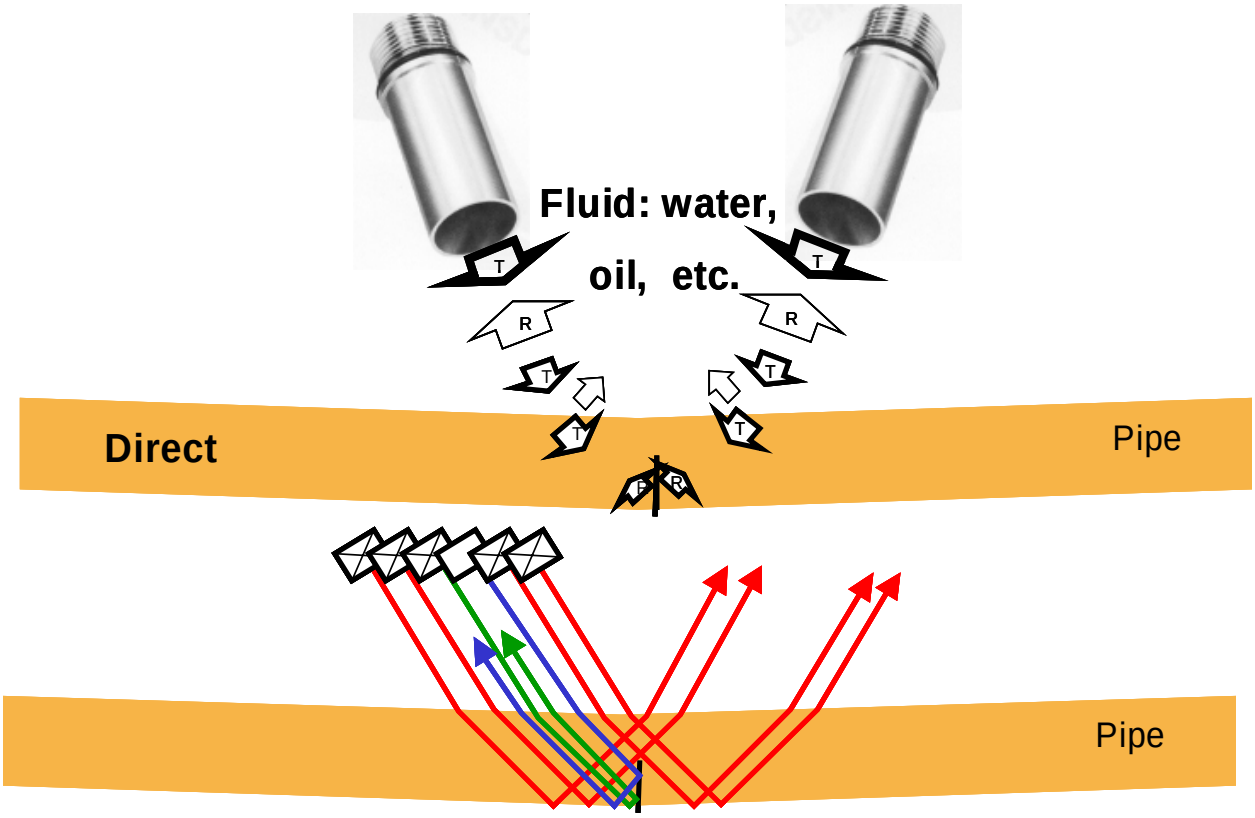

Figure 6. Liquid coupled angle beam inspection for the detection of cracks

Generation of these waves, illustrated in Figure 7, requires a strong static magnetic field and coil that is pulsed to create localized eddy currents in the pipe that oscillate at the designed inspection frequency. The wavelength is defined by the spacing of the meandering coil. The wave mode is dependent on the wall thickness. A change in one variable can cause a different wave type to be launched, which can affect inspection results. The coils have to be near the pipe surface to generate sufficient energy for detection of pipeline defects such as cracks. For long-distance pipeline inspections, the thin polymer covering the coil is worn away by the rough internal surface of the pipe. The primary advantages of EMATS are

- No liquid coupling media required
- Bounded wave propagates in the pipe wall.

Disadvantages of EMATS include

- Implementation challenges
- Wall thickness dependency of sensors
- Many possible modes; different modes provide unique results
- Lower frequency signal than the other techniques can reduce resolution and restrict sizing capability.

Early efforts by the Pipeline Research Council International (PRCI) that were directed at pipeline inspection included work by C.W. Pope in Australia and T.D. Williamson in the United States in the 1980s and 1990s. These efforts were combined in the middle 1990s, and then transferred to Tuboscope in the late 1990s. This tool and other EMAT implementations are under development. Considering all the ultrasonic inspection methods, EMATs have the greatest potential for implementation on crawler systems.

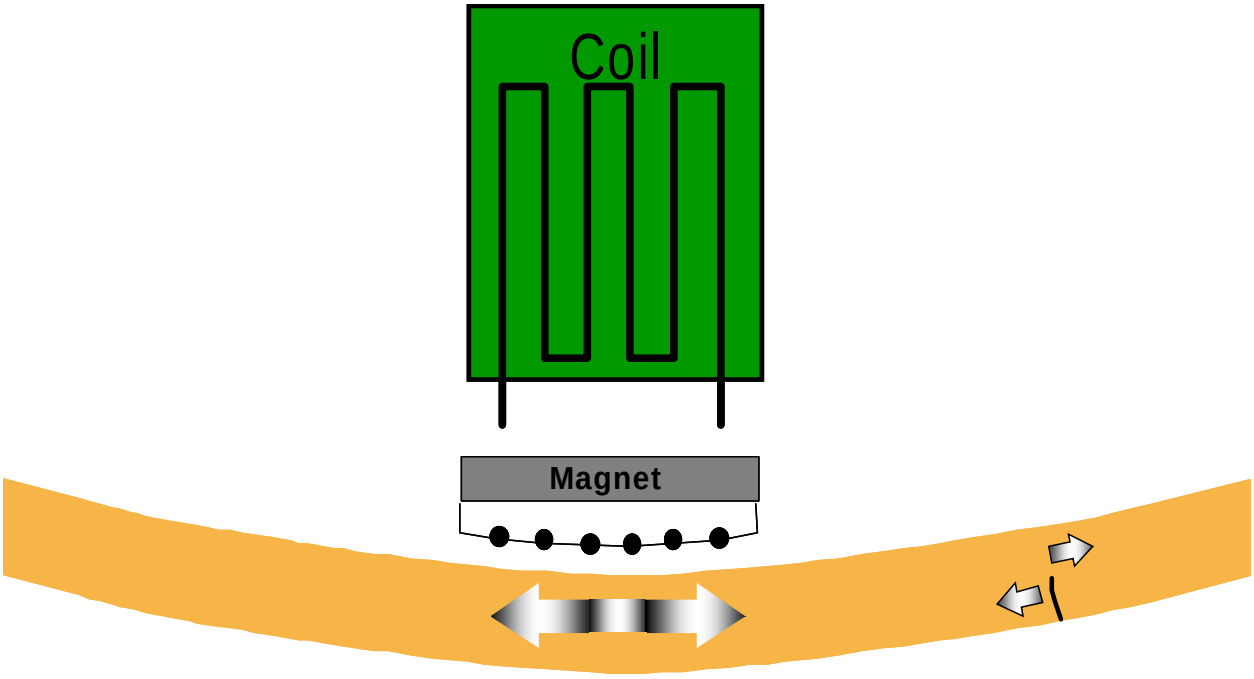

Figure 7. Electromagnetic acoustic transducer inspection for the inspection of pipes for cracks

2.1.3 Remote Field Technique (RFT)

The remote field technique has been used successfully to detect a variety of defect and material conditions in both magnetic and nonmagnetic conductive tubes and pipes [6,7,8]. The remote field eddy current technique uses a sinusoidal current flowing in an exciter coil to induce currents in the pipe and a remote receiver coil over two pipe diameters away to detect defects such as metal loss and stress corrosion cracks. Since the remote field eddy current technique detects signals of known frequencies, sharp filters can be used to detect defect signals while eliminating other sources of electromagnetic noise. Along with detecting stress corrosion cracks, the potential exists for remote field eddy current techniques to detect cracks associated with mechanical damage and to provide additional information for characterizing the severity of the damaged region.

Constraints have been identified that limit the implementation of this inspection technique. Traditional remote field eddy current techniques use low-frequency exciters, which limits the maximum speed at which inspection equipment can travel. Typically, these speeds have been less than one mile per hour, severely limiting potential uses on in-line inspection equipment [7]. Detecting pipeline defects depends on the strength of the eddy currents, which depends on the

excitation frequency and magnetic permeability of the pipe material. The magnetic permeability can be decreased by a strong static magnetic field, similar to the field applied by MFL magnetizers. With the permeability reduced, the signal levels at the sensor will be increased. Alternatively, excitation frequency can be increased for improved inspection speed while keeping signal level constant [9].

A schematic of the remote field eddy current technique is illustrated in Figure 8. An exciter, which is sized to nearly the same diameter as the inside diameter of the pipe, is driven with a low-frequency sinusoidal current. A small magnetic field sensor is positioned some distance away. One portion of the magnetic field generated by the exciter travels down the inside of the pipe, with the field directly coupled to the sensor. A second portion of the alternating magnetic field propagates through the material of the pipe, inducing eddy currents as it goes. Once the magnetic field penetrates the outside wall of the pipe, it spreads along the surface of the pipe and re-enters the pipe, again inducing eddy currents to flow in the pipe material. This second path is referred to as the remote path. The total magnetic field and eddy current flow at any point is the combination of directly coupled and remotely coupled fields.

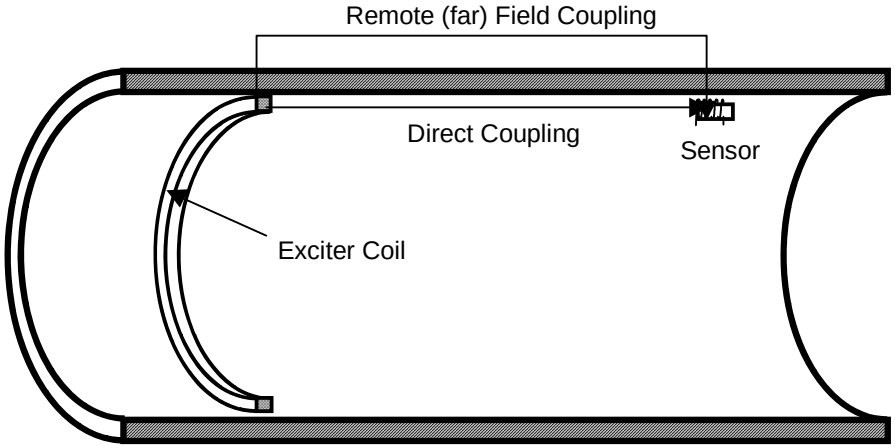

Figure 8. Remote field eddy current exciter and sensor configuration

The key to remote field eddy current testing is to choose a sensor position where the remotely coupled field is large compared with a directly coupled field. This is possible since the directly coupled field decays at a faster rate, as shown in Figure 9. This semi-logarithmic plot shows that the decays of both the remote and direct field are exponential and the decay constant for the direct field is nearly four times as fast as the remote field. Also, the combined magnetic field is less than the direct field in the near field, and it is less than the remote field in the far field. This phenomenon is due to the fact that phase difference for the two paths is always greater than 90 degrees for distances greater than a coil diameter.

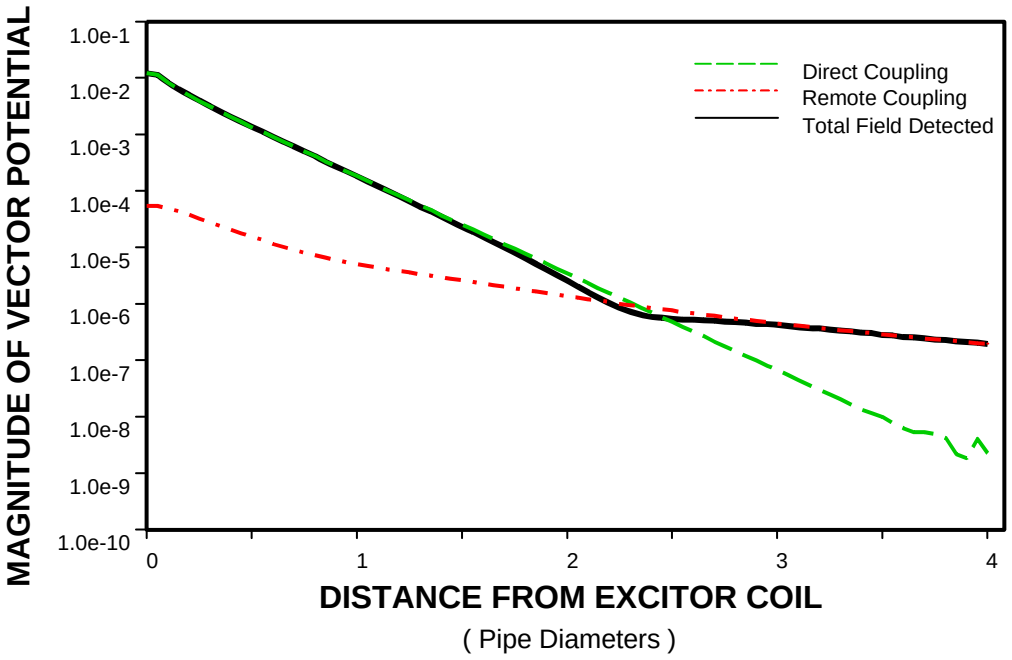

Figure 9. Calculated magnitude of the remote field eddy current effect

2.1.4 Pulsed Eddy Current

Pulsed eddy current inspection has the potential to inspect conductive materials such as pipelines. However, like EMATs, successful implementations of this technology are limited.

Oak Ridge National Laboratory [10] has designed and developed a pulsed magnetic saturation method for the eddy current testing of steel steam generator tubes with a wall thickness of 0.2 inches. It was shown that the current pulse that passes through an electromagnet has sufficient amplitude to saturate the ferromagnetic tube. Defects near the external surfaces can be detected by analyzing the decay of the current pulse. The defect signals can be differentiated from the signal variations that naturally occur in steam generator tubes. Special consideration must be given to the amplitude and duration of the pulse to prevent overheating problems. Peak power levels of 500 kilowatts and duty cycles of 1 millisecond were used to attain results.

A commercial pulsed eddy current instrument is available for inspection of thermally insulated carbon steel components [11, 12]. The instrument measures the wall thickness without any requirement for contact with the steel component itself. The instrument compares the relative decay of eddy currents induced in the pipe to establish wall thickness in pipe up to 1 inch thick. The instrument can work up to 4 inches away from the pipe surface, but requires signal averaging that can take approximately 2 to 5 seconds. Typically used to detect corrosion under insulation and erosion, it can also be applied for measuring wall thickness through coating or scaling.

2.2 Discussion on Established Inspection Technologies

Although several nondestructive in-line inspection technologies are commercially available for assessment of pipeline defects, each method has a significant implementation challenge when applied on crawler systems. Table 1 lists the most significant advantages and disadvantages of each technology with regard to crawler implementation. MFL, the most common technology for pipeline inspection, will have performance reductions for systems designed to pass plug valves and other significant restrictions. To detect shallow metal loss anomalies and size them accurately, MFL systems rely on measuring changes in a uniform magnetic field. Implementations designed to pass obstructions have difficulty achieving a sufficiently uniform magnetic field necessary to achieve performance levels typical of commercial systems used to inspect pipelines without restrictions. The other leading candidate for crawler implementation, the remote field technique, has to carry the electrical power for generating the signal. Power is of particular concern for systems that do not have a tether. Lower power levels for the exciter coil lead to reduced signal levels from defects, which are intrinsically low and require sensitive detectors and low noise amplifiers.

Table 1. Most significant advantages and disadvantages of pipeline inspection technologies as applied to crawler systems.

Technology	Advantage	Disadvantage
MFL	Proven, rugged technology can operate at reasonable product flow speeds.	Heavy with large drag forces. Partial circumference implementation to pass plug valve will have significantly reduced wall thickness measurement accuracy.
Liquid Coupled UT	Most accurate technology for wall thickness.	Not practical in gas lines.
Wheel Coupled UT	Liquid couplings not required. Reasonable wall thickness measurements.	Large sensor heads.
EMATs	Electromagnetic coupling of ultrasonic signal. Sensitive to many defects and conditions.	Many implementations have failed to achieve commercial success. Unproven measurement accuracy.
Remote Field Technique	Can operate at large liftoffs. Reasonable wall thickness measurements. Sensitive to many pipeline defects.	Signal levels small. Significant excitation power needed.
Pulsed Eddy Current	Can operate at large liftoffs.	One commercial system. Significant excitation power needed. Limited wall thickness measurement accuracy.

3 Fundamentals of the Rotating Permanent Magnet Inspection Method

A new method to produce inspection energy in a pipe was developed as an alternative to magnetic flux leakage or the common concentric coil method to induce low-frequency eddy

currents. Pairs of permanent magnets rotating around the central axis of a cylinder can be used to induce high current densities in the material under inspection. Anomalies and wall thickness variations are detected with an array of sensors that measure local changes in the magnetic field produced by the induced current flowing in the material. This electromagnetic technology is being developed for pipeline inspection platforms that crawl slowly inside a pipe to maneuver past physical barriers. These devices move down the pipeline independent of the product flow, and potentially stop for detailed defect assessment. Fundamental finite element modeling analysis and experimental investigations performed during this development have led to the derivation of a first order analytical equation for designing the rotating exciters and positioning sensors.

3.1 Concept of operation

Following the fundamental laws of electrical induction, rotating permanent magnet pairs along the longitudinal axis of a pipe establishes an alternating electrical current in the wall of the pipe. Figure 10, a cutaway drawing showing the rotating permanent magnet exciter, illustrates this concept that has the potential to induce strong eddy currents in the pipe wall. In contrast to traditional eddy current systems which use a coil that is driven by a sinusoidal current, this approach uses alternating N and S poles rotating around a shaft.

The dashed lines in Figure 10 illustrate the current flow as the magnetizer rotates in the pipe. The current flows in an elliptical path around the magnets. When the magnetizer is vertical, strong currents flow axially at the top and the bottom and circumferentially along the sides of the pipe. When the magnetizer is horizontal, strong currents flow axially at the sides of the pipe and circumferentially at the top and the bottom. Modeling shows that a two-pole magnetizer produces strong current densities which are detectable at distances over two pipe diameters away from the magnetizer in a 12 inch pipe.[1] The distribution of the current density in the pipe at a pipe diameter away from the magnetizer has a simple sinusoidal form with respect to the circumference; closer to the magnets, the current density has a pulse shape with harmonics.

To explain the magnetic fields in the pipe they can be separated into static and dynamic parts. The dynamic part is due to the current flowing in the pipe caused by the rotating magnets. The static part is attributed to the direct magnetic field from the strong permanent magnets. Figure 11 illustrates the differences in signals when the sensor is near and far away from a pair of rotating magnets in a pipe with a diameter of 12 inches (305 mm). Additional results over a wider range of sensor to magnet separation distances are shown in Appendix A.

When the sensor is near (less than 12 icnhes away) the rotating magnets, the magnetic fields from the magnets and the currents flowing in the pipe produce a saddle-shaped alternating signal. When the sensor is positioned farther away (greater than 12 inches) from the magnets, the dynamic magnetic field caused by the currents flowing in the pipe dominates producing a signal that is nearly sinusoidal. Spectral analysis reveals higher-order odd harmonics are more than an

[1] The finite element results presented in this paper were obtained using a three-dimensional rotational analysis problem solver that could calculate the current generated by a permanent magnet passing a conductor (Opera-3d® from Vector Fields, Ltd., Aurora, Illinois).

order of magnitude smaller than the fundamental frequency. To a lesser extent, the amplitude of the static field from the magnets also depends on rotational frequency and magnet to pipe separation.

Figure 12 shows a prototype inspection system for a pipeline with a diameter of 12 inches (305 mm) and a wall thickness of 0.375 inch (9 mm). Two pairs of neodymium iron boron (NdFeB) magnets are mounted on a steel core machined from 1018 steel. The magnets are 2 inches(51 mm) long, 1 inch (25.4 mm) wide, and 0.5 inch (12.7 mm) thick; the magnet strength is 38 MegaGauss-Oersted (305 kJ/m^3). Although the magnets have a strong attraction to the steel core, aluminum guide rails prevent the magnets from moving and keep them precisely on the core. The air gap between the magnet and the pipe wall is 0.5 inch (12.7 mm). Wheeled support plates keep the magnetizing assembly centered in the pipe while a variable speed direct current motor is used to rotate the magnetizing assembly.

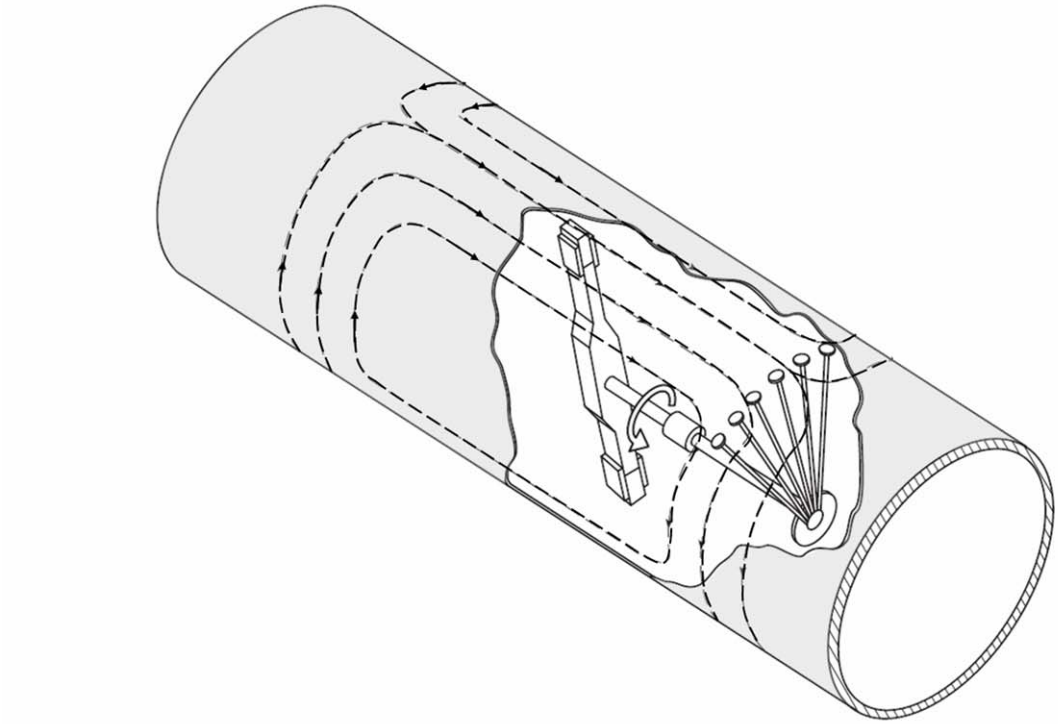

Figure 10. Illustration of the rotating permanent magnet exciter and sensor location

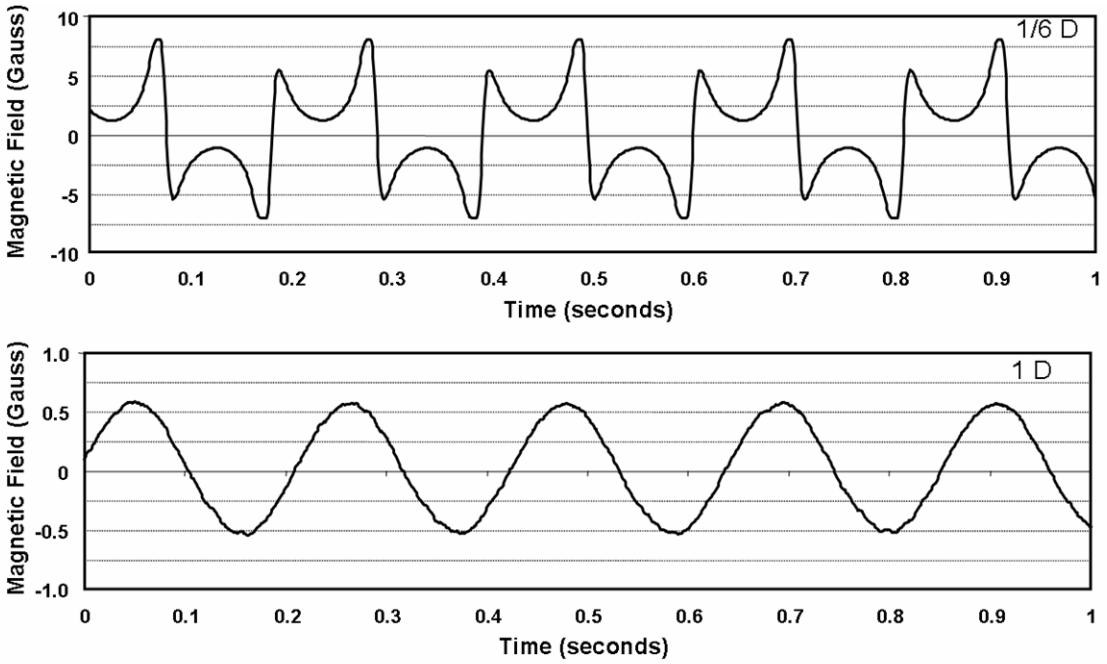

Figure 11. Magnetic field at the ID surface of the pipe near the exciter (top) and one pipe diameter away (bottom)

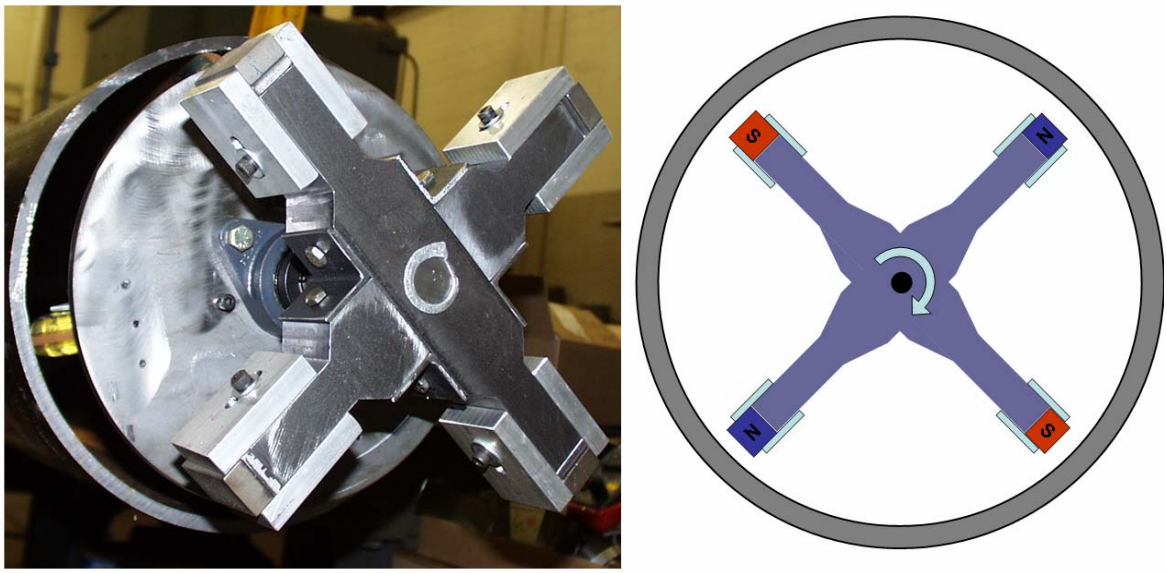

Figure 12. A rotating permanent magnet exciter for 12-inch (305 mm) diameter pipe with 4 magnets

Finite element modeling shows that a two-pole magnetizer produces strong and uniform current densities at distances well away from the magnetizer. Figure 13 shows modeling results for the 12-inch prototype system rotating at 300 rpm (5 Hz). The calculations were performed using

Vector Fields® three-dimensional rotational analysis solver. The image on the left shows the logarithm of the magnitude of the currents at the inside pipe wall. The current is strongest at the magnetizer poles, but becomes uniform at a distance of about half a pipe diameter away. The image on the right shows the current flow in the pipe, the direction as indicated by the arrows. While the current flow is complex near the rotating magnet poles, the current at a pipe diameter or more away from the magnetizer is uniform and sinusoidal.

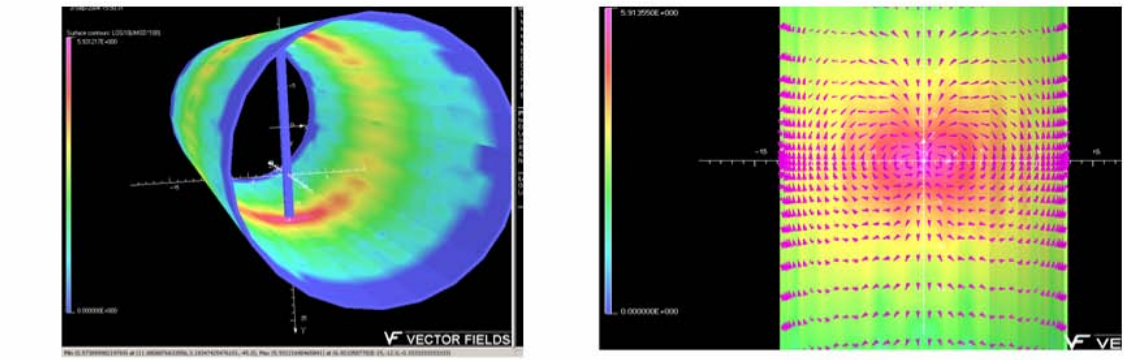

Figure 13. Finite-element modeling results for a two-pole magnetizer

3.2 Analytical Model

The previous section showed the optimal location to place the sensor is where the field from the magnets is small as compared to the dynamic field produced by currents flowing in the pipe. To generalize the experimental results, a mathematical representation of the strength of the current in the pipe induced by the rotating magnet system was derived through Ampere's Law and the Law of Charge Conservation. Some approximations and simplifications were used to obtain a simple closed form solution. As presented later in this paper, there was excellent agreement between this representation and the experimental results. Starting with basic physical laws, Ampere's Law can be written as:

$$\nabla \times \vec{B} = 4\pi\mu\vec{J} \tag{1}$$

where B is the magnetic field, μ is the magnetic permeability, and J is the induced current density. This equation relates the behavior of the magnetic field and the induced current density. The Law of Charge Conservation can be written as

$$\nabla \bullet \vec{J} = 0 \ , \tag{2}$$

since there is no build-up of charge within the cylindrical conductor. This equation states that current flows in loops, not segments. The induced current density can be written as follows:

$$\vec{J} = \sigma\vec{E} = \sigma\vec{v} \times \vec{B} \ , \tag{3}$$

with the first part representing Ohm's Law and the second part representing the Lorentz Force and where v is the velocity of the pipe with respect to the rotating magnetizer and σ is the conductivity of the pipe. This equation describes the velocity induced eddy currents. Note that this equation suggests that the induced current density is always perpendicular to the velocity. However, because the current density has no divergence (Equation 2), this will not always be the case. For the rotating magnetizer system, the velocity of the pipe wall with respect to the magnetizer is

$$\vec{v} = -\vec{\omega} \times \vec{r} \ , \tag{4}$$

where ω is the rotational speed and r is the radius of the pipe wall. Near the pole piece of the magnetizer (the source), the majority of the field is radial and the velocity is circumferential; consequently, the eddy currents would be axial, so that

$$J_Z = \sigma v B_R \ . \tag{5}$$

Equation 2 can be expanded to first order if we approximate the induced current density as a two-dimensional planar flow independent of pipe wall thickness. In this approximation, Equation 2 can be rewritten in cylindrical coordinates as

$$\frac{\partial J_Z}{\partial z} = -\frac{\partial J_\phi}{r \partial \phi} \tag{6}$$

where the subscripts z and ϕ refer to the axial and circumferential coordinates, respectively. To solve this problem for the behavior of the magnetic fields, a relationship between J_z and J_ϕ must be known.

Taking advantage of symmetry, the problem can be circumferentially sectioned into $2n$ parts, where n is the number of magnet pairs in the magnetizer. A symmetry section is centered at one magnet and ranges circumferentially between the angles of $\pm\pi/2n$ radians. For the magnetizer shown in Figure 10, the value of n is one and the symmetry section is $\pm\pi/2$ radians or $\pm 90^o$; for Figure 12, the value of n is two. Only one symmetry section needs to be solved, as the others are mirror images of this result.

To obtain the relationship between the two eddy current components, their circumferential distribution within a symmetry section must be estimated. Since Equation 2 forces the current to flow in loops, the following can be predicted. Based on the physics of the problem and assuming a two-dimensional planar flow, the value of J_ϕ at the center of the pole piece ($\phi = \phi_C$) must be identically zero while the value of J_z are peaked. Accordingly, the value of J_ϕ at the other boundary ($\phi = \pm\pi/2n$) are maximum while J_z are minimum. The farther the flow is axially from the magnetizer source, the more accurate this approximation will be (i.e., the far-field effect).

Based on the symmetry of this system, the circumferential distribution for J_ϕ would need to be an odd function of the coordinate ϕ that satisfies the above boundary conditions. To first order, we can approximate this odd function as

$$F(\phi) \approx F_0 \sin(n\phi) \ . \tag{7}$$

The actual function need not be a sine wave, but its function and derivatives should behave similarly. Using separation of variables, the function for J_ϕ can be written as

$$J_\phi(\phi, z) = J_0 J(z) \sin(n\phi) \ , \tag{8}$$

where $J(z)$ is only a function of the axial coordinate, z. Now, the circumferential distribution for J_z must be an even function in ϕ. This is satisfied by substituting Equation 8 into Equation 2, where upon integrating J_ϕ with respect to ϕ an even function is naturally obtained for J_z. Equation 2 can now be solved to determine $J(z)$ and so both $J_\phi(\phi,z)$ and $J_z(\phi,z)$. Substitution of Equation 8 into Equation 2 yields

$$\frac{\partial J_Z}{\partial z} = -\frac{\partial J_\phi}{r\partial \phi} = -\frac{n}{r} J_0 J(z)\cos(n\phi) \ . \tag{9}$$

Integration with respect to *z* yields

$$J(z) = e^{-(\frac{n}{r})Z} \ . \tag{10}$$

Therefore,

$$J_\phi(\phi, z) = J_0 \sin(n\phi) e^{-(\frac{n}{r})Z} \tag{11}$$

and the exponential behavior of the current density as a function of axial distance is revealed. The value of J_o is given by Equation 3 and is

$$J_0 = \sigma\omega r\beta M_0 \tag{12}$$

where M_o is the pole piece's magnetizing strength and β is a coupling factor that describes how much radial flux is coupled into the pipe wall and has a value between 0 and 1. While these values are assumed to be constant in this approximation, β is a nonlinear function of pole geometry and frequency that does not appear to be critical variable in the experimental studies performed to date.

Now, the circumferential component of Equation 1 yields:

$$\frac{\partial B_R}{\partial z} = 4\pi\mu J_\phi = -4\pi\mu J_0 F(\phi) e^{-(\frac{n}{r})Z} \ . \tag{13}$$

Solving for $B_R(z)$ and substituting Equation 12 into Equation 13 yields the following relationship for the radial field

$$B_R = 2\pi \frac{\beta}{n} (\frac{d}{\delta})^2 M_0 F(\phi) e^{-(\frac{n}{r})Z} \tag{14}$$

where δ is the classical skin depth and d is the pipe diameter, $d = 2r$. Again, the exponential characteristic of the magnetic field is revealed. Because

$$\nabla \bullet \vec{B} = 0 \ , \tag{15}$$

all three components of the magnetic field will have identical exponential decay along the pipe axis, at least in this approximation.

The same holds true for the radial to axial peak magnetic field amplitudes. In fact, the peak amplitude of the magnetic field as a function of axial position is given by

$$B_{pk}(z) \propto \frac{\beta}{n} (\frac{r}{\delta})^2 M_0 e^{-(\frac{n}{r})Z} \ . \tag{16}$$

Note that the peak amplitude of the magnetic field is proportional to the magnetizing strength of the pole piece (and the coupling factor) and the square of the ratio of the pipe diameter to classical skin depth, and inversely proportional to the number of pole pieces. Also, the

exponential decay constant, given by the ratio n/r, will cause greater decay for smaller pipe diameters and a higher number of pole pieces. This first order approximation suggests that the decay rate is basically geometry dependent.

Based on the finite element models, one can conclude that (1) the field amplitudes were mostly linear with rotational frequency; (2) the fields decrease exponentially independent of frequency, magnetizing strength, and pipe material property; (3) a larger number of magnets increases the decay rate and decreases magnetic field levels far from the source; and (4) with a smaller diameter pipe (e.g., 305 mm [12 inches] vs. 610 mm [24 inches] in diameter) the decay rate increases and the magnetic field levels decrease far from the source.

It should be noted that in the above approximation and in the finite element model, the magnetic permeability was assumed to be linear and isotropic. It actually is neither, and as a result some variations about this behavior can be expected. Also, the approximation is not valid near the magnetizer's pole pieces, i.e., close to the source, where the near-field effects predominate and result in a different near-field behavior. Figure 14 shows a comparison of the computed axial decay of the axial component with the closed form solution (Equation 16) and experimental results. The computed results were obtained using magnetic finite element analysis (FEA). For the experimental results, the rotating magnet assembly was positioned at one axial location while the sensor was moved along the inside surface of the pipe. At discrete locations along the pipe, the amplitude was measured with a Hall Effect sensor. The measured density was greater in the near field than the far field due to the nature of the amplitude changes. As illustrated in Figure 14, calculations and experiments show that the magnetic field decay is exponential. The rate of decay in pipe with a diameter of 305 mm (12 inches) is nominally an order of magnitude per pipe diameter. Experimental results, superimposed on the calculated results, confirm the analytical equation and the finite element calculations.

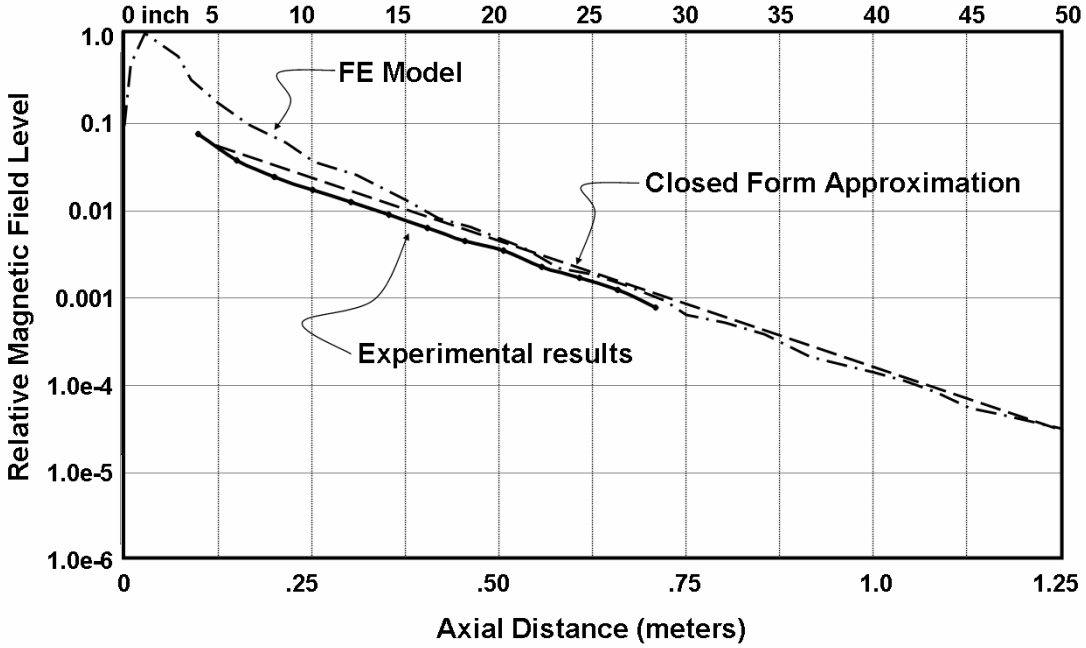

Figure 14. A comparison of the first-order estimate, modeling, and experimental results

3.3 Confirmation of Theory by Experiments

To demonstrate the validity of the closed form equation (Equation 16) for designing rotating exciters and positioning sensors, multiple configurations were implemented and tested. Figure 15 shows a plot of the change in magnetic field over axial distance for the three configurations tested:

- pipe diameter of 6 inches (152 mm) and two-pole magnetizer;
- pipe diameter of 12 inches (305 mm) and two-pole magnetizer; and
- pipe diameter of 12 inches (305 mm) and four-pole magnetizer.

The wall thickness of both the 6 and 12 inch pipe samples was nominally 0.375 inch (9 mm), and it was assumed that the magnetic permeability and electrical conductivity of both samples were equal. The signal frequency was 5 Hz. The rotation speed for the four-pole unit was cut in half to keep the frequency of the inspection current equal to that of the other two configurations. The plots in Figure 15 show that the decay rate is similar for the configuration with the 152 mm (6-inch) diameter pipe and two-pole magnetizer and the configuration with the 305 mm (12-inch) diameter pipe and four-pole magnetizer; only the initial amplitude of the smaller diameter magnetizer is lower. The decay rate of the configuration with the 12-inch (305 mm) diameter pipe and two-pole magnetizer is nominally half that of the other two. For the configuration with the 12-inch (305 mm) diameter pipe and four-pole magnetizer, two magnet bars were added to the two-pole magnet assembly and the polarity of the magnets assigned appropriately. Table 2 shows a comparison between the decay constant as calculated from Equation 16 and as measured from the exponential decay curves in Figure 15. The results compare quite favorably, considering the simplifications used in the equation. For the three test cases, the calculated values were slightly but consistently lower than the measured values.

Table 2. A comparison between calculated and experimental measured decays

	Pipe Diameter		Configuration		Decay (n/r)	
Configuration	mm	inches	Magnets	n	Calculation	Experiment
1	305	12	2	1	6.6	7.1
2	305	12	4	2	13.1	13.7
3	152	6	2	1	13.1	13.9

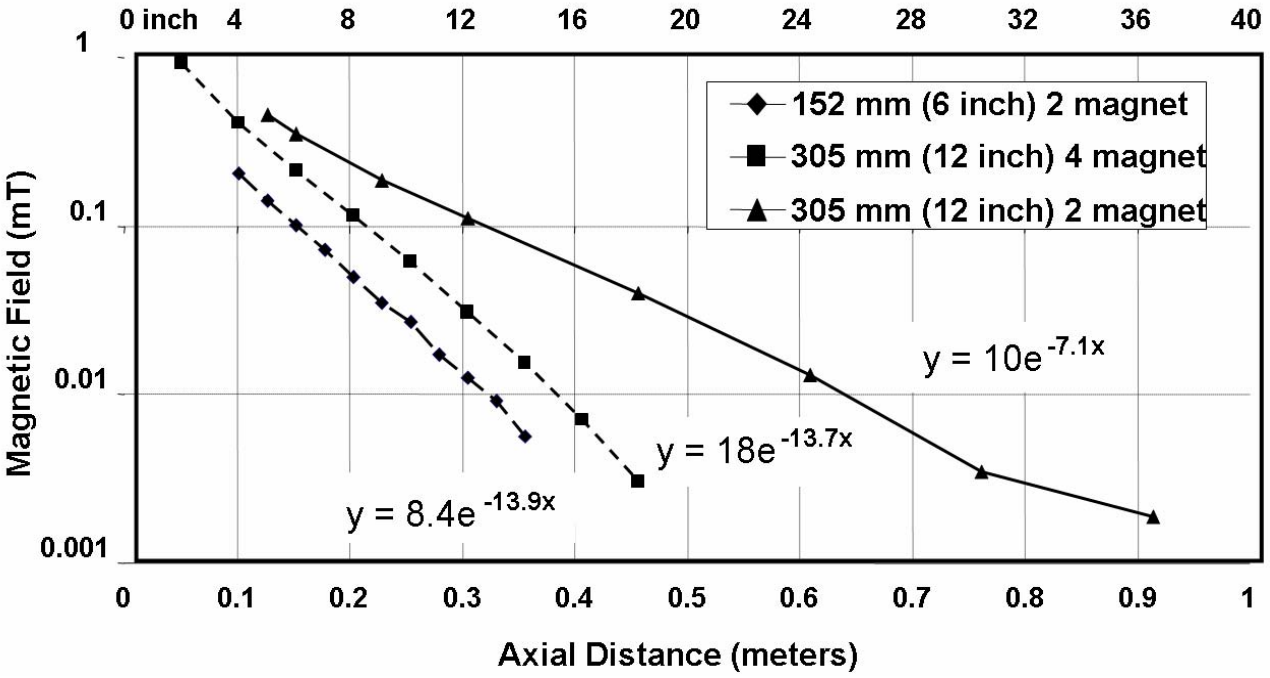

Figure 15. Experimental results showing the decay rate is related to both pipe diameter and number of poles

4 Components used to Attain Experimental Results

In the development of the rotating permanent magnet inspection method, electronic and mechanical components were configured to attain experimental results. As the experimental results defined areas of improvement, the developmental systems were modified. The general configuration of components is provided in the following sections including details of sensor, data recording, and rotating magnet systems.

4.1 Sensors

Hall Effect sensors were used to measure the magnetic field caused by the current flowing in the pipe. Hall Effect sensors are

- Well suited for the field levels which were on the order of a gauss,
- Frequency independent, in contrast to coils whose output is directly proportional the rotation frequency,
- Relatively low in cost (about a dollar for each sensor), and
- Rugged (used in automotive applications).

The commercially available sensors used were Honeywell Microswitch 495. The field levels were amplified by a factor of 100 using an operation amplifier after the Q-point offset was removed using a resistance voltage divider. Two of the three components of the magnetic field were measured, the axial and radial components. Typically three pairs of sensors were mounted in a sensor head as shown in Figure 16. The sensors are held nominally 0.040 inches (1mm)

from the pipe surface by the wear plate. Also shown in Figure 16 is the spring loaded linkage system used to keep the shoe in contact with the pipe.

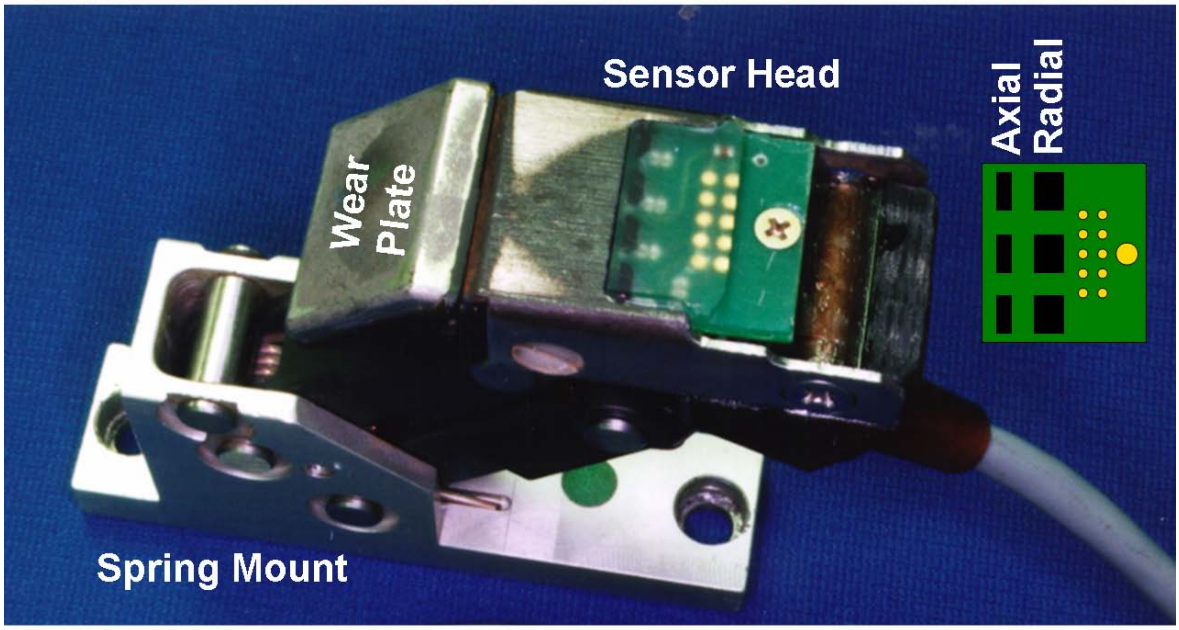

Figure 16. Spring loaded sensor shoe

A typical signal output from a metal loss anomaly for an axial-radial sensor pair is shown in Figure 17. The figure shows the pipe wall in profile in a segment that contains a machined metal loss defect. With the sensor pair aligned with the metal loss anomaly, the upper graph shows the unprocessed sinusoidal signals, and the lower graph shows a tracing through the peak values. The axial component of the magnetic field increases at the metal loss area. The radial component increases before the metal loss area and then decreases after. While typical variations in conductivity and permeability of the pipe can affect signal amplitude, by detecting both the axial and radial signal patterns, the probability of detection can be improved and false call rates can be reduced.

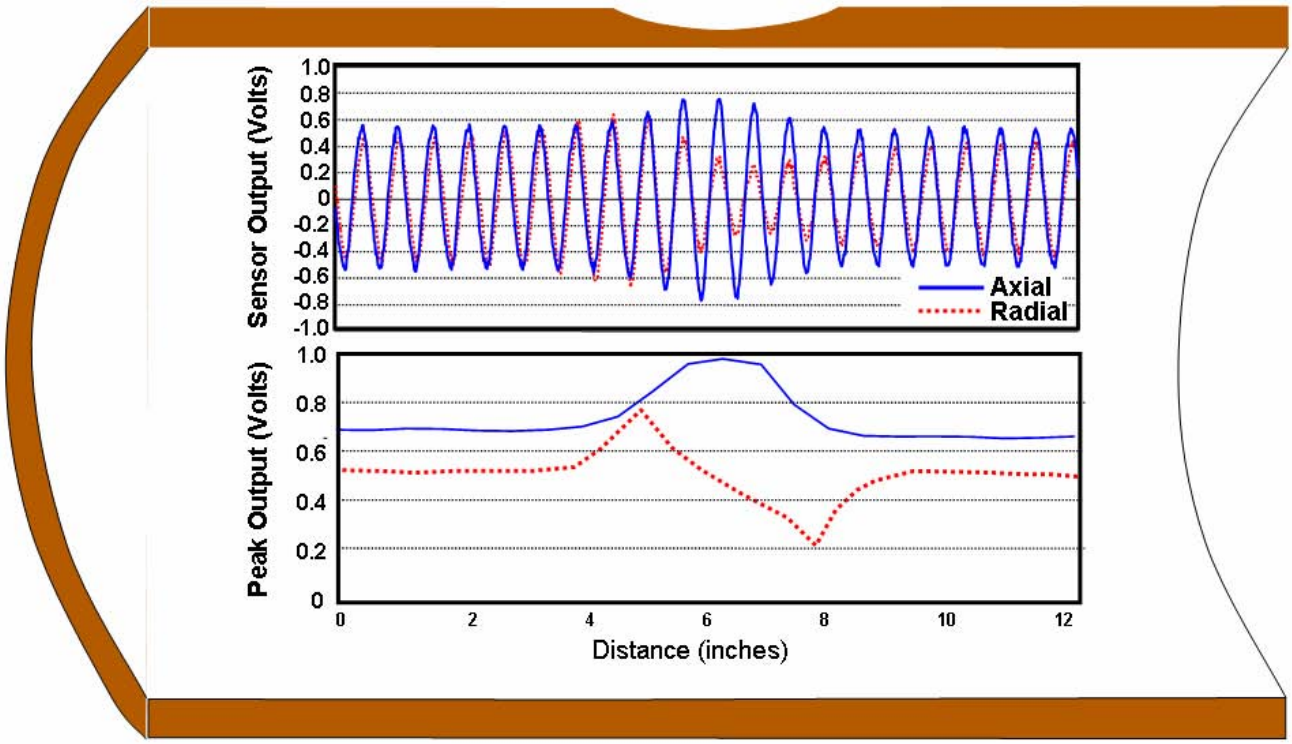

Figure 17. Typical signal from an area of pipe with a metal loss corrosion pit

4.2 Data Recording

Multiple sensors distributed around the circumference of the pipe are needed to measure signals from anomalies in an efficient manner. A multi-channel, real-time data recorder system was implemented to collect the sensor data. The goal of the recorder is to demonstrate that multiple channel sensor data could be simultaneously recorded and processed in a practical and efficient manner. A system was designed to simultaneously record and process 12 sensor pairs, or 24 Hall Effect sensors. The block diagram of the system is shown in Figure 18. The heart of the recorder is the National Instruments PXI-4472, an eight-channel dynamic signal acquisition module for making high-accuracy frequency-domain measurements. The eight NI PXI-4472 input channels simultaneously digitize input signals over a bandwidth from 0.5 Hz to 45 kHz. Three PXI-4472 modules are synchronized to provide 24 channel input using the PXI chassis and a star trigger bus. The PXI chassis communicates with a desktop computer using a fiber optic link. The desktop computer is used to analyze the signals using a lock-in amplifier approach, as described Appendix B. One of the 24 channels was used to record the reference signal required by the digital lock in amplifier. This signal was generated by a magnet on the shaft and a Hall effect sensor.

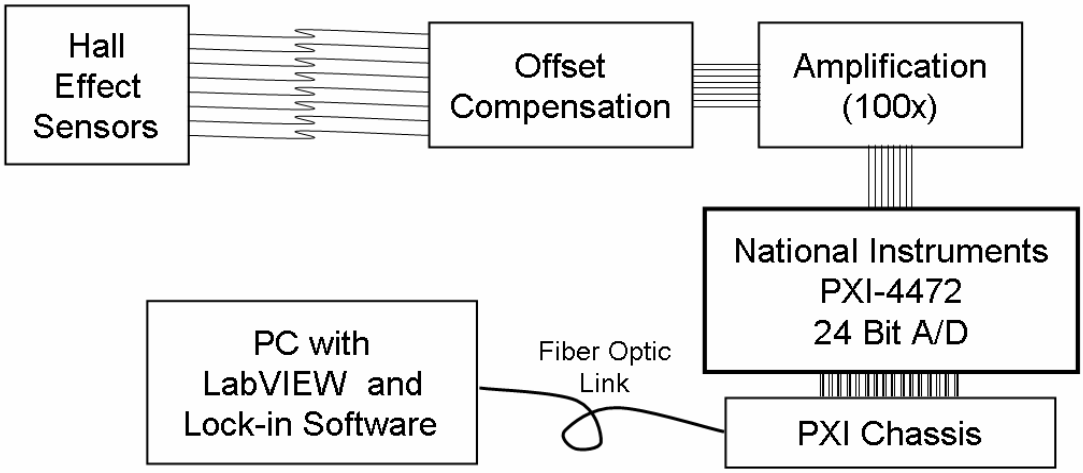

Figure 18. The block diagram of the data acquisition system

4.3 Rotating Magnet Systems

During the course of this program, various rotating magnet systems were built and modified to study the basic methodology, component configurations, anomaly response, and implementation variables. A generalized illustration is shown in Figure 19. Systems were built to inspect two pipe diameters, 12-inch and 8-inch, common diameters that were used in inspection benchmarking studies [13,14]. All laboratory prototype systems used a common motor. A central shaft was used to both spin the magnet bar and connect the motor, magnet and sensor carriages[2].

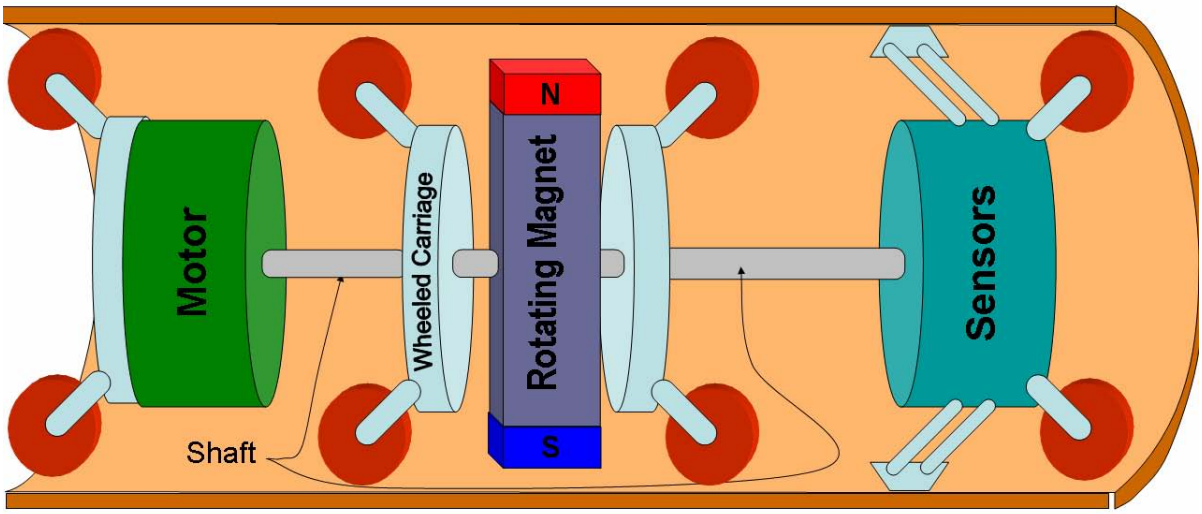

Figure 19. General configuration of prototype rotating permanent magnet inspection systems

[2] This turned out to be a poor design choice and an alternative was used in the final design presented later.

4.3.1 Laboratory Prototype for 12 inch pipe

The laboratory prototype was built for the first benchmarking in September 2004, shown in Figure 20. This 12-inch diameter system had NdFeB magnets that were 2 inches long, 1 inch wide, and 0.5 inch thick. The core material is common 1018 steel. The magnets hold themselves to the magnet bar with a force of attraction often 50 pounds or greater. Even with the large attractive force, the magnets can still slide on the magnet bar causing a misalignment which would establish an alternate path for the flux. Initially, aluminum guide rails were used to position the magnets precisely on the core; however the face of the magnet was left exposed and corners of magnets were occasionally chipped while inserting the tool into the test pipes. To maintain magnet alignment and protect the magnet, caps made of a non-ferromagnetic material, such as brass sheet metal, were placed over the magnets and attached to the magnet bar. The thickness of these caps is not critical for system performance; brass sheet metal with a thickness of 0.040 inches was used for the two prototypes.

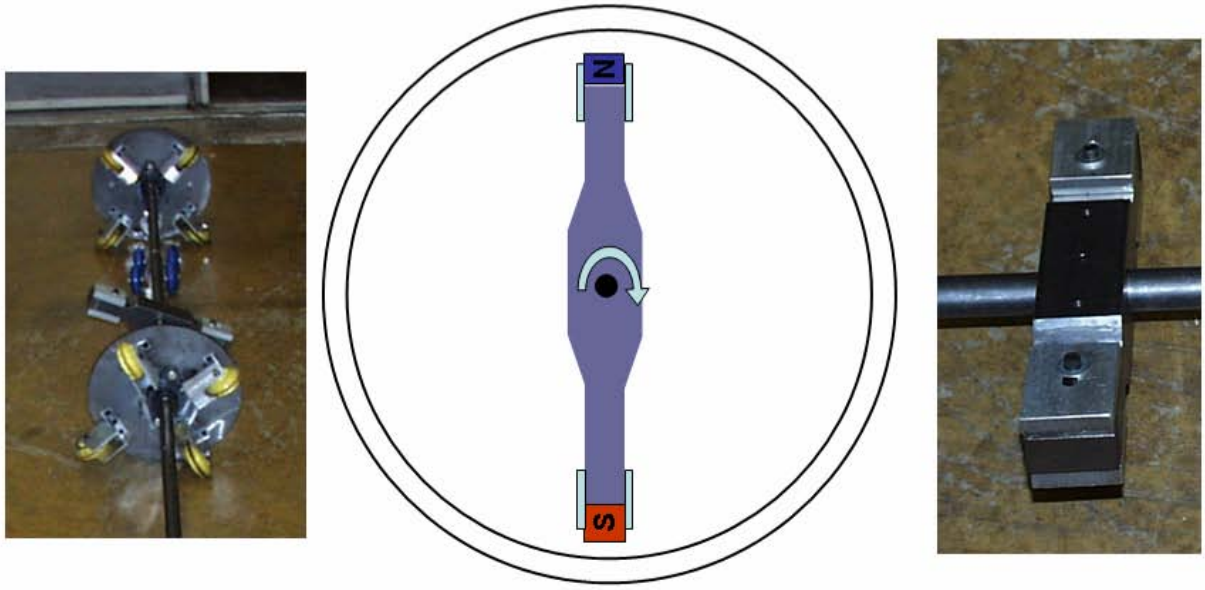

Figure 20. Two pole rotating permanent magnet exciter for 12 inch diameter pipe.

After the benchmarking, a special pole piece, shown in Figure 21, was developed to study the effect of separation distance between the magnets and the pipe on the signals produced for various pipe anomalies. The gap between the pipe and magnets could be adjusted between 0.45 and 1.35 inches.

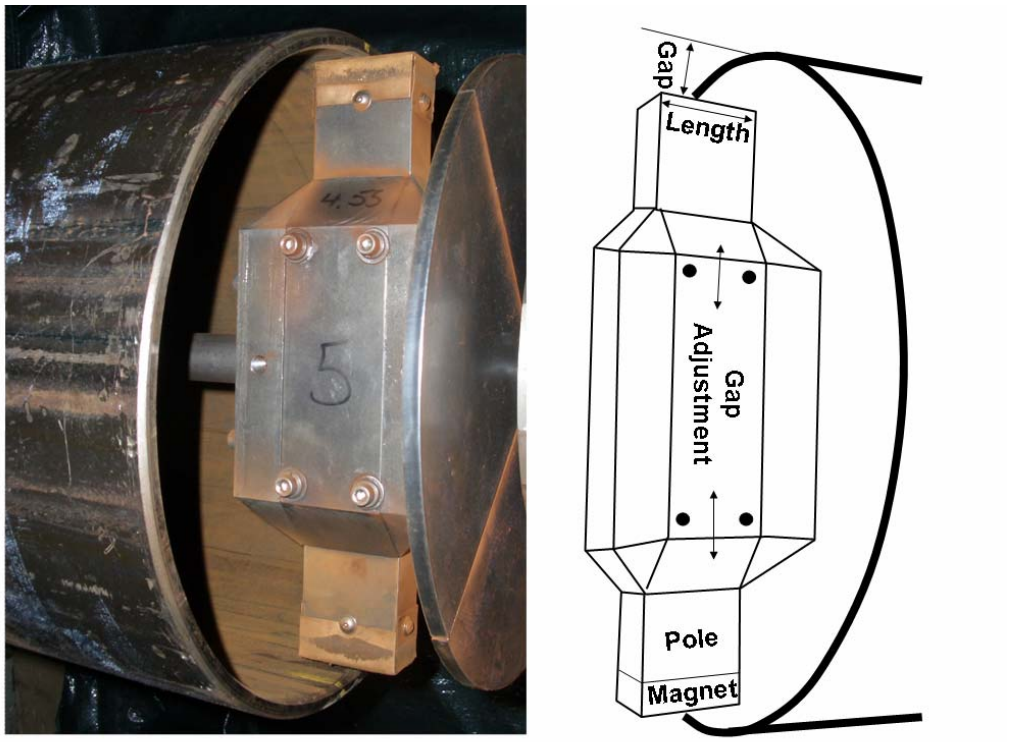

Figure 21. A special pole piece developed to study the effect of separation distance between the magnets and the pipe

4.3.2 Laboratory Prototype for 8 inch pipe

Figure 22 shows the laboratory prototype built for the January 2006 benchmark. This system, designed for 8 inch diameter pipe, included a pair of NdFeB magnets mounted on a steel core machined from 1018 steel. As on the 12 inch prototype, the magnets are 2 inches long, 1 inch wide, and 0.5 inch thick; the magnet strength is 38 MegaGauss-Oersted. After the benchmarking, this rotating magnet system was used to conduct further studies on the effect of different magnet configurations on the signal strength that included 1 inch x ½ inch x ½ inch, 1 inch x 1 inch x ½ inch, and 1 inch x 1 inch x 1½ inch magnets. Each size of magnet had a dedicated magnet bar to establish the gap between the pipe and magnet. Again, covers were used to keep the magnets precisely on the core, this time made of copper. The separation distances between the magnet and the pipe wall were 0.5 inches and 1.0 inches. Also shown in Figure 22 is the sensor configuration with twelve pairs of axial and a radial Hall Effect sensors mounted in the 4 sensor shoes designed to ride on the ID of the pipe.

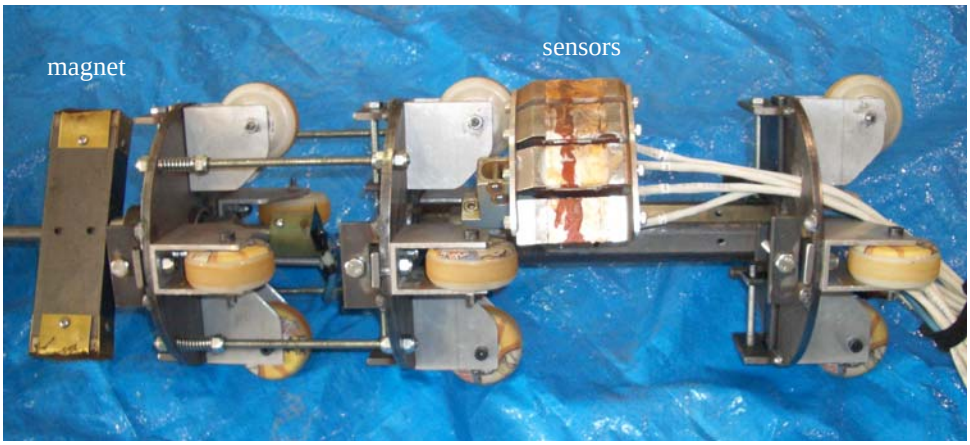

Figure 22. Rotating Permanent Magnet Inspection system as configured for the technology demonstration

4.4 Display Methods for Detecting and Sizing Anomalies

LabVIEW software modules for lock-in amplifier measurements were used in the development of a custom data acquisition and display program. A typical output of the data recording package is shown in Figure 23. In real time display mode, the data scrolls along the monitor as the inspection tool traverses inside the pipe; the display shows approximately 2 minutes of data. The upper and lower graphs show the axial and radial sensors respectively using a staircase plotting routine. In this figure, the signal from an 80 percent deep, 3 inch wide, 1.2 inch long metal loss anomaly can be seen in the middle channels of each sensor type.

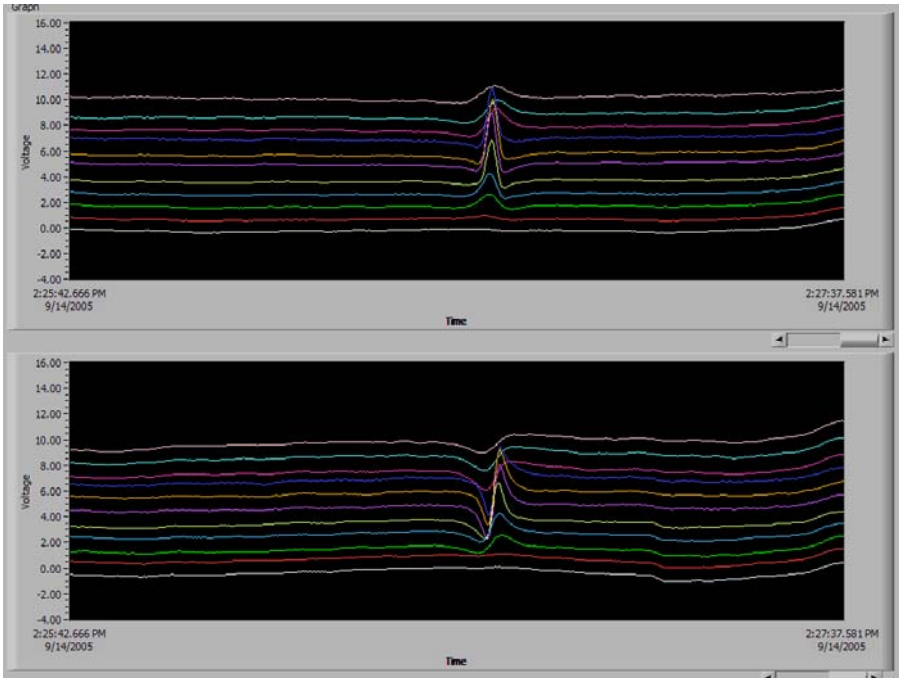

Figure 23. Display of custom LabVIEW data acquisition and display program. The axial signals are in the upper graphs and radial are in the lower

All data is stored for post processing that enables anomaly location and sizing. Figure 24 shows the entire length of one of the 12-inch diameter benchmark samples, nearly 300 inches (760 cm) or 25 feet (7.6 meters) long with the following features and anomalies highlighted in the figure:

- a 25percent circumferential groove (at 50 inches)
- two partial penetration welds (at 120 and 260 inches)
- MC1 – 80 percent deep, 3 inch wide, 1.2 inch long metal loss (at 80 inches)
- MC2 – 35 percent deep, 1.2 inch wide, 3 inch long metal loss near a weld (at 130 inches)
- MC5 – 60 percent deep, 2 inch wide, 1.2 inch long metal loss (at 50 inches)
- MC7 – two pits 48 percent deep, 1.1 inch wide, 1.1 inch long metal loss (at 240 inches)
- MC9 – an 80 percent deep, 1.5 inch wide, 2 inch long metal loss (at 280 inches) near end of the extent of travel of the inspection tool as configured for the benchmark.

Again, the upper graph displays the axial signal component and the lower graph shows the radial component for eleven sensor pairs.

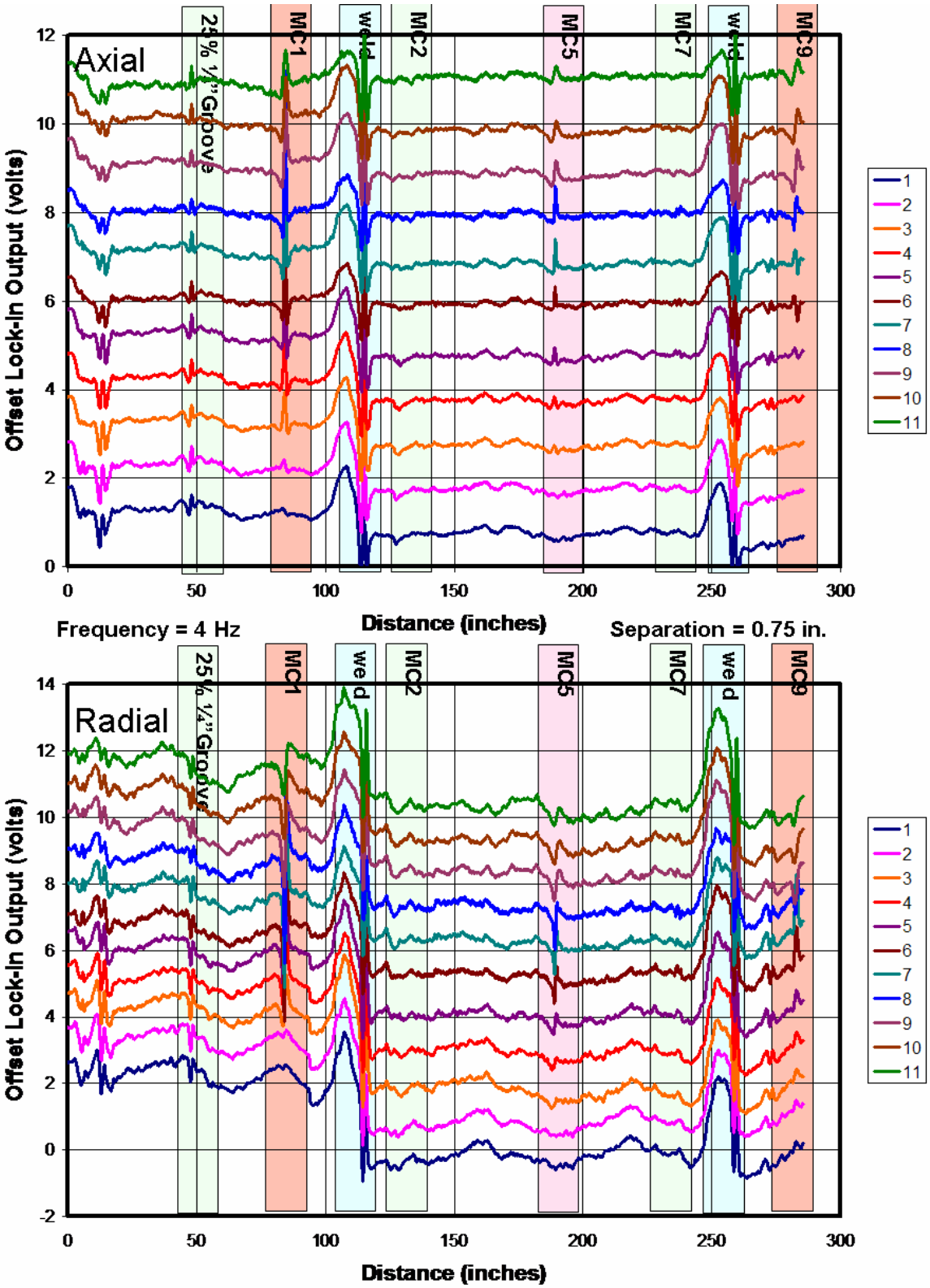

Figure 24. Axial and radial signals from benchmark pipe at a frequency of 4 hertz and a magnet to pipe separation is 0.75 inches

Isolated signals, shown in Figure 25, are examined to determine anomaly characteristics such as length and depth by extracting features such as amplitude and duration of the axial and radial signals. The anomaly in the Figure 25 is MC1, an 80 percent deep, 3 inch wide, 1.2 inch long metal loss anomaly in the 12 inch diameter 0.375 inch wall thickness pipe. No other anomalies are in the vicinity of this anomaly; therefore the signal variations seen in Figure 25 are due to pipe material variations and other sources of noise.

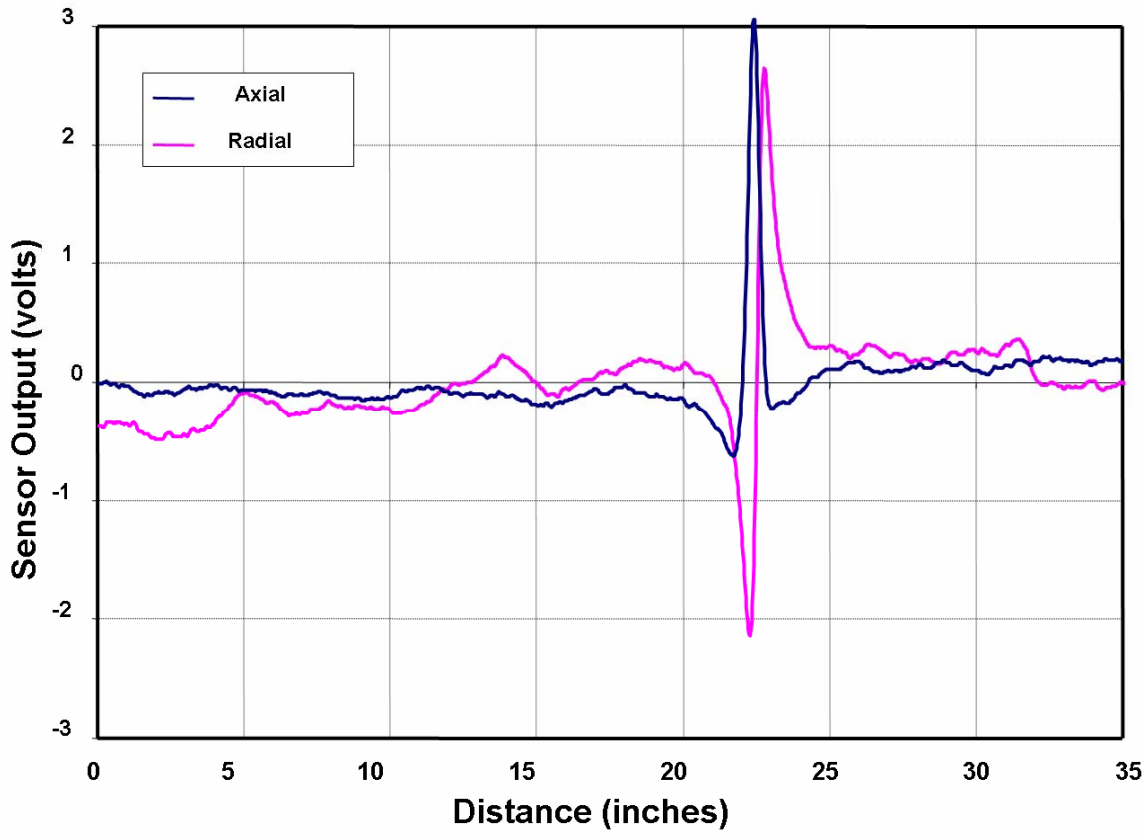

Figure 25. An axial and radial signal

Detection of anomalies is performed by detecting a generally increasing signal of the axial component at the same time as the bipolar radial signal. A method to reliably detect signals is to plot the axial and radial signal components against each other; a typical result shown in Figure 26. This display method is also an excellent way to compare signals; shown in Figure 26 are signals from 30percent and 50percent metal loss anomalies.

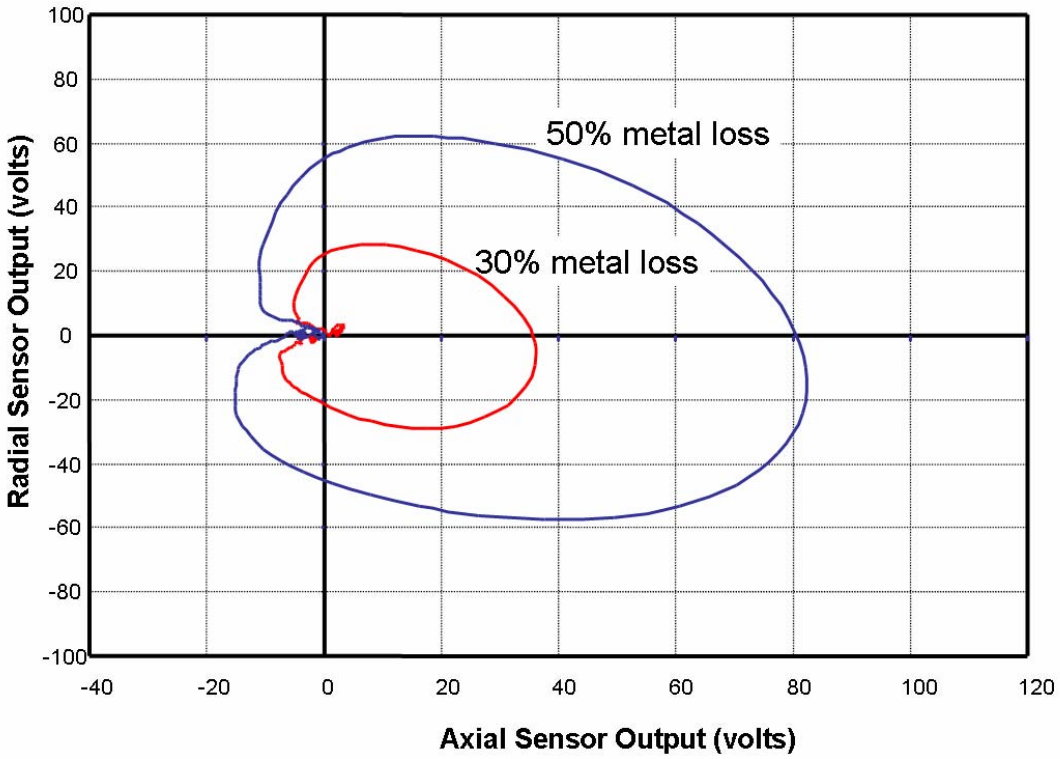

Figure 26. Axial – Radial signal plots for two metal loss grooves nominally 1.2 inches long and 3 inches wide, with depths of 30 and 50 percent as indicated

5 Experiments to Determine Basic Design Parameters

The two prototype rotating magnet systems described in the previous section were used to conduct experiments to understand some of the basic design parameters, including

1. Separation distance between the magnet and the inside of the pipe
2. Rotational frequency of the spinning magnet
3. Separation between the magnet and the sensor
4. Size of the magnet

The next three sections provide experimental results and conclusions on these inspection system variables.

5.1.1 Rotational Frequency

The rotational frequency influences the inspection speed, distribution of eddy currents through the thickness of the pipe and the power needed to spin the magnets[3]. Inspection speed is directly

[3] Motor power increases with faster rotation of the magnet. Other variables including magnet geometry, strength and separation distance between the pipe and the magnet effect motor power. Results on motor power are presented later.

proportional to rotational frequency; a 4 hertz rotation frequency enables an inspection rate of 240 feet per hour[4].

Fundamental studies on rotational frequency and magnet geometries were conducted for several anomalies and magnet configurations. Figure 27 shows an axial-radial plot for a 50 percent depth, 1.125-inch long, 3-inch wide flaw for rotational frequencies ranging from 3 to 12 hertz, repeated 3 times at each frequency. This result is for a 1 inch long by 1 inch wide by 1.5 inch thick brick of NeFeB with a power of 42 megaGaussOersted.. This figure shows that signal amplitude decreases with rotational speed. This implies that smaller anomalies will become more difficult to detect at higher rotational frequencies. Results for additional anomalies and magnet configurations are contained in Appendix C. The impact of the results on the design of a rotational magnet system is presented in section 7.

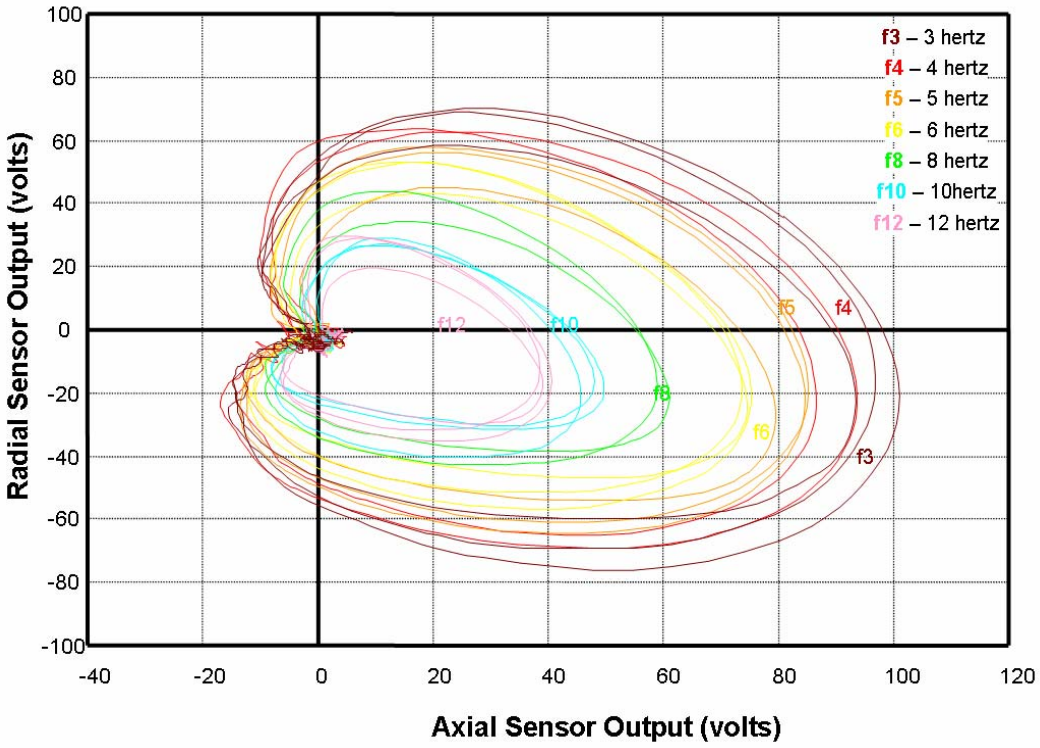

Figure 27. Axial – radial plot of signals from a 50% deep, 1.125-inch long, 3-inch wide metal loss defect at frequencies ranging from 3 to 12 hertz, repeated three times

5.1.2 Magnet to Pipe Separation

In the initial designs, the magnets were positioned as close as practical to the pipe wall to attain large signal levels at the sensors. An unexpected result was attained when varying the magnet to pipe separation distance. Scoping experiments showed that when the separation distance

[4] This calculation assumes an inspection data interval of 0.2 inches. Doubling the frequency doubles the distance. Halving the data interval halves the inspection rate.

between the magnet and the pipe wall was varied between 0.5 inches and 0.75 inches there was no significant change in signal amplitude; however background noise levels increased when the magnet was closer to the pipe. As such, a larger separation distance between the magnet and the pipe was found to be advantageous since it allows for a cleaner signal while at the same time makes the inspection apparatus smaller to more easily pass through diameter restrictions. Since these results were counterintuitive (a decrease in signal amplitude was expected for increasing separations), further experiments were performed to quantify this phenomenon.

To quantify the magnet to pipe separation, the distance from the pipe to the magnet was varied from as little as 0.45 inches to as much as 1.35 inches. The metal loss anomaly discussed previously (80 percent deep, 1.2 inches wide, 3 inches long), was examined at six magnet to pipe separations (0.45, 0.65, 0.75, 0.95. 1.05, 1.35 inches) at an inspection frequency of 4 hertz with the results shown in Figure 27. The anomaly signals appear very similar for all liftoffs. By increasing the magnet to pipe separation to even greater distances, it is expected that the signal amplitude will eventually decrease, however significant modification to the current magnetizer design would be required to conduct this experiment and therefore was not evaluated. Magnet to pipe separation of over an inch provides sufficient flexibility in the design of the inspection system and further quantification will be performed only if required by new design requirements.

Repeating the pipe to magnet separation experiments discussed in the previous section for a frequency of 8 hertz, Figure 28 again shows strong signals that are relatively independent of separation distances. Figure 29 quantifies the results of both the 4 hertz and 8 hertz experimental results by plotting the peak to peak signal amplitude for the separation distances examined.

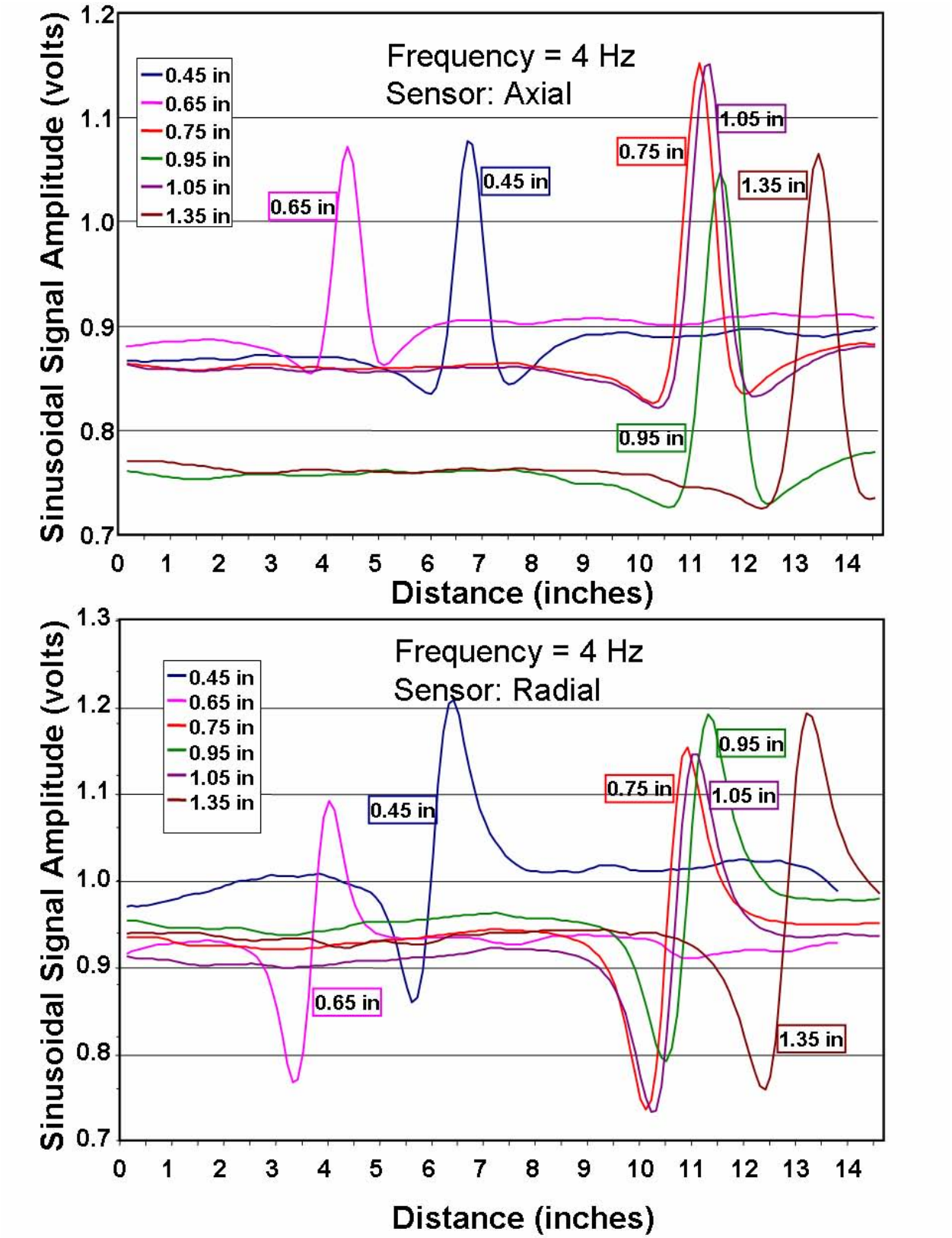

Figure 28. Axial and radial signals from benchmark anomaly MC1 at a frequency of 4 hertz and a magnet to pipe separation ranging from 0.45 inches to 1.35 inches

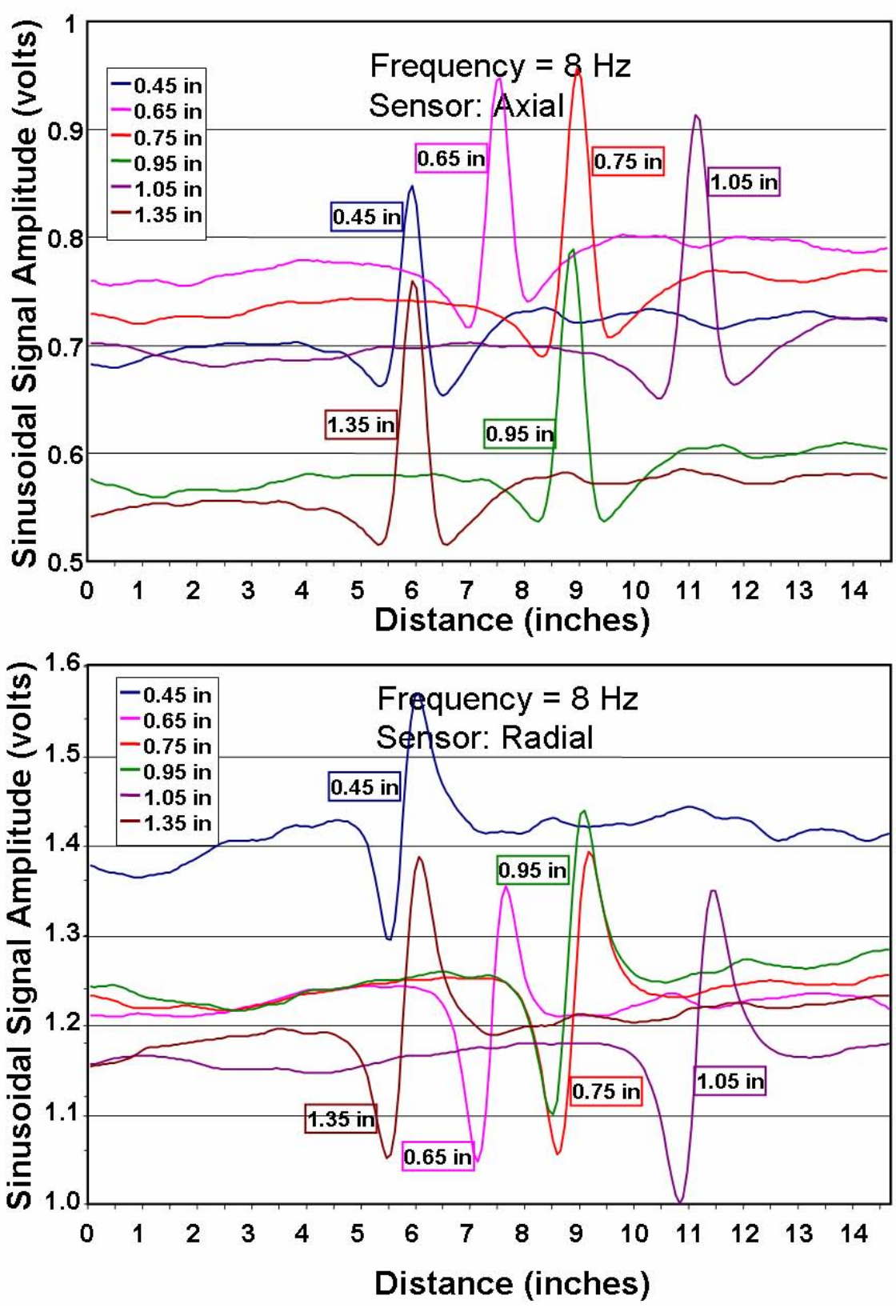

Figure 29. Axial and radial signals from benchmark anomaly MC1 a frequency of 8 hertz and a magnet to pipe separation ranging from 0.45 inches to 1.35 inches

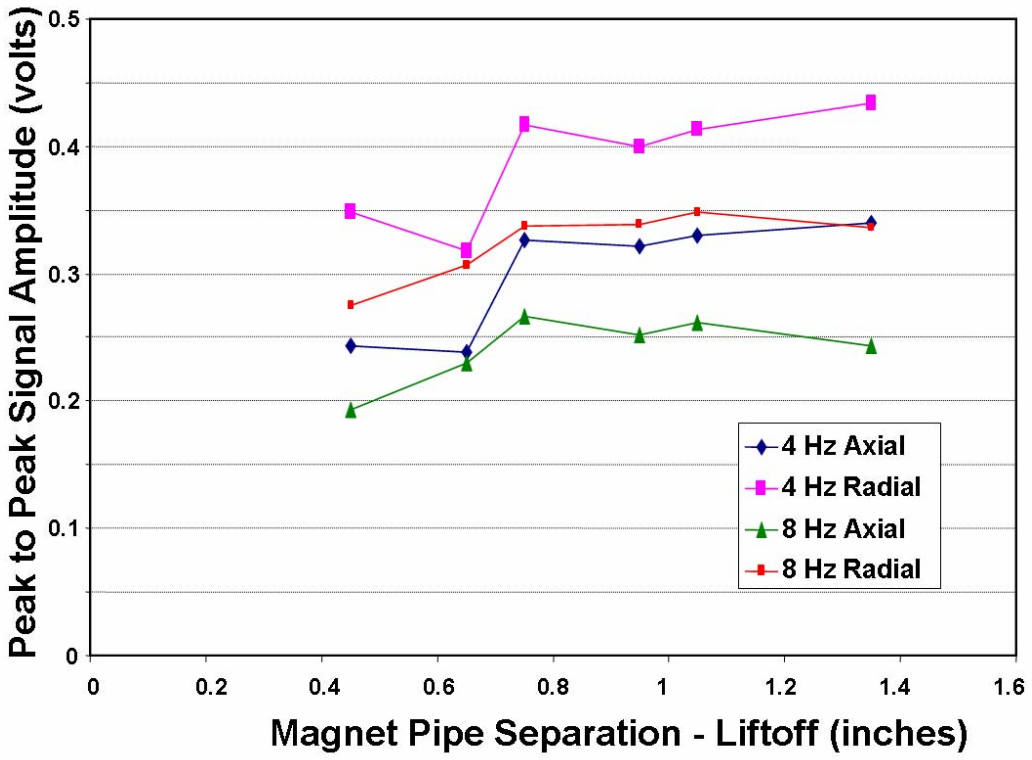

Figure 30. Peak to peak signal amplitude for the separation distances examined

5.1.3 Attenuating the Static Field

As discussed previously, the magnetic field in the pipe has two parts, each with distinct properties and effects. One part is the static magnetic field from the strong permanent magnets; this field is directly detected by the sensors without the generation of current. The second field is the dynamic magnetic field due to the induced current flowing in the pipe. Near the rotating magnets, the direct field from the magnet is dominant and produces a saddle-shaped alternating signal. Farther away from the magnets, the magnetic field caused by the currents flowing in the pipe dominates producing a sinusoidal signal pattern. For the 12 inch diameter pipe, experiments showed that positioning the sensor approximately 12 inches (300 mm) or more from the magnetizer could be used to attain a signal dominated by the induced current in the pipe, the dynamic field. This distance may not be practical for some configurations, particularly for smaller diameter pipe. To further reduce the direct field effect at distances closer to the magnet assembly, a magnetic shield between the magnet and the sensors was investigated. The concept is illustrated in Figure 31. The shield is made of a ferromagnetic material, such as steel, and is slotted to reduce the generation of circumferential eddy currents in the shield which would reduce the currents in the pipe. Unfortunately, this configuration did not prove useful as illustrated by the signals in Figure 32. The signals for the configuration with the shield are smaller in amplitude and more distorted.

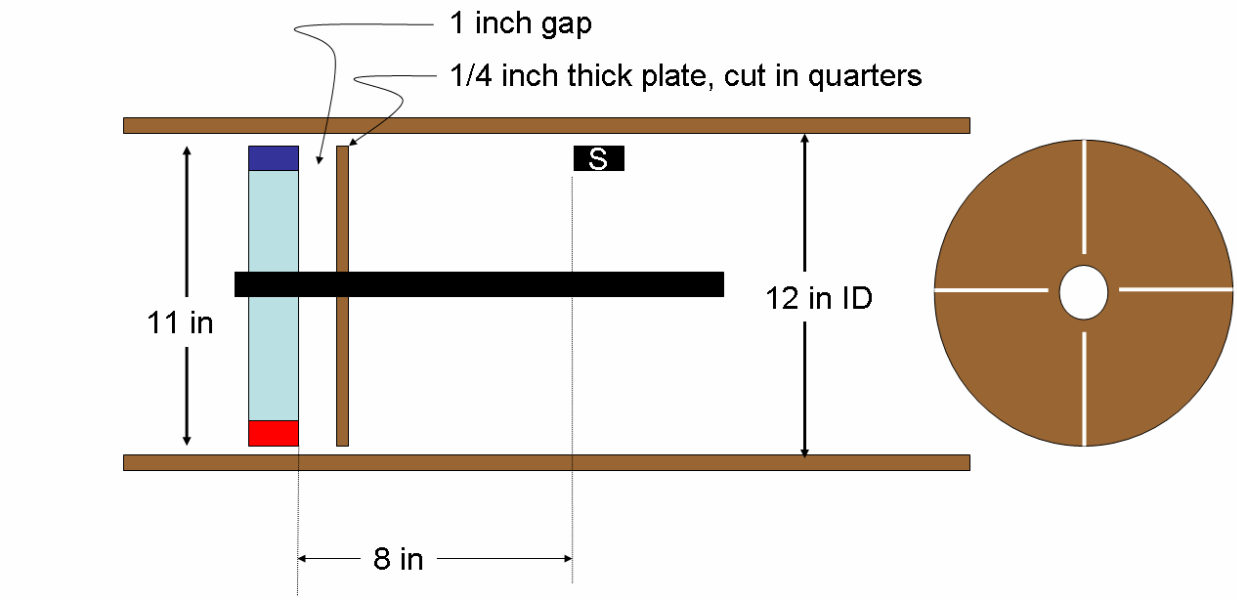

Figure 31. A magnetic shield between the magnet and the sensors to reduce the direct field

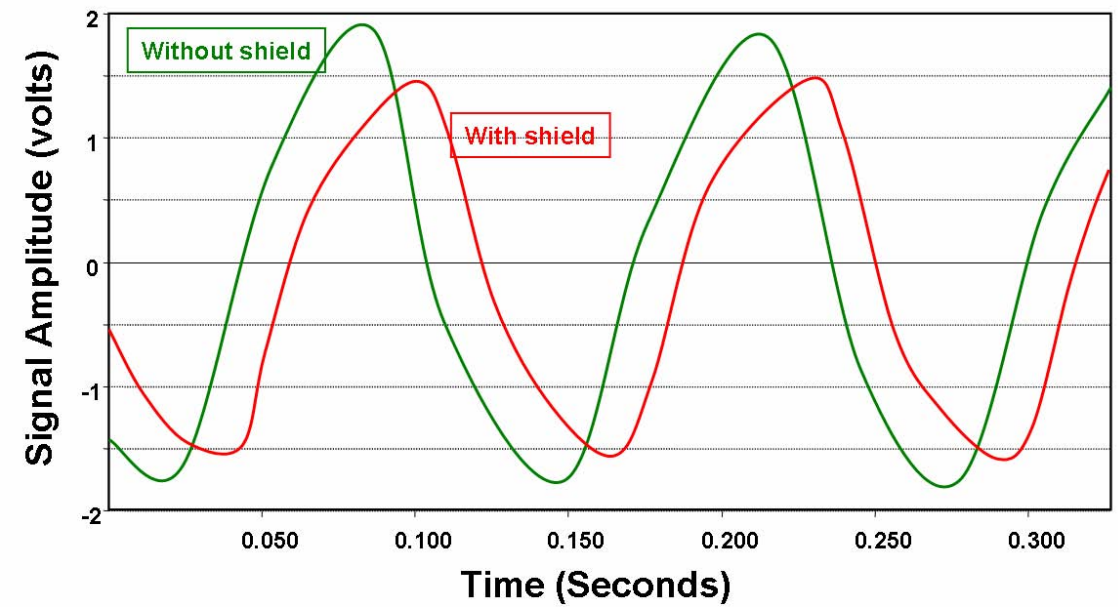

Figure 32. Signal with and without shield designed to reduce the direct magnetic field

6 Assessment of Metal Loss

The development of the rotating magnet inspection system has focused on the detection and sizing of metal loss anomalies. Two blind benchmarking studies were conducted during this program. The first benchmarking study, which occurred during the first year of development, showed feasibility of the inspection technique to detect metal loss. At that point in the development, sensor and data recording systems did not provide sufficient data to attempt sizing of anomalies.

In the second benchmarking study, full metal loss detection and sizing was attempted. The typical result is seen in Figure 33 with the results from all anomalies proved in Appendix D. A scaled topographical map of the corrosion depth is included at the bottom of Figure 33. The two humps in the stacked graphs correspond to the two pits in the image. Other graphical representations, including plotting axial versus radial signals (as shown previously in Figure 26), are proving to be useful in assessing and sizing corrosion. The signals provided in Appendix D are plotted on the same scale for quick visual comparison.

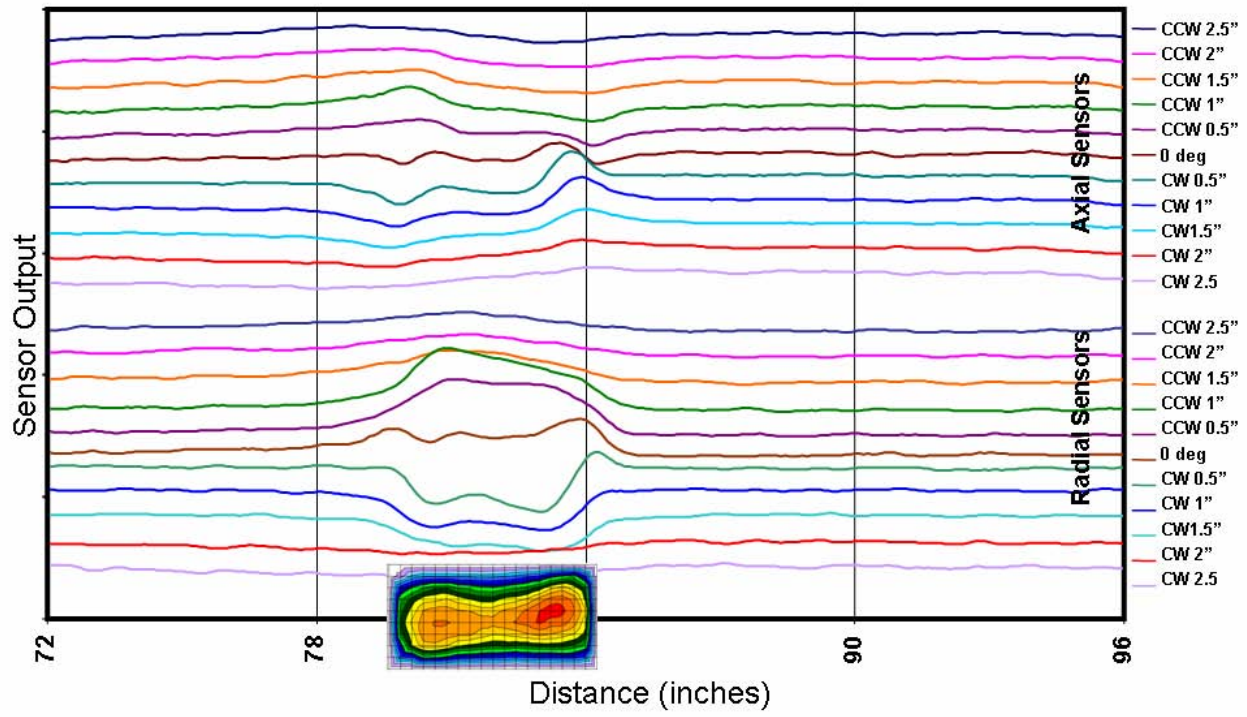

Figure 33. Typical signal from a variable depth anomaly

Detection. The results of the demonstration showed that all corrosion anomalies were detected and one additional anomaly was falsely detected. The false call anomaly was assessed as small and as not detected in all pulls. The spacing between sensors (sensor pitch) of the demonstration configuration was 0.5 inches. For corrosion with shallow depth and a width and length nominally the same as the sensor pitch, a detectable signal may only be produced by a sensor traveling directly underneath the anomaly. Two sensors straddling the same anomaly may not produce a signal. Future implementations may need a finer sensor pitch to improve results. For this inspection technology, the detection threshold is a function of both wall thickness and corrosion depth as well as the area of the metal loss. For anomalies with diameters greater than four wall thicknesses (4T), 30 percent anomalies were clearly detected in 0.188 pipe. For wall thickness greater than three tenths of an inch, the detection threshold increases with wall thickness. A full characterization of wall thickness and depth variables will require additional pipe materials and experimentation.

Corrosion sizing. A corrosion anomaly locally increases the density of the currents that are induced by the rotating magnetizer. The local change in current density is also influenced by the length and width of the anomaly. The algorithm for estimating the depth of the corrosion anomaly includes these three measures, in a manner similar to magnetic flux leakage data analysis methods. Data from the calibration anomalies and the first benchmark demonstration were used to establish the sizing algorithm. The unity plot shown Figure 34 indicates a good correlation between measured and predicted values; however there is a general tendency to undercall the depth. This was the first algorithm developed for corrosion anomaly depth assessment and may need to be refined in future implementations.

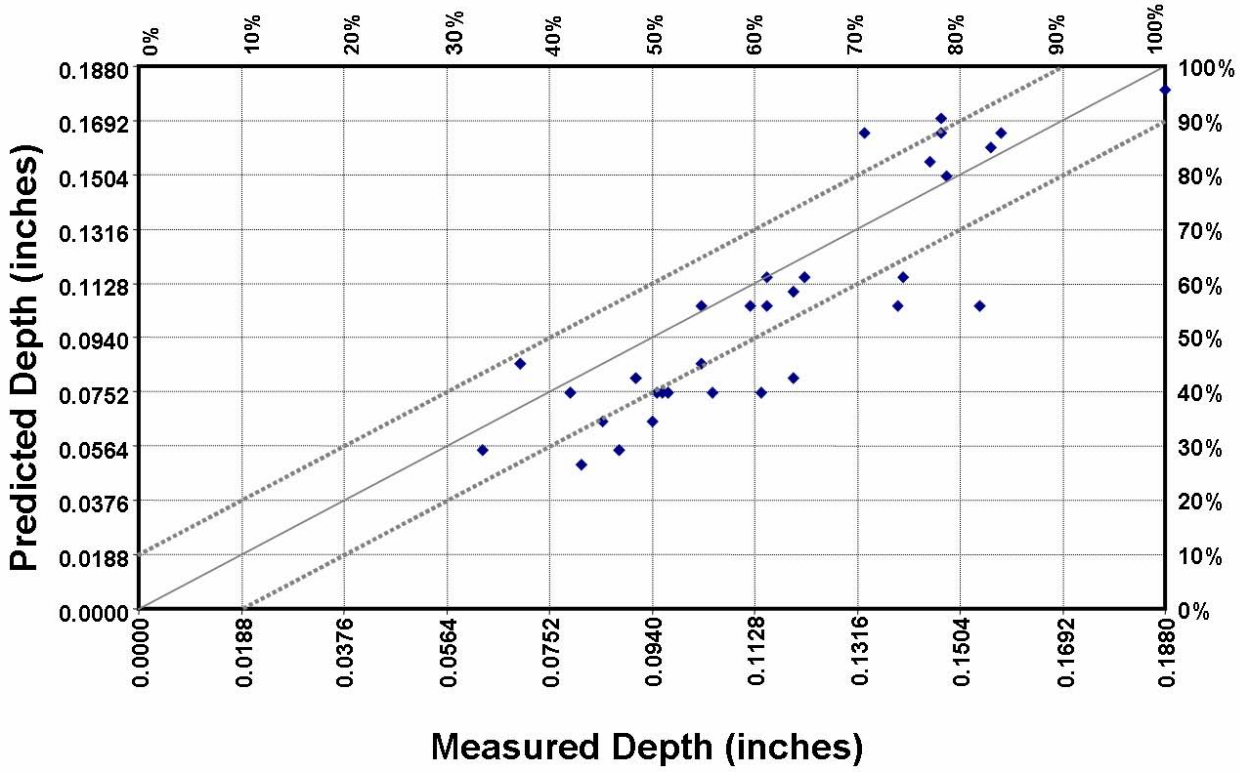

Figure 34. Unity plot for benchmark study

The benchmarking results are a representative assessment of the current state of development of the RMPI system. Improvements are possible to enhance detection and sizing capability.

7 Design Considerations of a Rotating Permanent Magnet Inspection Exciter

In its simplest form, the rotating permanent magnet inspection (RPMI) system is a bar magnet that spins on the shaft of a motor. Although the basic design principle is simple, there are a number of individual components that need to be optimized to obtain the best inspection capability while still maintaining design practicality. The design goals for the RPMI system are to:

- Maximize current away from the rotating magnets so that changes at anomalies produce larger signals.
- Minimize the motor power requirements to rotate the magnets, thus enabling longer inspection runs on a single battery charge.
- Minimize inspection system size so that it is capable of passing though openings much less than the nominal pipe diameter.

As with any engineering design, some of these goals cannot be met simultaneously. Specifically, first engineering principles would indicate that the largest, most powerful magnet will produce the strongest current in the pipe, which addresses the first design goal. However, large, strong magnets are in opposition to the second design goal, since power to spin the magnet is greater for large and powerful magnets. Furthermore, large strong magnets are in opposition to the third design goal since larger support components are needed for larger magnets.

The functionality of the entire system must be considered in a prudent design. For example, a significantly smaller inspection system may be possible while still maintaining reasonable inspection performance. The following sections discuss optimizing the size of the magnet bar, the design of the motor and rotating assembly, and the design of the collapsible components of the inspection system. The result is the conceptual design of a rotating permanent magnetic system for pipe ranging in size from 8 inches to 18 inches in diameter.

7.1 Number of poles

The first step in the design is to determine the number of magnets. As described in section 3, a first order approximation of the field behavior in the rotating permanent magnet inspection system was derived through Ampere's Law and the Law of Charge Conservation. The peak amplitude of the magnetic field as a function of axial position is given by

$$B_{pk}(z) \propto \frac{\beta}{n}\left(\frac{r}{\delta}\right)^2 M_0 e^{-\left(\frac{n}{r}\right)Z} \tag{17}$$

where:

- Z is the distance from the magnets along the pipe
- r is radius
- n is the number of pole pairs
- δ is the classical skin depth
- β is a coupling factor that includes separation between the magnet and pipe (between 0 and 1)
- M_0 is magnetic energy in magnet pole piece

This equation indicates that the peak amplitude of the magnetic field is proportional to the magnetizing strength of the pole piece (and the coupling factor) and the square of the ratio of the pipe diameter to classical skin depth, and inversely proportional to the number of pole pieces. Also, the exponential decay constant, given by the ratio of pole pairs to pipe radius (n/r), will cause greater decay for smaller pipe diameters and a higher number of pole pieces. This first order approximation suggests that the decay rate is basically geometry dependent. The validity

of this equation was demonstrated experimentally. The other term in the decay rate, distance from the magnets along the pipe, Z, is essentially a constant for all pipe diameters.

To detect anomalies, the signal from the dynamic field in the pipe must be greater than the magnetic field from the permanent magnets. Experiments on 6 inch, 8 inch, and 12 inch diameter pipe have shown that the direct coupling of the field from the magnets to the sensors is not significantly related to pipe diameter. At 8 inches of separation, the direct field distortion signal was nominally 20 percent of the initial current field. Table 3 shows the relative signal levels for a range of pipe diameters and pole configurations. Areas of marginal performance are highlighted in gray.

Table 3. Relative signal levels for a range of pipe diameters and pole configurations

Pipe Diameter		# of poles pairs	Signal level	
Inches	Meters		Sensor to Magnet Distance 8 in (20cm)	Sensor to Magnet Distance 12 in (30cm)
4	0.10	1	13.5%	5.0%
5	0.13	1	20%	9.1%
6	0.15	1	26%	13.5%
8	0.20	1	37%	22%
10	0.25	1	45%	30%
12	0.30	1	51%	37%
14	0.36	1	56%	42%
16	0.41	1	61%	47%
18	0.46	1	64%	51%
10	0.25	2	20%	9.1%
12	0.30	2	26%	13.5%
14	0.36	2	32%	18%
16	0.41	2	37%	22%
18	0.46	2	41%	26%
20	0.51	2	45%	30%
24	0.61	2	51%	37%

In general, a straight magnet bar with a magnet at either end (one pole pair) will work for diameters of 8 inches and greater. For diameters greater than 16 inches, a cross configuration with 4 magnets (2 pole pairs) should be considered. The cross configuration is advantageous because it would produce two cycles of alternating current per revolution. In other words, the rotation speed could be cut in half while maintaining the same inspection capability. This would reduce the motor power requirements and stress to the mechanical components. While there is no maximum theoretical diameter for a bar magnet with a pair of poles, there is a transition zone between 16 inches and 20 inches where the cross configuration becomes advantageous.

7.2 Magnetizer Design

An essential element in maximizing the current at the sensors and minimizing the system power requirements is in the design of the magnet bar. Referring to Figure 35, the key parameters of the magnet bar include the axial length, circumferential width and radial thickness of the magnets as well as the separation between the magnet and the pipe wall, further referred to as liftoff. As any electrical current generator that uses permanent magnets, the magnet composition and strength are also an important variable that affects the induced current densities and thus inspection capabilities. These design variables relate the design goals in the following way:

- Inspection current – Larger magnet area, thicker magnets, and smaller liftoff all increase current density for detection of anomalies
- Motor power – Two poles, smaller magnet area, thinner magnets, and greater liftoff all decrease motor power consumption
- System size - Two poles, smaller magnets and smaller pole pieces enable the passage of the tool though openings much less than the nominal pipe diameter.

A range of configurations were examined to establish the optimal system.

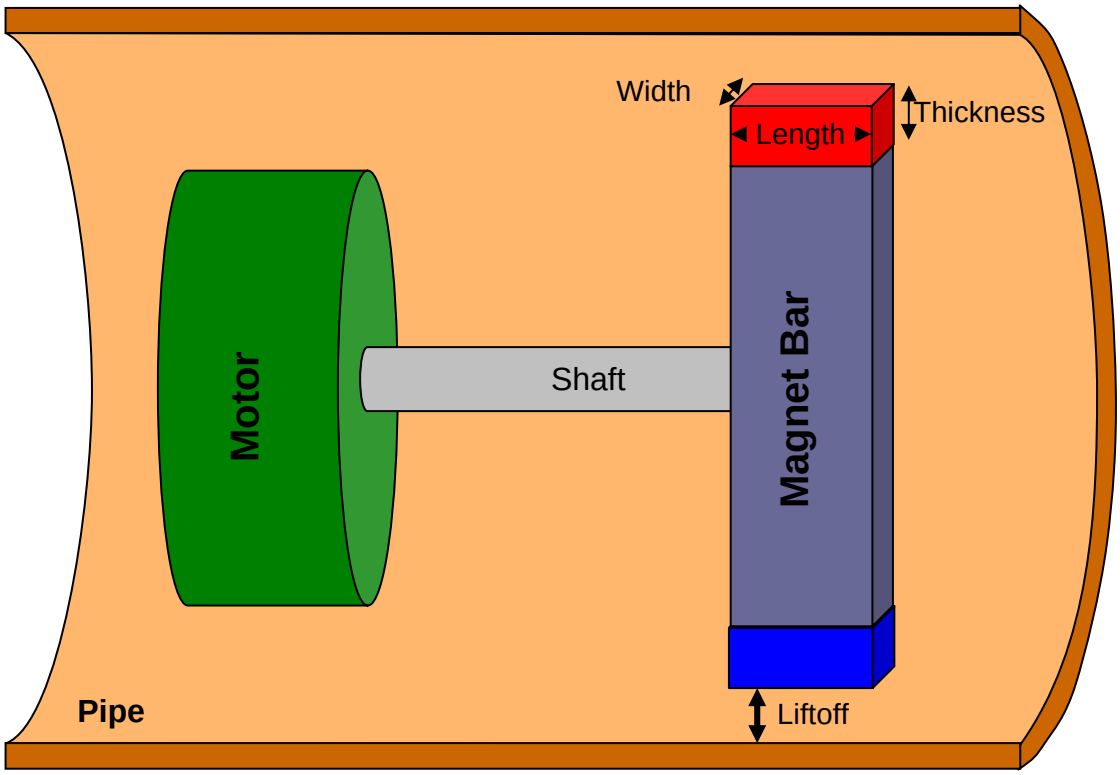

Figure 35. Fundamental components of the Rotating Permanent Magnet Inspection System

Initially, two prototypes were built to evaluate the inspection capability of this inspection method and optimize design parameters. The first had a nominal diameter of 12 inches and the second had a nominal diameter of 8 inches. Both were benchmarked in blind trails using pipe samples with machined metal loss anomalies and natural corrosion in 2004 [13] and 2006 [14]. Both

prototypes used 2 inch long, 1 inch wide, and ½ inch thick bricks of neodymium iron boron (NdFeB) with an energy product of 35 megagauss oersted (MGOe). When specifying magnets, the orientation of the magnetic field is through the thickness.

The length and width of the magnet bar should be the exact same dimensions as the magnets. The main goal is to channel as much magnetic flux into the pipe wall as possible; any size variation would establish alternate paths for the magnetic flux which would reduce current generation.

High strength magnets made from NdFeB are readily available in a number of standard shapes. In recent years, the magnetic energy of these specialized magnets has increased while at the same time the cost to purchase these magnets has decreased. These factors have enabled the practical experimentation of a range of magnet configurations to identify optimal inspection parameters. While the magnets themselves are less than $20 per brick, a unique magnet bar had to be machined for each configuration which became the dominate cost of the optimization tests of components.

To establish the optimum magnetizer geometry, a range of magnet lengths, widths, thicknesses and liftoffs were examined. The magnet configurations tested are given in Table 4.

Table 4. Optimization of magnet length, width, thickness, and liftoff variables

Length	Width	Thickness	Liftoff
(inches)			
2.0	1.0	0.5	0.5
1.0	1.0	1.5	0.5
1.0	1.0	1.5	1.0
1.0	1.0	0.5	0.5
1.0	1.0	0.5	1.0
1.0	0.5	0.5	0.5
1.0	0.5	0.5	1.0

To quantify the anomaly detection capability of each magnetizer configuration, three metal loss anomalies were examined

- N1: 1 inch long 3 inch wide 30 percent deep
- N2: 1 inch long 3 inch wide 70 percent deep
- N3: 1 inch long 3 inch wide 50 percent deep

Successive inspections of the pipe sample were conducted while varying the magnet rotational frequency between 3 and 20 hertz and measuring the electrical power supplied to the motor at each frequency. Figure 36 shows the signal amplitude for the first three metal loss anomalies (30 percent, 50 percent, and 70 percent of wall thickness) for the seven different magnet configurations at a rotational speed of 5 Hz. The motor power requirement for each

configuration is provided along with a depiction of the magnet shape and liftoff. The following observations can be drawn form the results:

- The 1-inch x 1-inch x 1.5-inch magnet (thickest) at 1-inch liftoff produced the largest signal.
- Magnets at a 1-inch lift-off produce better signals than magnets at a ½-inch liftoff. Similar results were attained in a 12-inch pipe sample previously inspected where the separation between the pipe and magnet was adjusted in 0.1 inch increments [13].
- Motor power required to maintain rotational speed was larger for magnets at ½-inch liftoff than magnets at 1-inch liftoff.
- At both the ½ inch and 1 inch liftoffs, the signal strength for the smallest magnets (1 x ½ x ½ inch) were significantly weaker than the 1 x 1 x ½ inch magnets, while the power requirements were only slightly less.

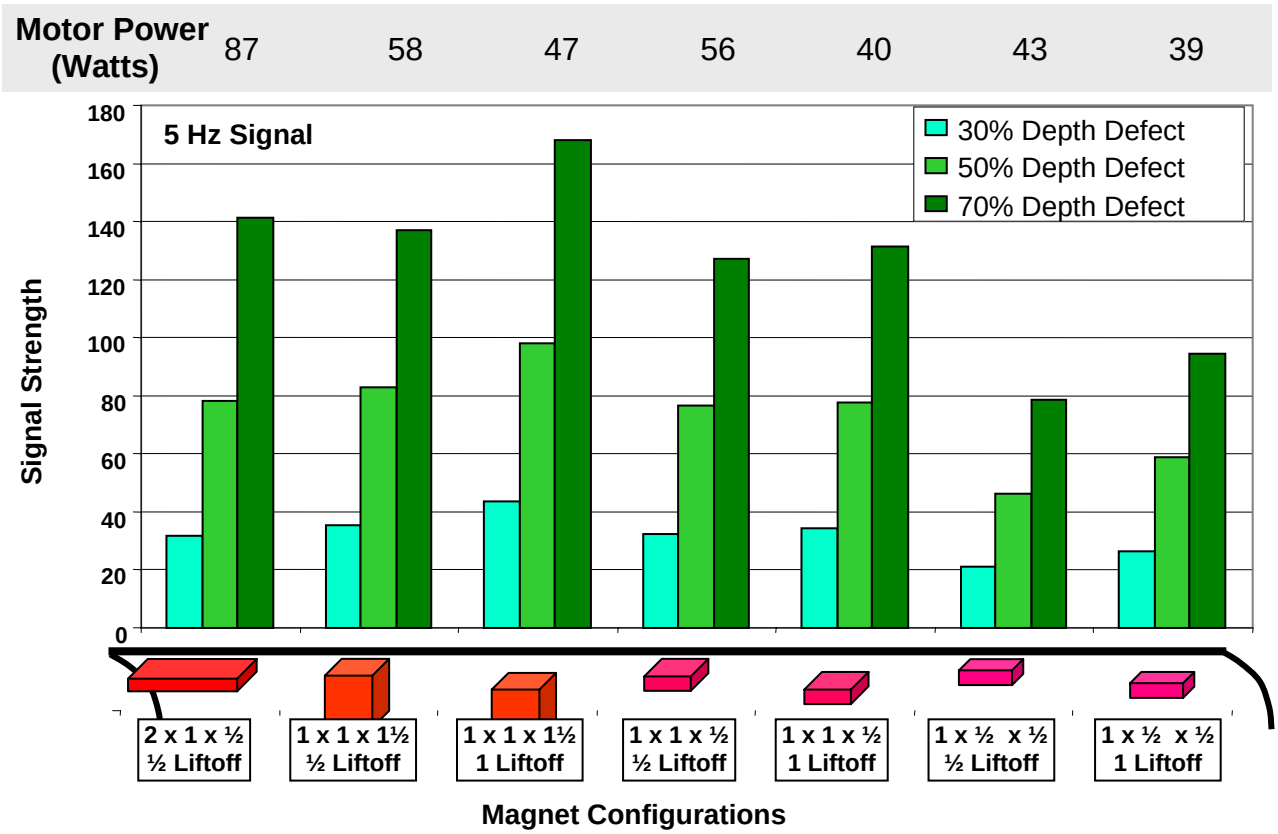

Figure 36. Signal level from corrosion anomalies for seven magnet configurations at 5 hertz rotation frequency

Similar results, presented in Figure 37, are achieved for a test frequency of 10 Hertz. Overall, the signal levels are smaller at the higher frequency; however the general trends are similar.

The experimental results in these examples are for eight inch diameter pipe; optimal values for each magnet configuration may vary for different pipe diameters. When designing a RPMI system, the following guidelines can be drawn from the experimental results:

- Positioning the magnets further away from the pipe wall is better for both signal strength and power considerations. More importantly, this allows for greater design flexibility for pipelines with restrictions.
- A larger magnet area (length x width) is not necessarily better. A 1-inch x 1-inch inch magnet area performed better than both the 2-inch x 1-inch and a 1-inch by ½-inch magnet configurations.
- Thicker magnets tend to give better signals, but other practical design requirements will limit thickness.

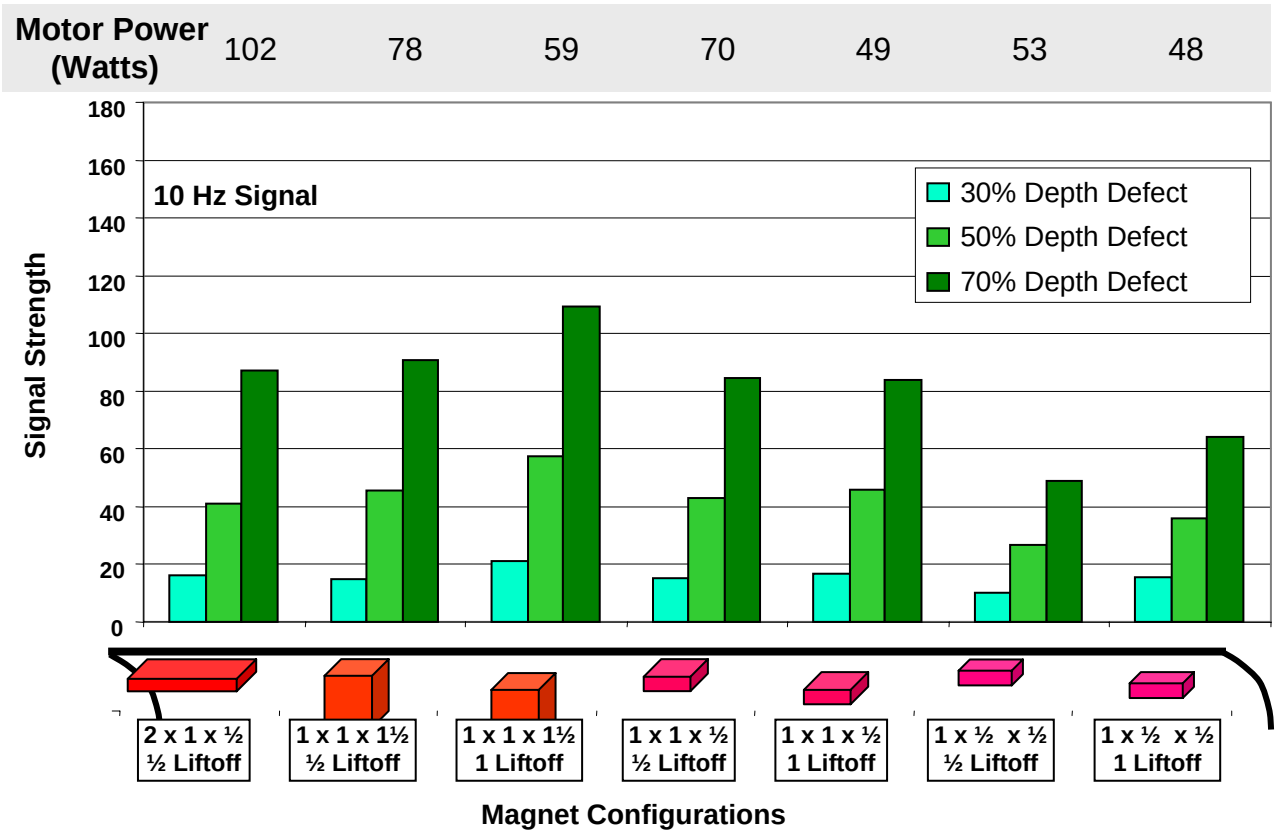

Figure 37. Signal level from corrosion anomalies for seven magnet configurations at 10 hertz rotation frequency

While first principles indicate that bigger magnets close to the surface would increase current generation, the first two guidelines establish limits on these values. With these guidelines for the magnet configuration, implementation details for the rotational assembly can be considered.

7.3 Motor and Rotating Assembly

A wheeled carriage system, illustrated in Figure 38, is used to center and support the motor and magnet in the pipe. In the first two prototype designs, the motor shaft used to rotate the magnets also transferred the forces from the drive and sensor modules. This dual load caused the bearings at the motor and the carriage closest to the magnet to misalign and prematurely fail.

The bearing problems can be reduced by having the magnets rotate around a fixed tube or shaft, as illustrated in Figure 39. A bearing pair is inserted into the magnet bar with the inner race connected to the fixed tube. At the end of the motor shaft is a gear that meshes with a second gear directly coupled to the magnet bar. The axial pulling loads applied from either end are transferred through the fixed shaft to the other side rather than to the bearings. An added benefit of this design is that the fixed tube can be hollow, enabling the passage of power cables, signals and data from one end of the system to the other. Figure 39 shows the motor in an offset position. A centered motor configuration could be easily implemented with the addition of a second gear pair which would facilitate the use of a larger motor or enable the passage of tighter bends with a smaller motor.

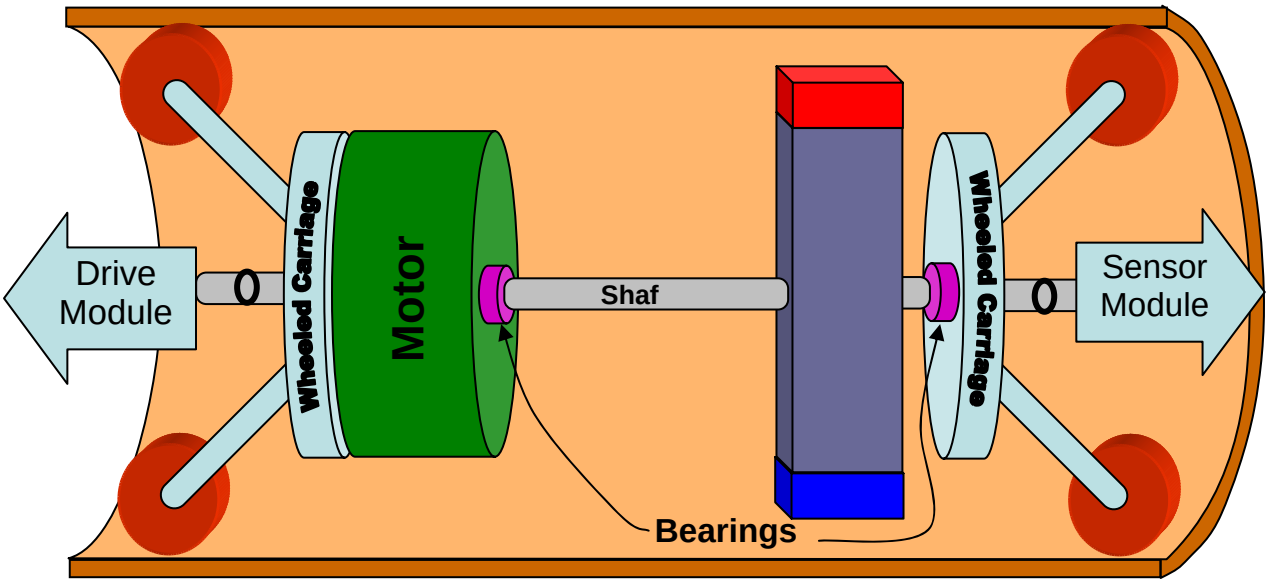

Figure 38. Illustration of carriage system used on prototype designs

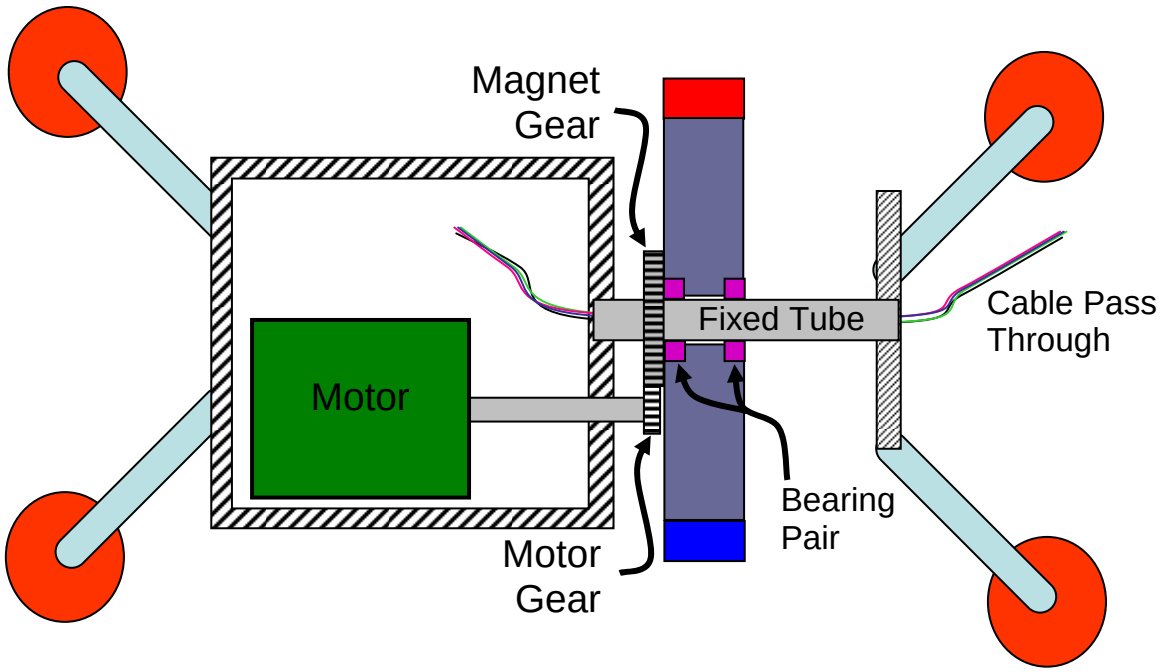

Figure 39. Fixed tube design for improved performance of the RPMI System

7.4 Retracting Magnet Bar

While one inch separation between the magnets and pipe is sufficient to pass significant obstructions, additional reduction may be desired. To further reduce the cross-section, the magnet bars can be designed to retract without degradation to the magnetic performance. Since it would not be practical to expect an inspection system to perform in severe restrictions like plug valves, the rotation of the magnets would be stopped. In addition, to pass oblong obstructions, the magnet bar could be aligned with the largest opening. The magnet system design has three basic guidelines:

- There must be a continuous path of magnetic material between the two magnets
- The path should not have any abrupt changes in cross-section
- The cross-sectional area of the magnetic material perpendicular to the magnetic flux path must be greater than or equal to the cross-sectional area of the magnets (length x width)

A novel feature of this implementation is the ability to configure the magnetizer to a form factor that allows the tool to pass obstructions within the pipeline. In the example configuration shown in Figure 40, a telescoping magnet bar retracts the magnets as they pass over obstructions, while in the example shown in Figure 41, a hinged structure allows the bars to bend to pass over obstructions. For either implementation, centripetal force or simple mechanical devices such as worm screws can be used to move the magnets back into the proper position for inspection.

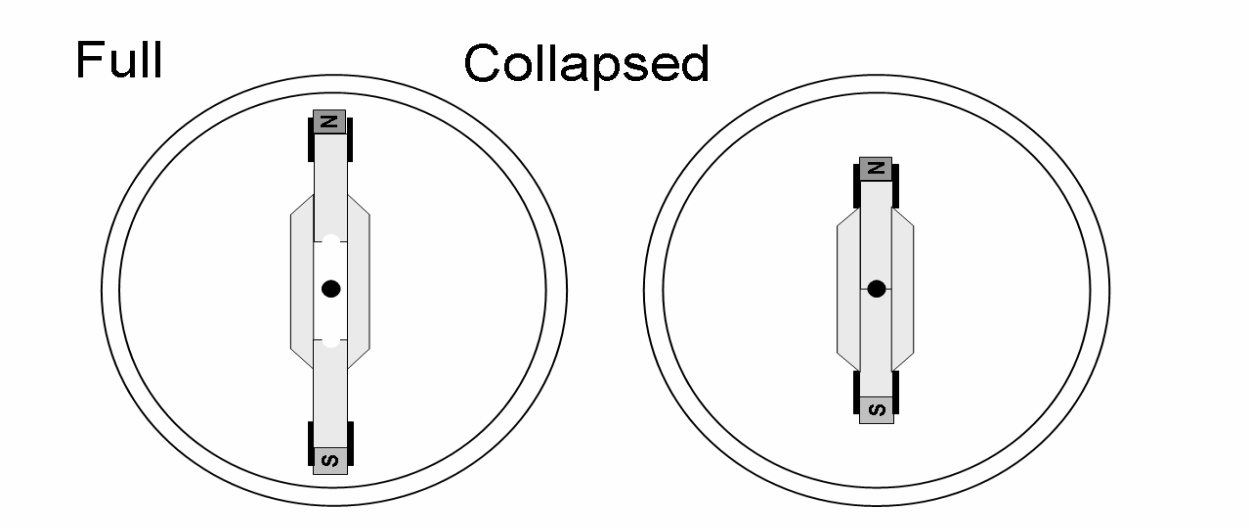

Figure 40. A telescoping magnet bar that enables the magnets to retract as they pass by obstructions

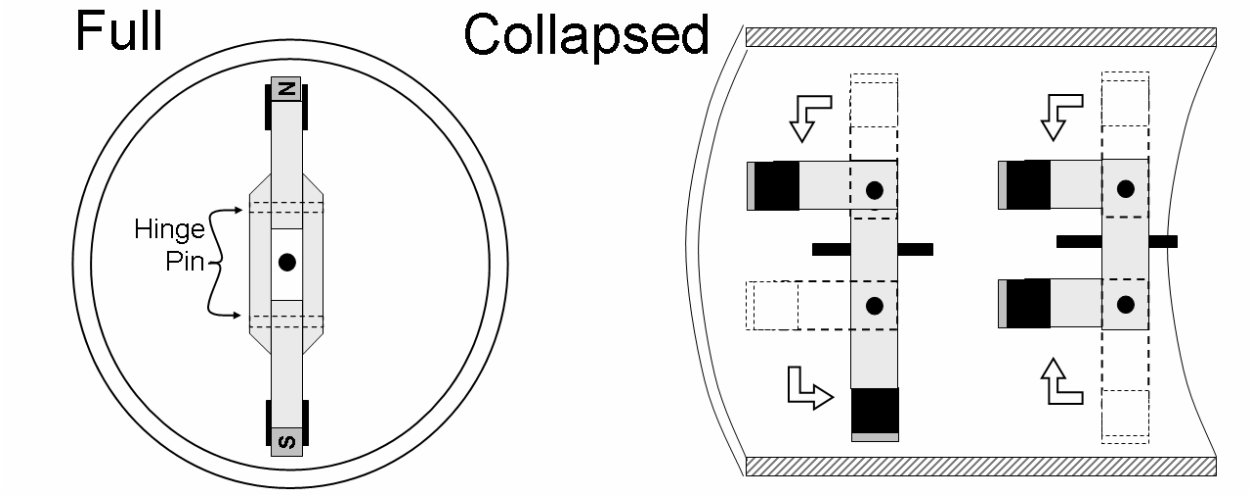

Figure 41. A hinged structure that enables the magnets to retract as they pass by obstructions

7.4.1 Hinged magnet bar configuration

The hinged configuration is shown schematically in Figure 42. The magnetizer could be designed to fit through obstructions that are less than one-third the pipe diameter. In a two-pole magnetizer configuration, the hinged magnetizer could easily pass a plug valve. The extension can be designed to be activated by rotation with retraction assisted by springs.

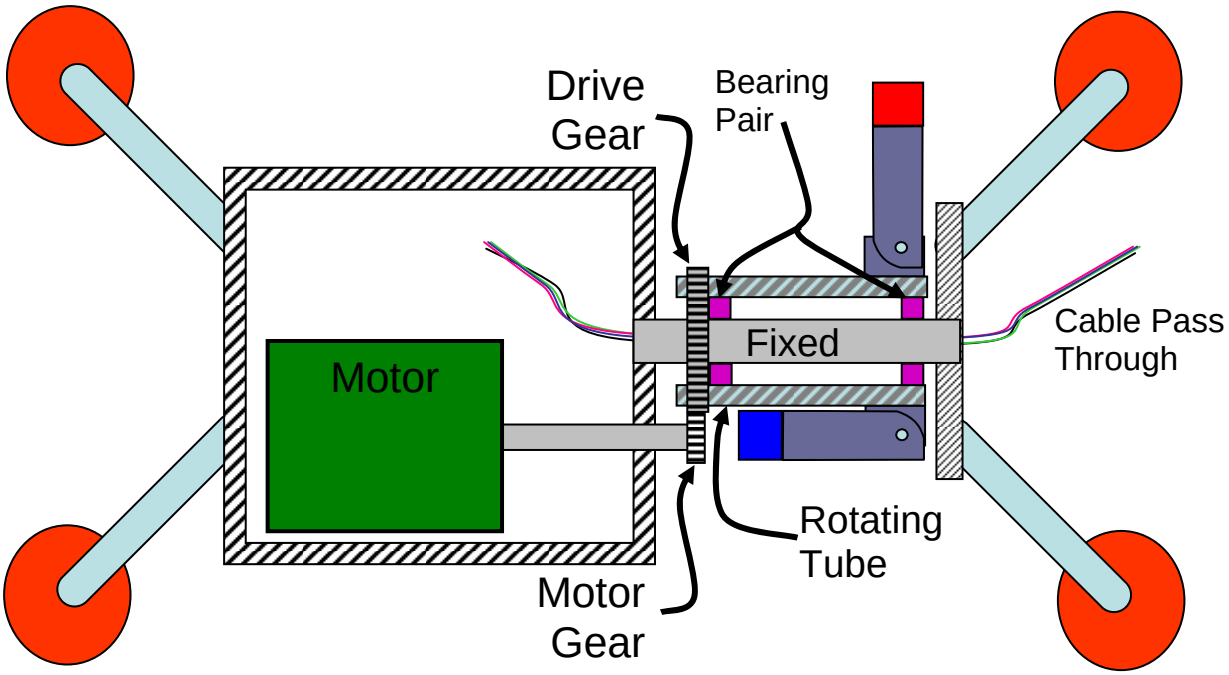

Figure 42. Hinged configuration with an outer tube rotating around a fixed tube

7.4.2 Telescoping magnet bar configuration

A magnet system can also be designed to pass obstructions using a telescoping magnet bar configuration. As illustrated in the front and side view in Figure 43, each magnet is attached to a pole piece that is roughly a quarter of the extent of the entire magnet bar. Each pole piece fits snuggly into a sleeve that has low friction guides and pins to keep the pole piece from leaving the sleeve. The wall thickness of the sleeve is defined by the area of the magnet and the pole piece. For example, for a 1-inch x 1-inch magnet, the wall thickness must be at least 0.207 inches. A good design would include 10 to 25 percent more material; therefore a wall thickness of 0.25 inches will be appropriate[5]. A spring is useful in maintaining the magnet in full extension position; however the attraction force between the pipe and magnet keeps the spring force requirement low.

[5] The other dimension of the sleeve is 1.5 inches. The base area is 2.25 square inches. The area of the pole piece is 1 square inch. Therefore 1.25 square inches of material is available to carry flux to the 1 square inch pole piece.

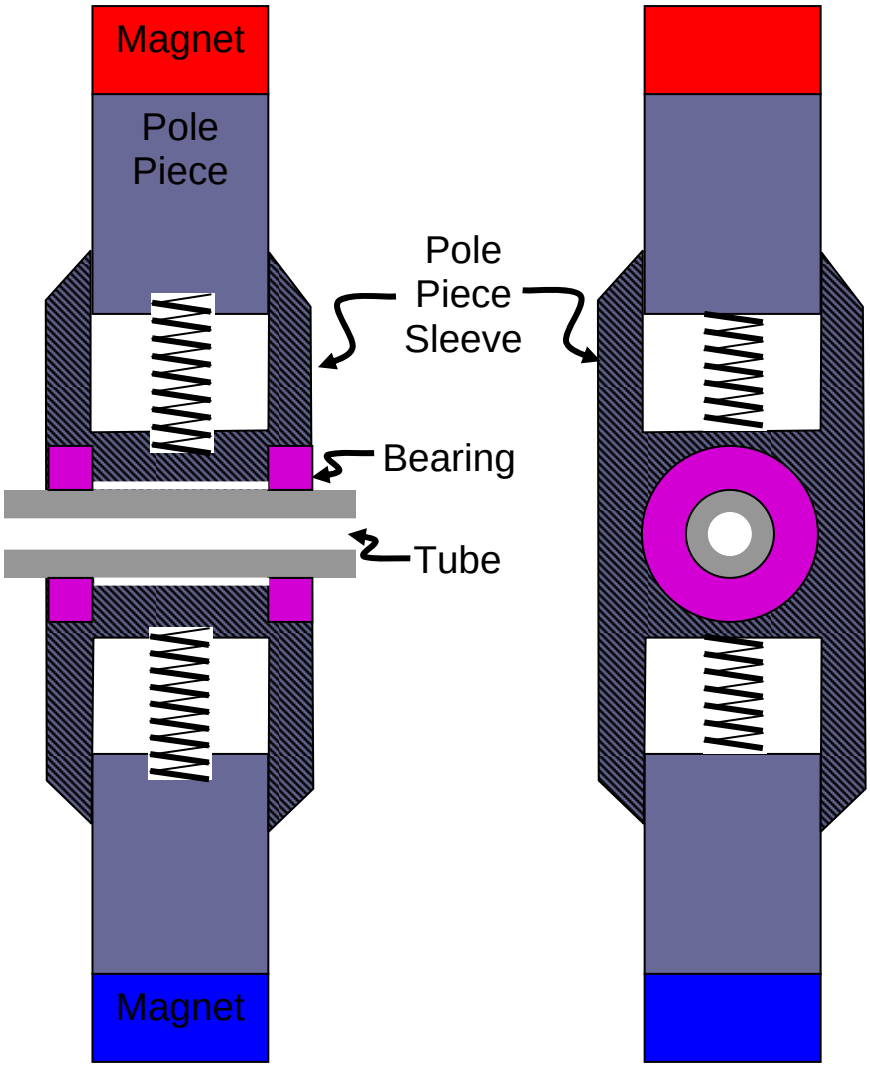

Figure 43. Retractable pole piece

Range of Collapse. The amount the magnet bar can collapse is a function of the diameter of the pipe and the thickness of the magnets. The key design constraint is that the magnet cannot enter the sleeve. Using a 12-inch inside pipe diameter configuration as an example, as illustrated in Figure 44, the inspection diameter would be 10 inches with the optimum 1 inch liftoff. Each magnet bar can retract another 1.5 inches so that in the stationary position, the minimum size would be 7 inches.

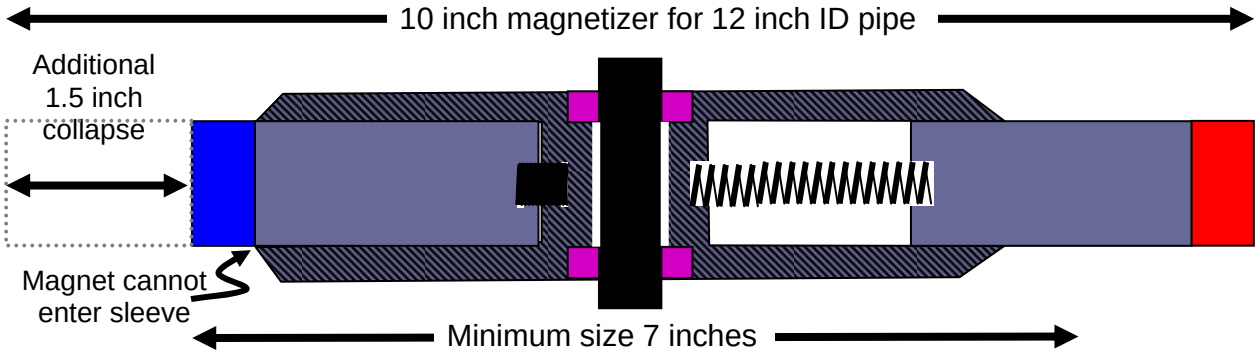

Figure 44. Retraction potential for a 12 inch diameter pipe

Table 5 shows the potential collapsible magnet bar configurations for pipe diameters ranging from 8 inches to 18 inches. Two values are given, one for inspection diameter and the other for minimum diameter. The inspection dimension in inches assumes a 1 inch liftoff. The percentage value is the percentage obstruction that a tool could negotiate. It should be noted that the pipe inner diameter is controlled for pipe 12 inches or less and outside diameter is controlled for pipe greater than 12-inches in diameter.

Table 5. Collapsible magnet bar configurations for pipe diameters ranging from 8 to 18 inches

Pipe Diameter	Magnet Thickness	Inspection Diameter (1 inch liftoff)		Minimum Diameter (Full Collapse)	
Inches	Inches	Inches	Percent	Inches	Percent
8	0.5	6	25%	5	38%
10	0.5	8	20%	6	40%
12	0.5	10	17%	7	42%
14	0.5	12	14%	8	43%
16	0.5	14	13%	9	44%
18	0.5	16	11%	10	44%
12	1.0	10	17%	8	33%
14	1.5	12	14%	9	36%
16	1.5	14	13%	10	38%
18	1.5	16	11%	11	39%

7.5 Protective Boot

Direct contact between the magnet and the pipe should be avoided. A method that isolates the rotating magnet from the pipe using a boot attached to the stationary parts of the system is illustrated in Figure 45. While illustrated for the telescoping configuration, the boot concept can work equally well for the hinged system. The magnetizer is free to spin within the boot; however to pass a severe obstruction, the rotation needs to be stopped. In this design, there are two ways to control the rotation and stop as necessary. First, if the deflection of the wheeled support arm on the carriage exceeds a threshold, power to the motor can be interrupted. If the obstruction is more localized and not detected by the carriage arms, the boot will be forced into the spinning magnetizer causing it to stop. Since the rotational speed is continuously monitored, a sudden drop in speed would indicate an obstruction and the system controller would interrupt power to the motor. To pass large obstructions, with the magnet rotation stopped, the boot can force the magnet pole piece into the sleeve. The cup material can be made from polyurethane, a material commonly used on current pipeline inspection tools. Note that in Figure 45, a second gear was added to center the motor, as discussed previously in the motor and rotating assembly section of this report.

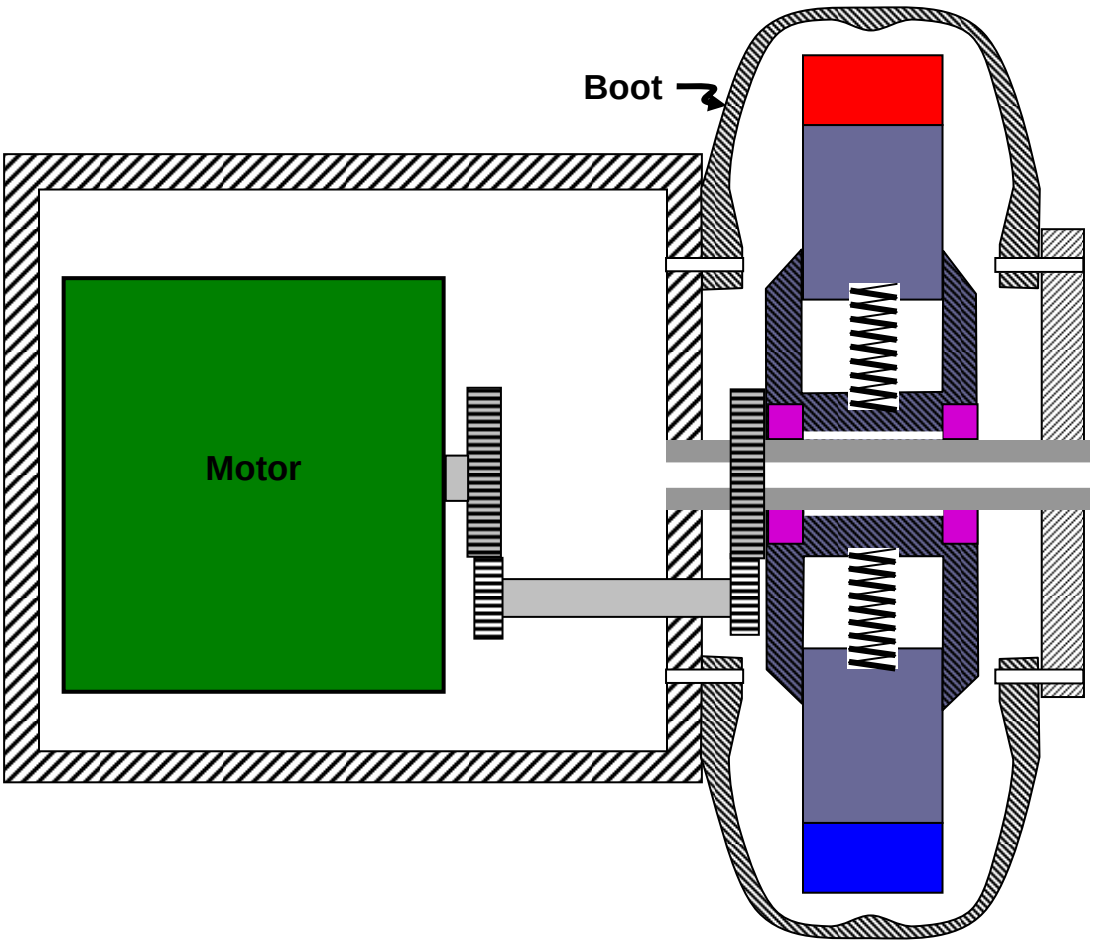

Figure 45. Stationary protective boot surrounding the magnet

7.6 Design Summary

The rotating permanent magnet inspection system is feasible for pipes ranging in diameter from 8 inches to 18 inches using a two pole configuration. Experimental results and theoretical calculations provide the basis for selection of the critical design parameters. The parameters include a significant magnet to pipe separation that will facilitate the passage of pipeline restrictions. With the basic values of critical components established, the next step is a detailed mechanical design of a pipeline ready inspection system.

8 Potential Implementation

With a general understanding of this new technology established, the final step of this program was to determine whether a practical implementation could be designed and fabricated. The design goals included collapsibility and low electrical power consumption. The system must collapse to fit through a 50 percent diameter restriction such as a plug valve. The electrical power goal was to draw less than 50 watts. The system also features a central tube for routing electrical power and data cables.

The feasibility of this new inspection technology was demonstrated with a hinged rotating magnet system designed to inspect a 12 inch pipe, shown in Figure 46. The system was designed to potentially mate to a pipeline crawler system currently under development in another research program.

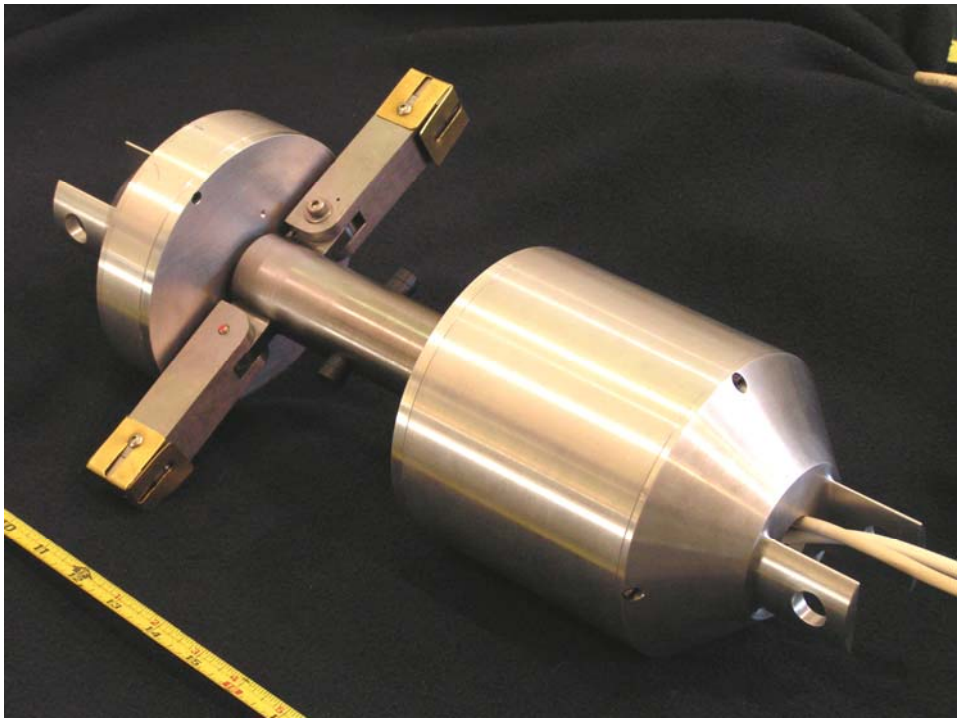

Figure 46. Rotating permanent magnet inspection device for a twelve inch pipe

The magnet bars fold out during inspection and retract to negotiate obstructions. In the collapsed configurations, the unit is less than 5 inches in diameter. The inspection system was tested using the same supports and sensors used in the previous benchmark studies, as shown in Figure 47.

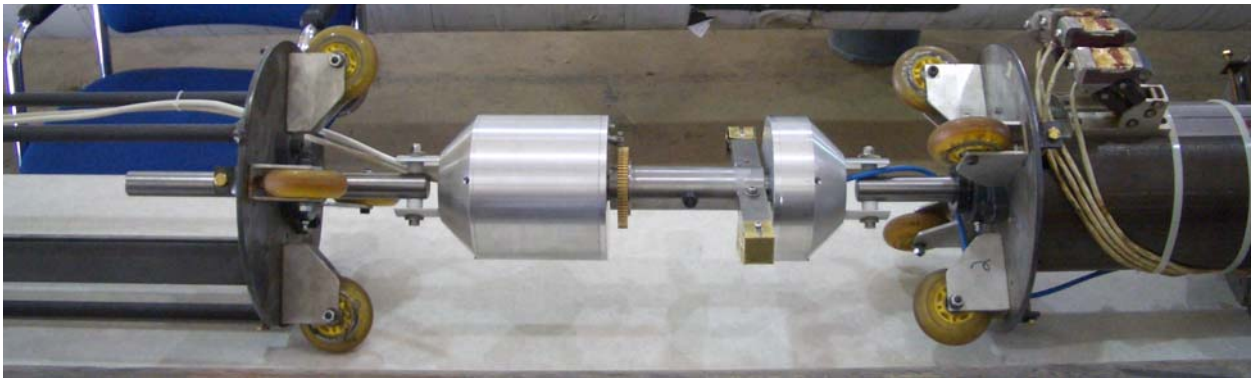

Figure 47. The collapsible magnetizer mounted between centering carriages for testing in a 12-inch pipe

Magnet arms rotate on a stationary center tube, shown in green in Figure 48. This tube is hollow enabling cables to be routed through the center. The magnet bars are mounted on a concentric spindle (blue), with low friction bearings (gold) enabling smooth rotation. The pulling force needed to propel the unit in the pipe translates through this tube; the rotating objects are isolated from lateral forces which can quickly wear out bearings.

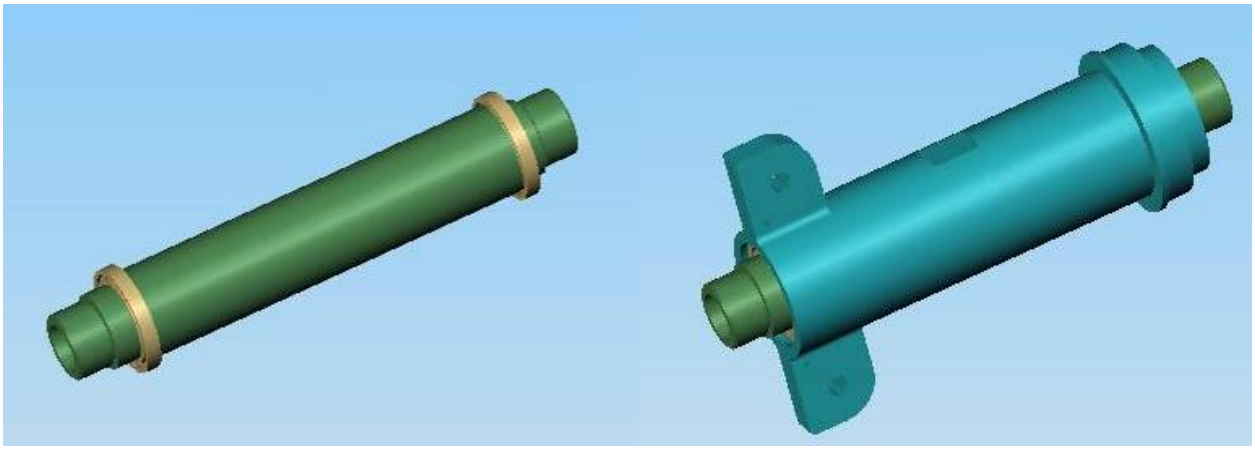

Figure 48. Stationary center tube (green) and concentric spindle (blue) for mounting hinged magnet bars. Low friction bearings (gold) enable smooth rotation

The magnets automatically extend by centrifugal force when the magnet tube starts spinning. Springs, illustrated in Figure 49, are used to retract the magnet bars to the collapsed position when spinning stops.

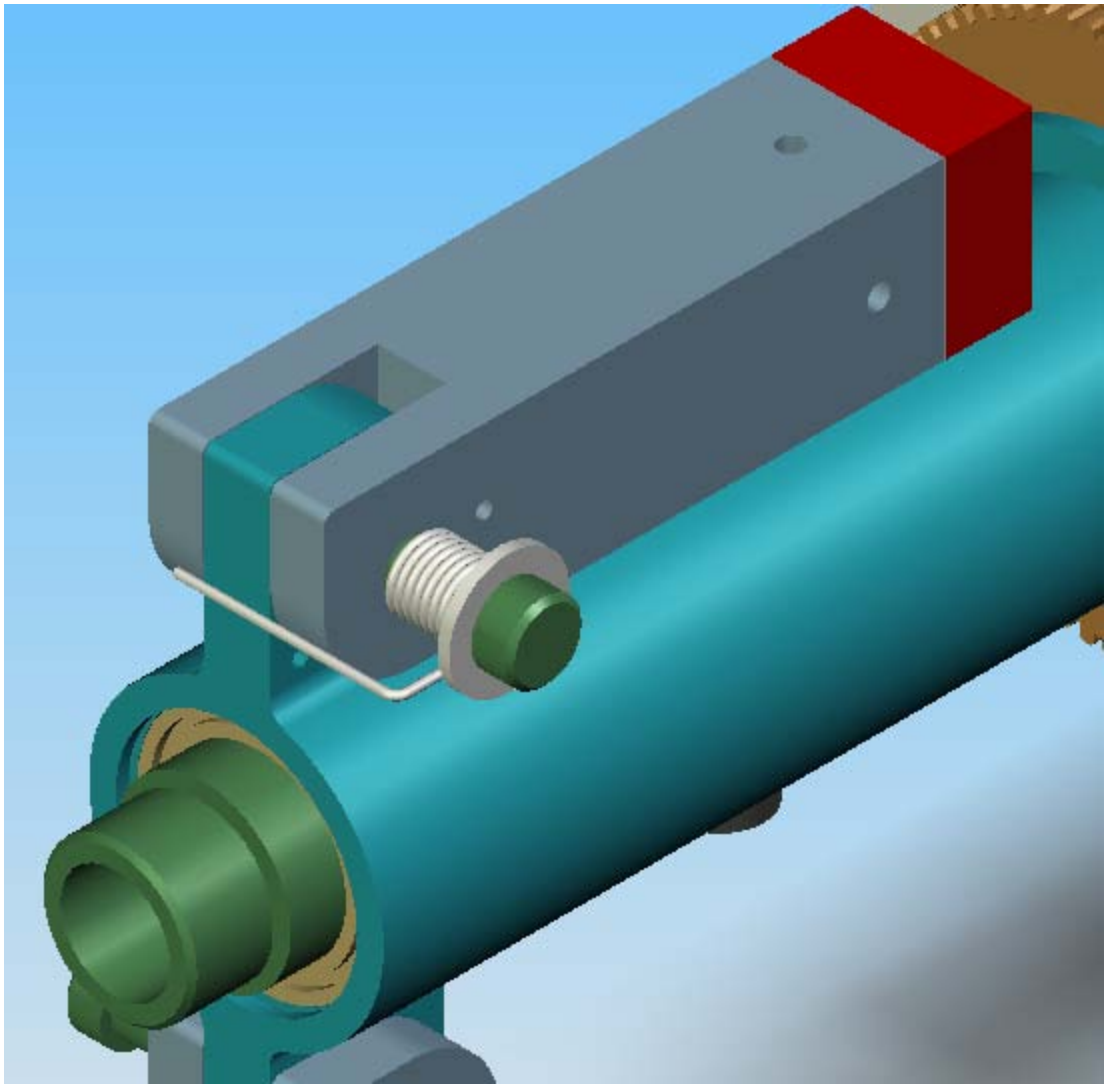

Figure 49. Spring system for returning hinged magnet to the collapse position. Centripetal force overcomes the magnet force.

A small tuned motor, shown in Figure 50 was used to achieve rotational speeds up to 6 hertz. The power consumption was nominally 6 watts. The small motor gear turns an external gear on the magnet bar spindle. A 24 volt DC motor controller is mounted next to the motor inside a seal housing.

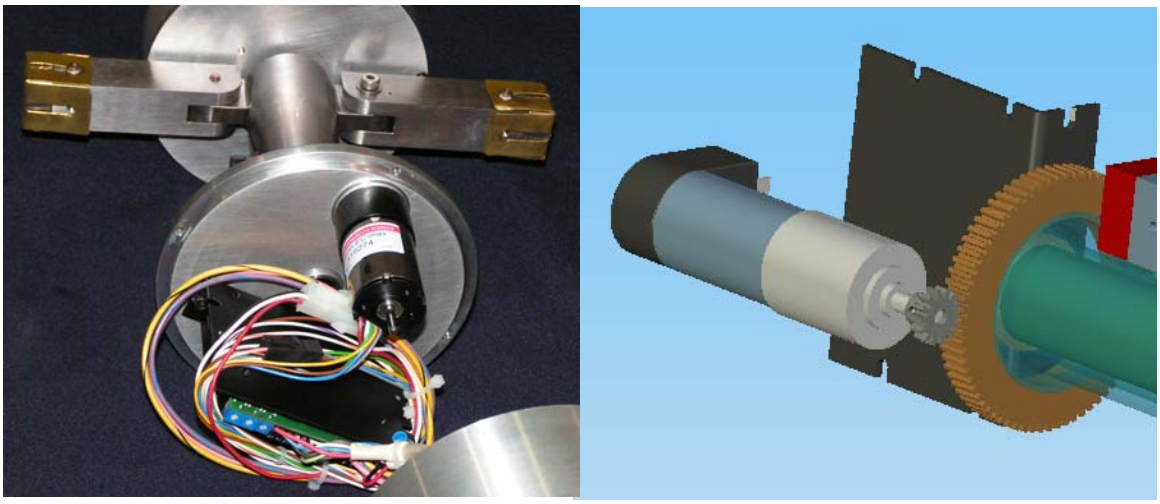

Figure 50. Small dedicated motor and controller for spinning magnets. The power requirement is less than 6 watts.

The fabrication of this unit demonstrated the feasibility of this inspection method. As with any initial design, changes can be made that will incrementally improve performance. For example, the magnetic performance was not quite as strong as solid magnet bars; adding hinge loops from the spindle to the outside of the pivoting magnet bars should overcome this slight deficiency. While not optimal, this initial design did produce results comparable to the laboratory prototype. Figure 51 shows the result from MC1, an 80 percent deep, 3 inch wide, 1.2 inch long metal loss

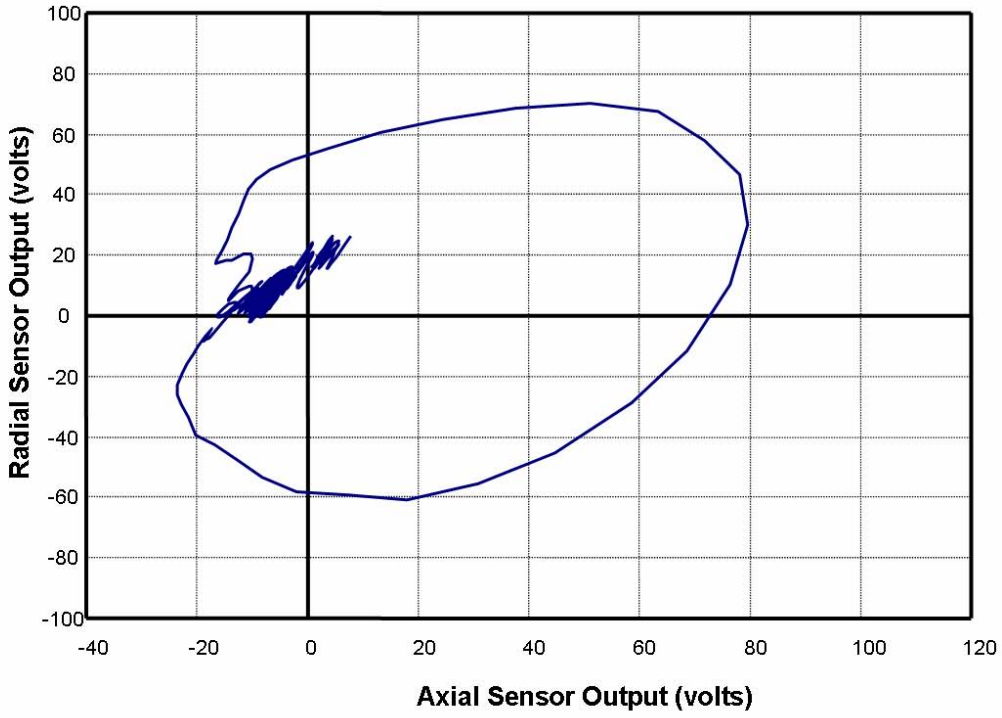

Figure 51. Response from metal loss anomaly using low power RMPI magnetizer

9 Conclusions

A new inspection method was developed called rotating permanent magnet inspection (RPMI). This patent pending technology employs pairs of permanent magnets rotating around the central axis of a cylinder to induce high current densities in the material under inspection. Experimental results have shown that metal loss anomalies and wall thickness variations are detected with an array of sensors that measure local changes in the magnetic field produced by the induced current flowing in the material. The design exploits the phenomenon that circumferential currents are easily detectable at pipe diameters from the magnets. Current changes at anomalies were detectable with commercial, low cost Hall Effect sensors. Commercial analog to digital converters can be used to measure the sensor output and data analysis can be performed in real time using PC computer systems. The technology was successfully demonstrated during two blind benchmark tests where numerous metal loss defects were detected. For this inspection technology, the detection threshold is a function of wall thickness and corrosion depth. For thinner materials, the detection threshold was experimentally shown to be comparable to magnetic flux leakage. For wall thickness greater than three tenths of and inch, the detection threshold increases with wall thickness. The potential for metal loss anomaly sizing was demonstrated in the second benchmarking study; accuracy comparable to magnetic flux leakage was found.

The rotating permanent magnet system has the potential for inspecting unpigable pipelines since the magnetizer configurations can be sufficiently small with respect to the bore of the pipe. This allows the RPMI system to pass obstructions that limit the application of many inspection technologies. Also, since the largest dimension of the Hall Effect sensor is two tenths of an inch, the sensor packages can be small, flexible and light. The power consumption on the order of ten watts is low compared to some inspection systems; this would enable autonomous systems to inspect longer distances between charges.

This report provides the foundation the RPMI method. The excellent agreement of experimental results with the finite element modeling and analytical model derived from basic theory will help facilitate future developments. While many engineering challenges must be addressed to implement this technology, this new method may provide another tool to help pipeline companies ensure the safe and reliable delivery of energy products.

10 References

1. Nestleroth, J.B. and Bubenik, T. A., “Magnetic Flux Leakage (MFL) Technology for Natural Gas Pipeline Inspection,” Battelle, Report Number GRI-00/0180 to the Gas Research Institute, February 1999.

2. Dobmann, G. and Höller, P., “Physical Analysis Methods of Magnetic Flux Leakage,” in Research Techniques in Nondestructive Testing, Volume IV, edited by R. S. Sharpe, Academic Press, 1980.

3. Krautkramer, J, Ultrasonic Testing of Materials, Springer Verlag, 1977.

4. Reber, K, M. Beller, O.A. Barbian, and N. Uzelac, “A New Generation of Ultrasonic Inspection Tools; How Defect Assessment Methods Influenced Design,” The Pipeline Pigging, Integrity Assessment and Repair Conference, Feb 2002.

5. Williams, H.H., O.A. Barbian, and N.I. Uzelac, “Internal Inspection Device for Detection of Longitudinal Cracks in Oil and Gas Pipelines,” ASME International Pipeline Conference, Calgary, 1996.

6. “Remote Field Eddy Current Inspection: A Selective NTIAC Bibliography,” Materials Evaluation, Vol. 47, No 1, Jan 1989, pp 29-31.

7. Nestleroth, J.B., “Remote Field Eddy Current Detection of Stress-Corrosion Cracks in Gas Transmission Lines,” British Journal of NDT, Vol. 35, No 5, May 1993.

8. Atherton D.L., L. Clapham, W. Czura, B.J. Mergelas, and S. Smith, “Remote Field Eddy Current Defect Interaction” Final Report, Gas Research Institute, GRI-95/0506, March 1996.

9. Atherton D.L., L. Clapham, W. Czura, et al., “Factors Affecting Pipeline Flaw Detection and Measurement,” Final Report, Gas Research Institute, GRI-97/0264, May 1997.

10. Dodd, C.V., W.E. Deeds, and L.D. Chitwood 1988. “Eddy Current Inspection of Ferromagnetic Materials Using Pulsed Magnetic Saturation,” Materials Evaluation, Vol. 46, 1988, pp. 1592-97.

11. Stalenhoef, J.H.J. and J.A. De Raad, “MFL and PEC tools for plant inspection,” Insight, Vol. 42, No. 2, 2000, pp. 74-77.

12. Robers, M.A. and R. Scottini, “Pulsed Eddy Currents in Corrosion Detection,” 8th ECNDT, Barcelona, June 2002.

13. “Pipeline Inspection Technologies Demonstration Report 2004,” available from Department of Energy, National Energy Technology Laboratory. http://www.netl.doe.gov/scngo/

14. Pipeline Inspection Technologies Demonstration Report 2006," available from Department of Transportation, Pipeline & Hazardous Materials Safety Administration.. http://primis.phmsa.dot.gov/rd/demos/010906_OH/DTRS56_05_T_0003_Benchmark_Final.pdf

15. INNOVATIVE ELECTROMAGNETIC SENSORS FOR PIPELINE CRAWLERS" Technical Progress Report November 2005 NETL Award No. DE-FC26-03NT41881 www.osti.gov/servlets/purl/875411-kFoVvp/

Appendix A
Pull Away Tests

The goal of the rotating magnetizer is to produce a uniform current of appreciable magnitude. The magnetic field in the pipe has two parts, each with distinct properties and effects. One part is the direct magnetic field from the strong permanent magnets. The second field is due to the current flowing in the pipe. Near the rotating magnets, the direct field from the magnet is dominant and produces a saddle-shaped alternating signal. Farther away from the magnets, magnetic field caused by the currents flowing in the pipe dominates. Figure A-1 shows the magnetic field at the inside surface of the pipe at distances ranges from close to the magnetizer to 2.5 pipe diameters away for a two-pole system in a 12-inch pipe spinning at 5 hertz. The field due to direct field is negligible at distance greater than one pipe diameter (1D) and the measured signal is nearly sinusoidal. The axial field is also strong, on the order of a gauss. The currents are detectable at distances beyond 2 pipe diameters. Figure A-2 shows the magnetic field at the inside surface of the pipe at distances ranging from close to the magnetizer to 1.5 pipe diameters away for a four-pole system in a 12-inch diameter pipe spinning at 2.5 hertz.

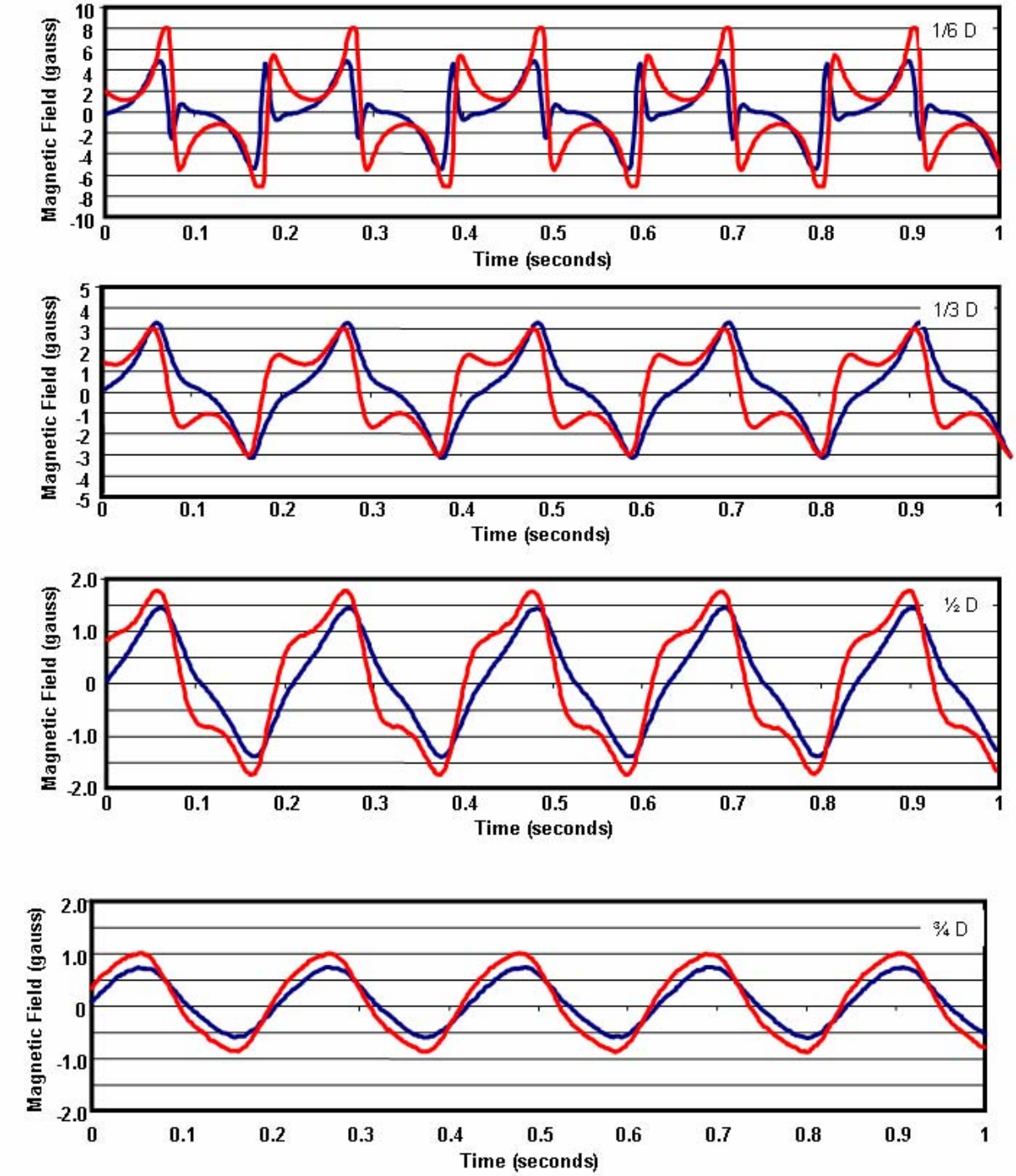

Figure A-1. Magnetic field at the inside surface of the pipe at distances ranges from close to the magnetizer to 2.5 pipe diameters away for a two-pole system in a 12-inch pipe spinning at 5 hertz

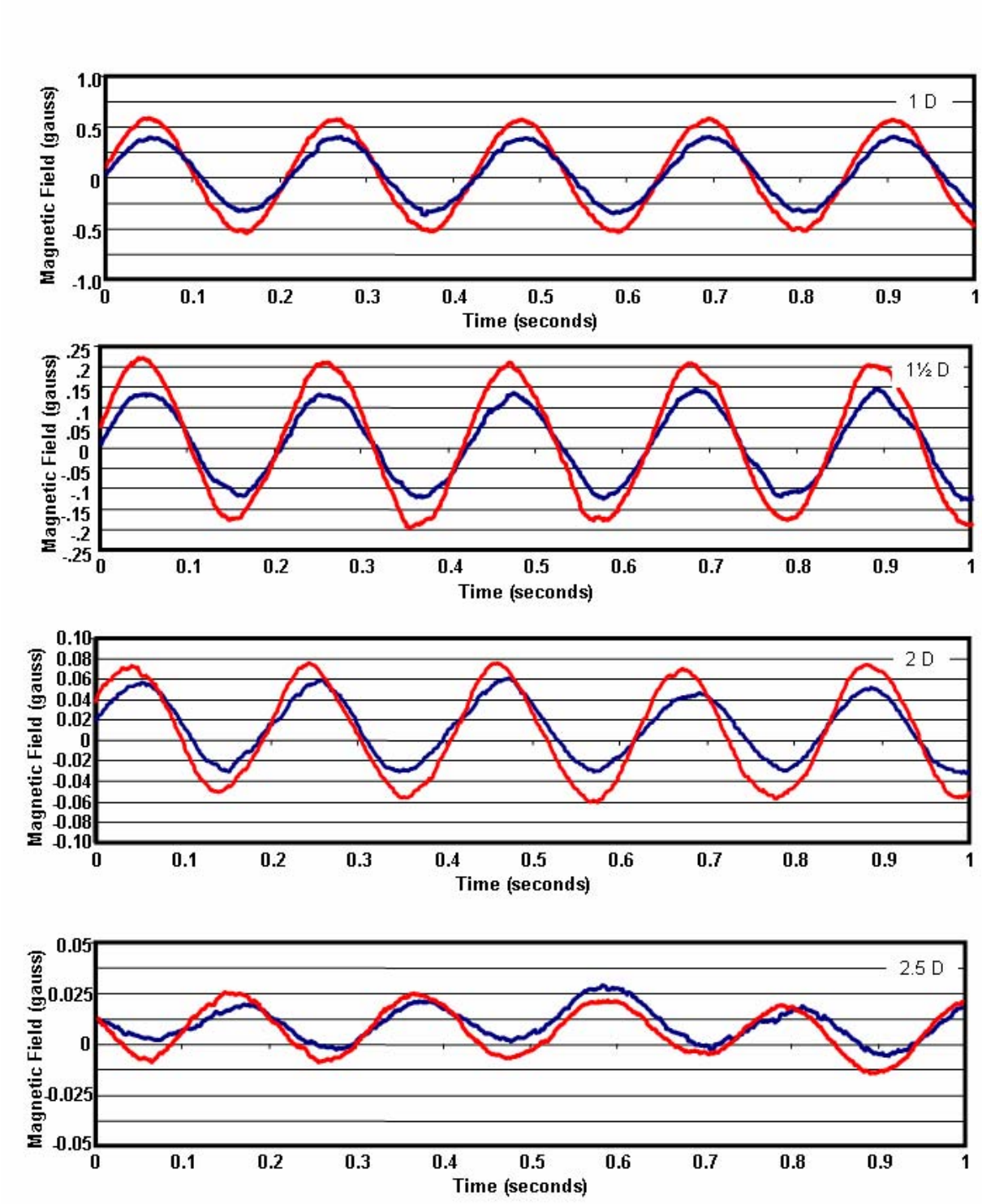

Figure A-1 (cont). Magnetic field at the inside surface of the pipe at distances ranges from close to the magnetizer to 2.5 pipe diameters away for a two-pole system in a 12-inch pipe spinning at 5 hertz

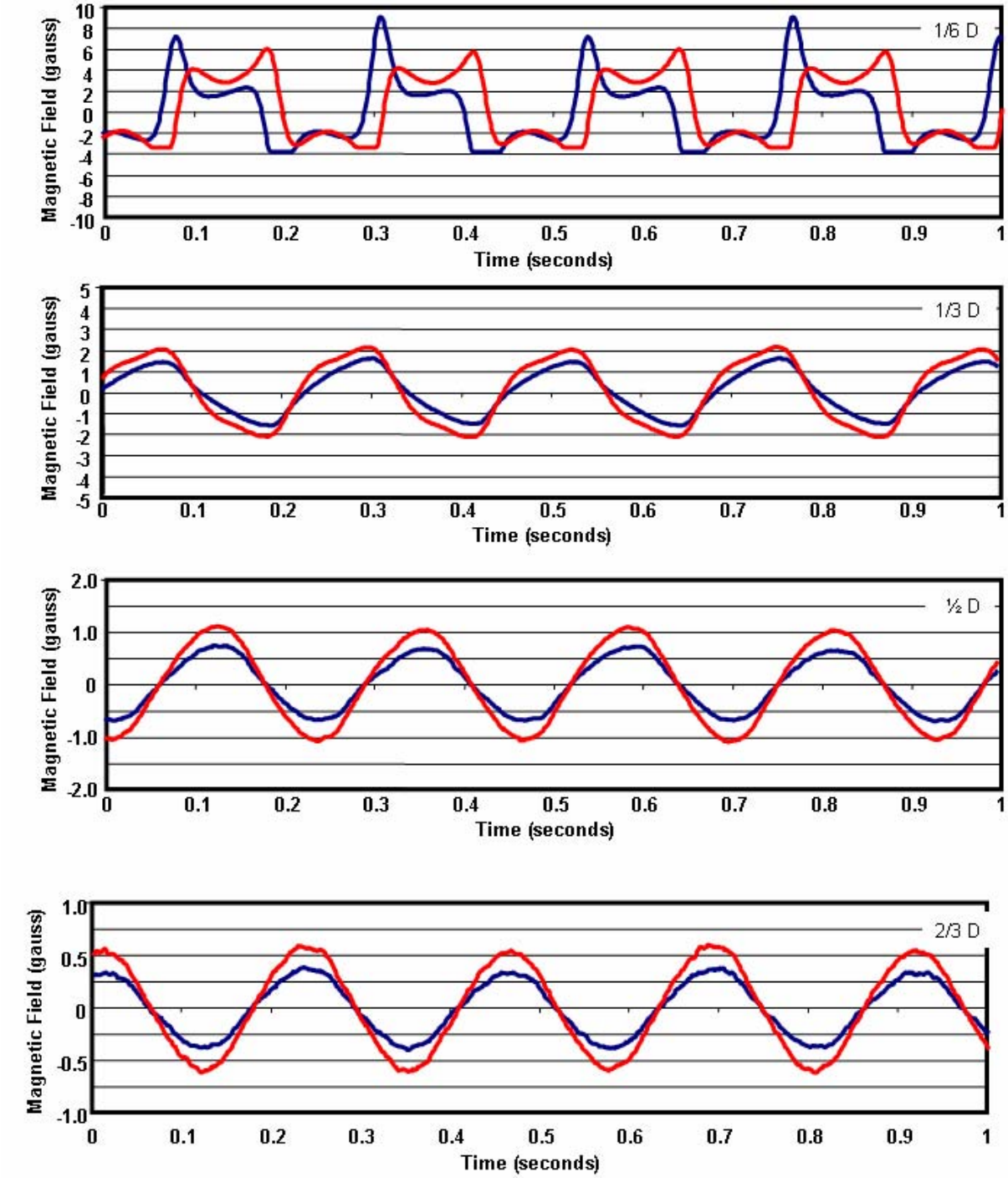

Figure A-2. Magnetic field at the inside surface of the pipe at distances ranges from close to the magnetizer to 1.5 pipe diameters away for a four-pole system in a 12-inch pipe spinning at 2.5 hertz

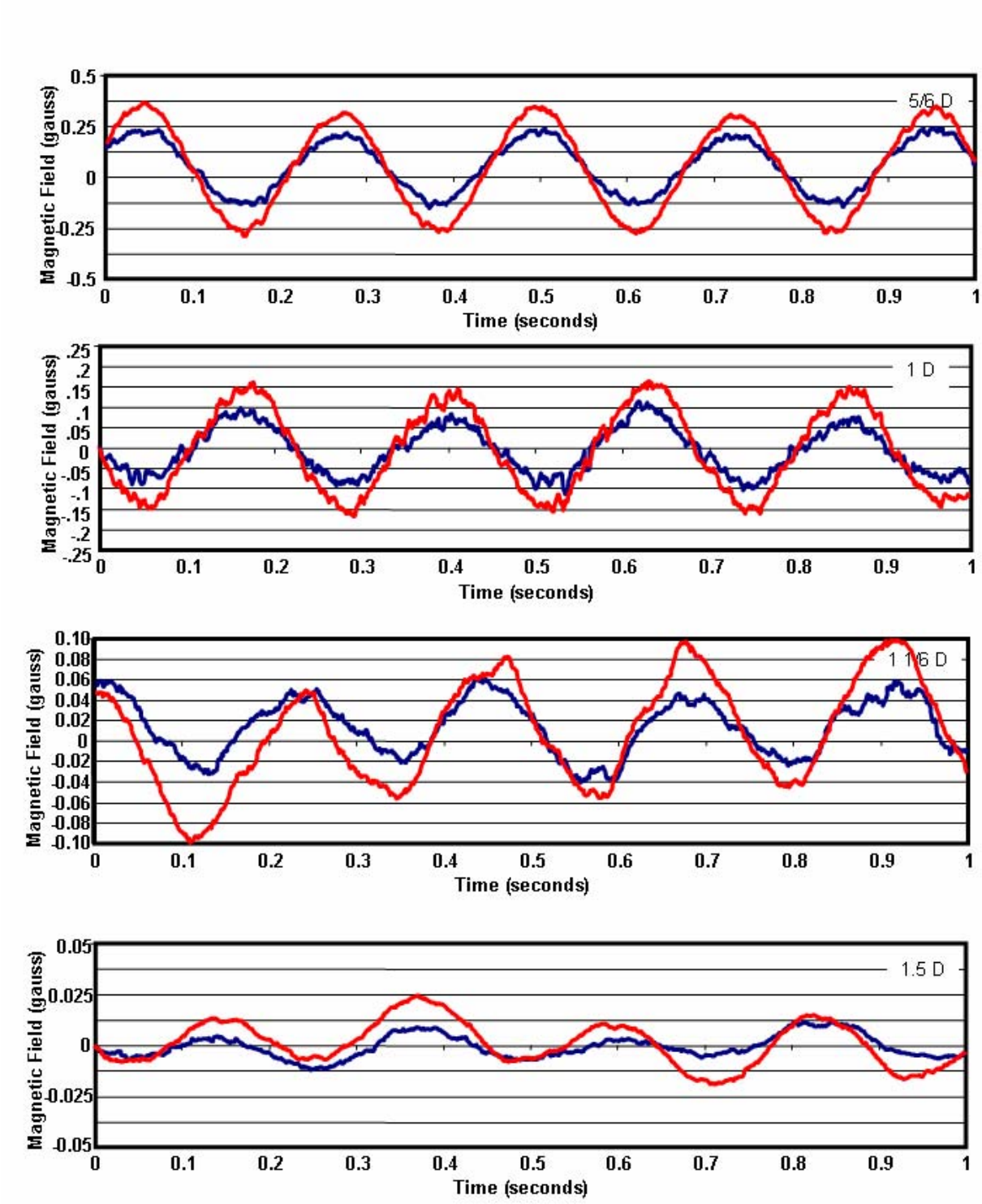

Figure A-2 (cont). Magnetic field at the inside surface of the pipe at distances ranges from close to the magnetizer to 1.5 pipe diameters away for a four-pole system in a 12-inch pipe spinning at 2.5 hertz

Appendix B
Signal Processing

Signal Processing

A rotating permanent magnet is used to induce a magnetic field in the pipe wall under inspection. The resulting eddy currents that flow in the pipe wall produce a secondary magnetic field that can be measured at a sufficient distance from the primary magnetic field. Defects in the pipe wall cause localized changes in flux density in the area of the defect. A Hall sensor located in the area of the secondary field can be used to measure the field disturbance due to the pipe wall defect. Finite-element state modeling of the system has shown that the secondary magnetic field produced is sinusoidal in nature with a fundamental frequency that is given by the rotational speed of the two-pole permanent magnet. Based on an observation of experimental data, the effect of a pipe wall defect on the measured magnetic field is to modulate the amplitude of the sinusoidal signal in a manner that is proportion to the defect size. Calculating the amplitude of the measured field strength while the system moves though the pipe can provide information about the location and severity of wall defects.

This project examined three potential signal processing approaches for determining the signal amplitude (hence, the pipe wall defect profiles) from measurements of the field strength using a linear output Hall Effect sensor located in the secondary magnetic field. Simulation results are provided that shows the performance of each method with varying simulation parameters (noise, crawler speed, rotor speed, and rotor speed deviation).

The signal processing problem can be stated as follows. We wish to accurately determining the amplitude of the measured magnetic field in the presence of noise. The measured signal can be written as,

$$x(t) = r(t) + \eta(t), \tag{B1}$$

where, *x(t)* is the measured signal, *r(t)* is the sinusoidal signal for which the amplitude is to be estimated, and $\eta(t)$ is the noise component. The sinusoidal signal *r(t)*, can be written as;

$$r(t) = A(t) \cdot \cos(\omega_c t + \theta), \tag{B2}$$

where, *A(t)* is the amplitude, which is a function of time (distance along the pipe), ω_c is the angular frequency, and θ is the phase.

The signal processing problem is to accurately estimate *A(t)* given measurements of the signal *x(t).*

Lock-in Amplifier Method (Synchronous AM Demodulation)

Observing that Equation B2 is in the form of a Double Sideband – Suppressed Carrier, Amplitude Modulated (DSB-SC AM) signal, led to the investigation of AM demodulation techniques to estimate (recover) the signal amplitude *A(t).* In DSB-SC AM demodulation, a reference sinusoid is used to demodulate a message signal from a carrier. The difficulty with this technique is in generating a reference that is both at the proper frequency and in phase with the input signal. A Phase Locked Loop (PLL) is often used for this purpose. The PLL employs a

feedback loop to "lock" onto the input signal and maintain the reference output at the proper frequency and at a constant phase relationship to the input.

A similar device that is employed which is essentially the same method to demodulate the input is known as a lock-in amplifier.

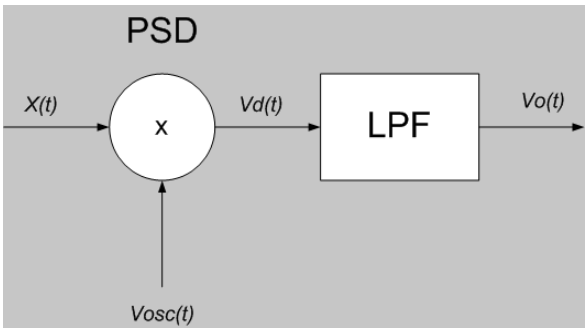

Figure B-1. Lock-in Amplifier Block Diagram.

A block diagram of a lock-in amplifier (LIA) is shown in Figure B-1. The LIA consists of a phase sensitive detector (PSD), which is nothing more than a multiplier, and a low-pass filter (LPF). The LIA utilizes a reference oscillator to produce a sinusoidal signal with the same angular frequency as the signal of interest. For synchronous AM demodulation a PLL is employed to generate *Vosc(t)* with fundamental frequency ω_c and phase angle θ_o, that is related to the phase θ by a constant. That is, $(\theta - \theta_o) = C$, and ideally $C = 0$. The PLL implements closed loop feedback that keeps *Vosc(t)* "locked" with the input even for variations in input frequency. For the LIA, the phase of *Vosc(t)* is either determined by experiment or *Vosc(t)* is derived from the same source as the input. For the experimental method, the oscillator phase is adjusted until maximum output is achieved.

The detected signal can be derived as follows. The oscillator output, with amplitude $A_{osc,}$ is given as

$$Vosc(t) = A_{osc} \cdot \cos(\omega_c t + \theta_o)\,. \tag{B3}$$

Therefore, the output of the PSD is given by

$$Vd(t) = A(t) \cdot A_{osc} \cdot \cos(\omega_c t + \theta) \cdot \cos(\omega_c t + \theta_o) + \eta(t) \cdot A_{osc} \cdot \cos(\omega_c t + \theta_o)\,. \tag{B4}$$

It is convenient to ignore the term associated with the noise so that,

$$Vd'(t) = A(t) \cdot A_{osc} \cdot \cos(\omega_c t + \theta) \cdot \cos(\omega_c t + \theta_o)\,. \tag{B5}$$

Using a trigonometric identity, Equation B5 can be rewritten as,

$$Vd'(t) = .5 \cdot A(t) \cdot A_{osc} \cdot \cos(\theta - \theta_o) + .5 \cdot A(t) \cdot A_{osc} \cdot \cos(2\omega_c t + \theta + \theta_o)\,. \tag{B6}$$

Passing this signal through an ideal low-pass filter (LPF) with a cutoff frequency less than $2\omega_c$ and with bandwidth *W* that is the bandwidth of *A(t)* will produce the output

$$Vo'(t) = .5 \cdot A(t) \cdot A_{osc} \cdot \cos(\theta - \theta_o)\,. \tag{B7}$$

Assuming that $(\theta - \theta_o) = 0$, and letting $A_{osc} = 1$, the output is the desired result

$$Vo'(t) = \frac{A(t)}{2}\,. \tag{B8}$$

Taking into account the noise term present in Equation B4, it can be shown that

$$Vo(t) = \frac{A(t)}{2} + \frac{n_c(t)}{2}, \tag{B9}$$

where, $n_c(t)$ is the "in-phase" component of the noise which has the same power content as $\eta(t)$ and for zero mean, white Gaussian noise, the signal to noise ratio is given by

$$SNR = \frac{P_A}{W \cdot N_o}. \tag{B10}$$

Here, P_A is the power in $A(t)$, W is the bandwidth of the LPF and N_o is the variance of $\eta(t)$.

Vector Subspace Method

Using a trigonometric identity, Equation B2 can be rewritten as:

$$r(t) = A(t) \cdot [\cos(\omega_c t) \cdot \cos(\theta) - \sin(\omega_c t) \cdot \sin(\theta)], \tag{B11}$$

$$r(t) = A(t) \cdot \cos(\theta) \cdot \cos(\omega_c t) - A(t) \cdot \sin(\theta) \cdot \sin(\omega_c t), \tag{B12}$$

$$r(t) = a \cdot \cos(\omega_c t) - b \cdot \sin(\omega_c t). \tag{B13}$$

It follows that,

$$a = A(t) \cdot \cos(\theta), \tag{B14}$$

$$b = A(t) \cdot \sin(\theta), \tag{B15}$$

$$A(t) = sqrt(a^2 + b^2), \tag{B16}$$

and

$$\theta = \arctan(b/a). \tag{B17}$$

After analog-to-digital conversion the measure signal is given as:

$$x(n) = r(n) + \eta(n) \tag{B18}$$

and

$$r(n) = a \cdot \sin(\omega_c nT) - b \cdot \cos(\omega_c nT). \tag{B19}$$

Given the sample time T and N samples, $r(n)$ can be written in matrix-vector form as follows,

$$\begin{bmatrix} r(0) \\ r(1) \\ \vdots \\ r(N-1) \end{bmatrix} = \begin{bmatrix} \sin(0) & -\cos(0) \\ \sin(\omega_c T) & -\cos(\omega_c T) \\ \vdots & \vdots \\ \sin(\omega_c [N-1]T) & -\cos(\omega_c [N-1]T) \end{bmatrix} \cdot \begin{bmatrix} a \\ b \end{bmatrix}, \tag{B20}$$

$$\vec{r} = A \cdot \vec{v}. \tag{B21}$$

If we had samples of $r(n)$ we could solve for $\vec{r}$; however, since we only have samples of $x(n)$ we must formulate a different problem. Due to the additive noise, it is unlikely that $\vec{x}$ will lie in the column space of A and, therefore, there will not be a solution $\vec{v}$ such that:

$$\vec{x} = A \cdot \vec{v}. \tag{B22}$$

Instead, we pose the problem as follows: we wish to find $\hat{v}$, such that, $\left\| A\hat{v} - \vec{x} \right\|$ is minimized.

From linear algebra, the solution is given by the least squares projection of $\vec{x}$ onto the subspace spanned by the columns of *A*. That is, the projection of $\vec{x}$ onto the subspace of sinusoidal signals with angular frequency ω_c.
The solution can be found using a pseudo inverse as follows:

$$\hat{v} = \left(A^T A\right)^{-1} A^T \cdot \vec{x} \cdot \tag{B23}$$

Processing Complications

SIGNAL BANDWIDTH. The signal represented by Equation 18 is not a typical AM signal due to the fact that the bandwidth, *W* of *A(t)* may be greater than the fundamental frequency ω_c of the carrier signal. The nature of the PM crawler system is such that, the rotational speed of the permanent magnet assembly is slow, on the order of 5Hz, and for certain (sharp) defects the modulating signal could contain much higher frequency content. This poses a problem for the LIA detection approach. Adjusting the ideal LPF cutoff to be equal ω_c would reject frequencies in the modulating signal that are greater than ω_c. The resultant output of the LIA would be a low pass version of *A(t)* and depending on the amount of signal filtered out could result in a poor estimate. This problem could be eliminated by processing *N* samples of the input at a time and then computing an *N*-point FFT of this result. The zero frequency component of the FFT would give an estimate of *A(t*).

VARIABLE ROTOR SPEED. It is likely that the speed of rotation of the magnet assembly will drift as the crawler moves down the pipe due to changes in drive motor applied voltage as well as other factors. To preclude the need to incorporate tight control on motor speed it is desirable that an updated method be incorporated to accommodate any changes in rotor speed and hence fluctuations in ω_c. A sensor could be attached to the rotor to provide an input of rotor speed that could be used to update ω_c periodically. Both of the processing methods discussed above would require this input to account for changes in ω_c unless a PLL was designed that could be used with the LIA method. It is believed that it would be difficult to design a PLL that would work at such low operating frequencies.

Other Methods

Another AM demodulation technique that could be employed to recover *A(t)* is an envelope detector. For the case were $A(t) > 0$, for all *t*, the envelope detector would be a valid approach. An envelope detector is nothing more than a rectifier followed by a low pass filter. However, for reasons previously discussed the low pass filter operation would degrade the estimate of *A(t)*. As with the previous methods, the envelope detector method could be employed on *N* points at a time and an the zero frequency term of an FFT would produce an estimate of *A(t).*

Simulations

We performed several simulations to evaluate the performance of the methods discussed above. The parameters that were investigated for the purpose of simulation were; the rotor speed [Hz], the crawler speed [in/sec], the Signal-to-Noise Ratio (SNR) [dB], the pipe defect size [in], the rotor frequency deviation [Hz/in] and the number of cycles processed [cycles]. The number of

cycles determines the number *N* of points processed at a time to compute the result. The specific parameters used for each simulation are summarized in Table B-1. Simulation results are presented for each case along with a brief discussion of the significance of the results.

Table B-1. Simulation parameters

Parameter	SIM 1	SIM 2	SIM 3	SIM 4	SIM5	SIM6
Rotor Speed [Hz]	5	5	5	5	5	5
Crawler Speed [in/sec]	3	3	1	3	1	1
SNR [dB]	inf	20	20	Inf	20	20
Defect Size [in]	2	2	2	2	2	2
Max Frequency Deviation[Hz/in]	0	0	0	.05	.05	.05
Num Cycles	1	1	2	1	2	1

The pipe profile *A(t)* was modeled with a square wave to simulate defects with sharp edge transitions and with a specific depth. This allowed us to analyze the detection performances based on defect size and severity. Each simulation result shows the pipe wall profile, the modulated sinusoid *r(t)* and the results for the three detection methods.

SIM 1 - IDEAL ESTIMATION. This case is the ideal case where there is no additive noise (infinite SNR) present in the received signal *x(t)* and no frequency deviation (constant rotor speed) as the crawler moves along the pipe. The number of cycles to process for this case was set to 1.0. The results are shown in Figure B-2. All three detectors (LIA, Subspace and Envelope) achieve perfect results. The filter effect of processing *N* samples at a time is also evident by the transients observed as the pipe wall transitions sharply from normal to defect and then back. The filter effect can be reduced by reducing the number of points *N*, however; a minimum number of points (corresponding to cycles of *r(t)*) is required to produce an accurate result.

Figure B-2. Simulation 1 Results

SIM 2 – ADDITIVE NOISE SIMULATION. In this case Gaussian noise was added to *r(t)* such that the SNR was 20 [dB]. This SNR was determined to be comparable to the SNR of measured data taken with a prototype PM crawler system. The SNR achieved in a real system could be worse and is largely dependent upon the rotating magnet configuration. Higher SNR is a function of how close the permanent magnets are to the pipe wall. However, the closer the magnets are the more torque (and ultimately the more power) required to turn the assembly. Since the PM Crawler will operate from a battery source, it is expected that the magnets may need to be backed away from the pipe wall to guarantee enough battery life for an entire inspection run. The results shown in Figure B-3 indicate that additive noise at a level of 20 [dB] does not significantly reduce the detector performance.

For SNR below 20 [dB] the detectors performance can be improved by increasing the number of samples *N* processed. However, the cost of increasing *N* is to reduce the resolution (due to the filter effect) of the detectors, that is, the smallest defect that can be resolved. This effect could be countered by decreasing the crawler speed such that there are more rotor cycles per distance.

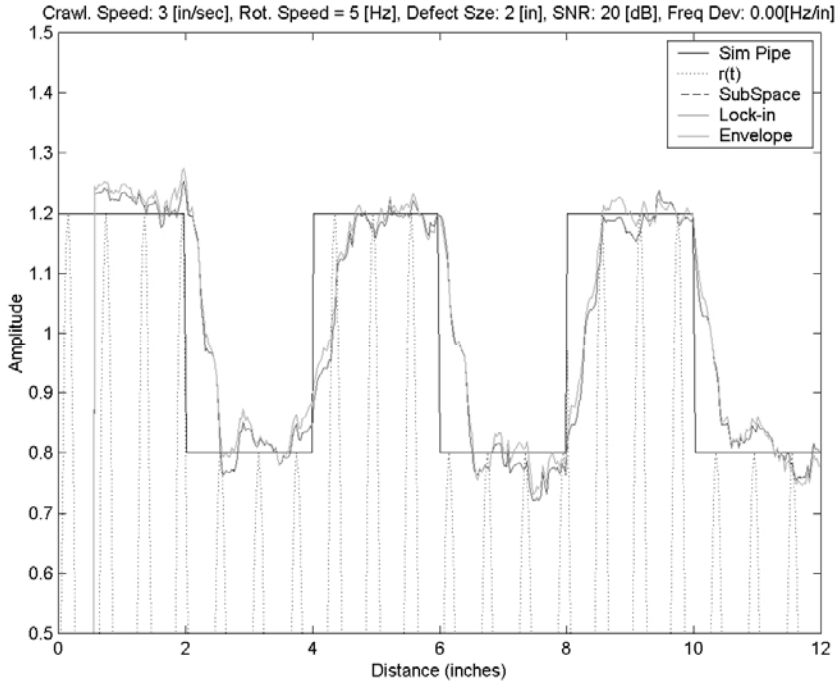

Figure B-3. Simulation 2 Results

SIM 3 – ADDITIVE NOISE – REDUCED CRAWLER SPEED. Figure B-4 shows the third simulation exploring the affect of additive noise and reduced crawler speed. In this case the crawler speed has been reduced and *N* has been increased to improve the detection performance while maintaining nearly the same detection resolution.

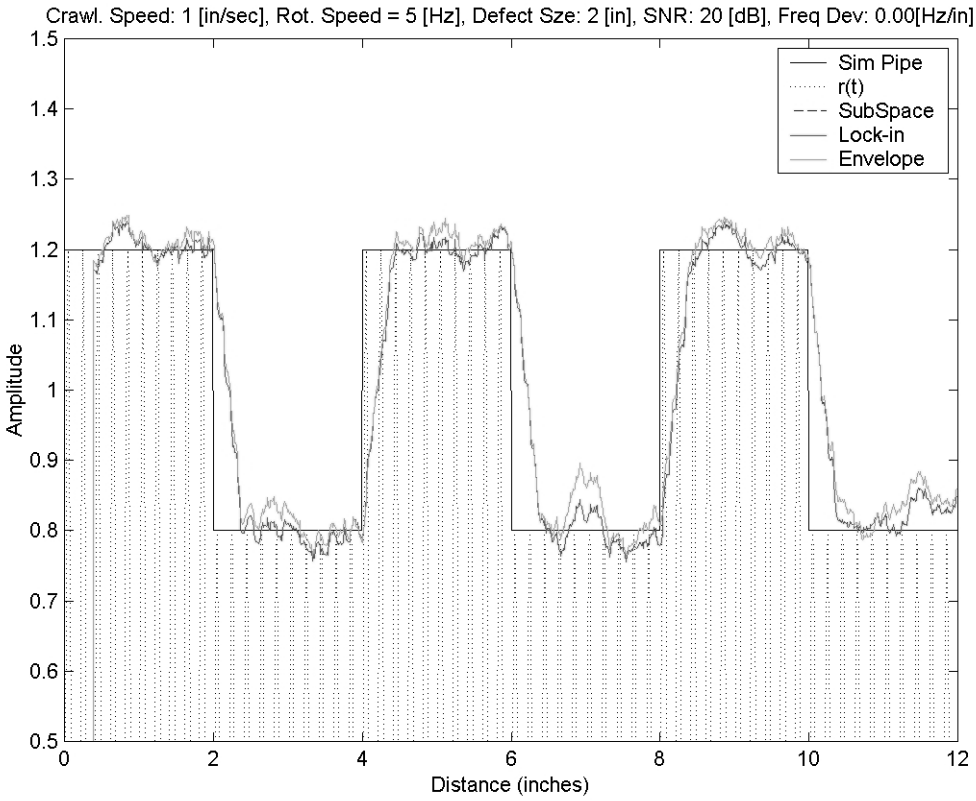

Figure B-4. Simulation 3 Results

SIM 4 – VARIABLE ROTOR SPEED. Figure B-5 shows the fourth simulation, exploring the affect of variable rotor speed**.** For this case there is no additive noise present in *x(t)*, instead we have allowed the rotor speed to deviate linearly as a function of distance along the pipe wall. For this case the deviation is .05 [Hz/in] which results in a 0.6 [Hz] frequency deviation from left to right in Figure B-5. In this case we are applying an update in the signal processing to accommodate the changing rotor speed. As can be seen, the frequency deviation does affect detector performance. The estimates of *A(t)* oscillate around the true value and the amplitude of oscillation is a function of how fast the rotor speed is changing. For the LIA and Subspace methods this is due to the use of the mean measured frequency for all *N* points to process the signals.

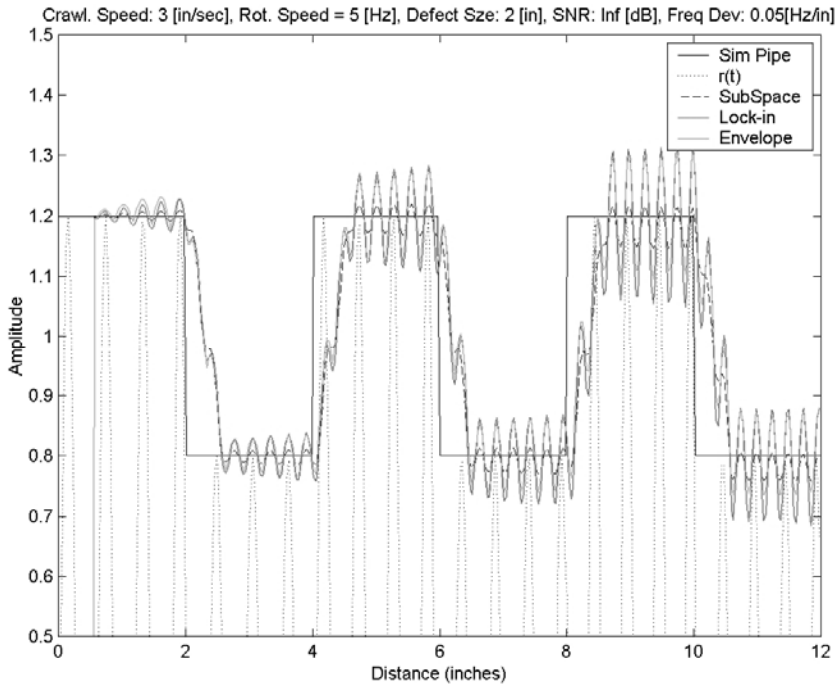

Figure B-5. Simulation 4 Results

SIM 5 – VARIABLE ROTOR SPEED AND REDUCED CRAWLER SPEED. Figure B-6 shows the fourth simulation, exploring the affect of variable rotor speed and reduced crawler speed**.** In this case we have reduced the crawler speed and are processing over two full cycles. As was expected the LIA and Subspace methods have degraded. Processing over more points means that there will be greater error between the mean measured frequency (which is used to process all N points) and the actually frequency of *r(t)* which is changing over all *N* points. An interesting observation is that the Envelope detector performance does improve. This is because the Envelope detector does not require the frequency measurement input. The envelope method requires no reference signal at all.

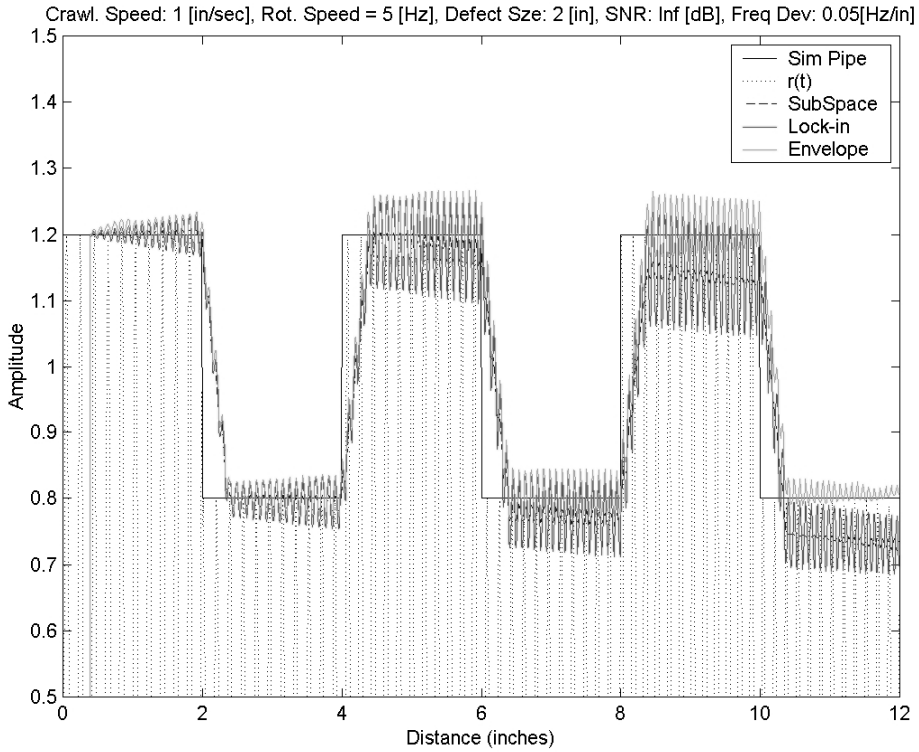

Figure B-6. Simulation 5 Results

SIM 6 – VARIABLE ROTOR SPEED AND ADDITIVE NOISE. Figure B-7 shows the results for both varying rotor speed and additive noise. All three methods achieve similar results. In fact for all of the cases presented here the results for each method are comparable. More analysis should be performed to investigate the limitations of each method. Based on the observations of this analysis the Envelope detection method would be preferred due to the simplicity of implementation and the lack of need for a reference input. However, we have made assumptions about *A(t)* that may not hold for real data.

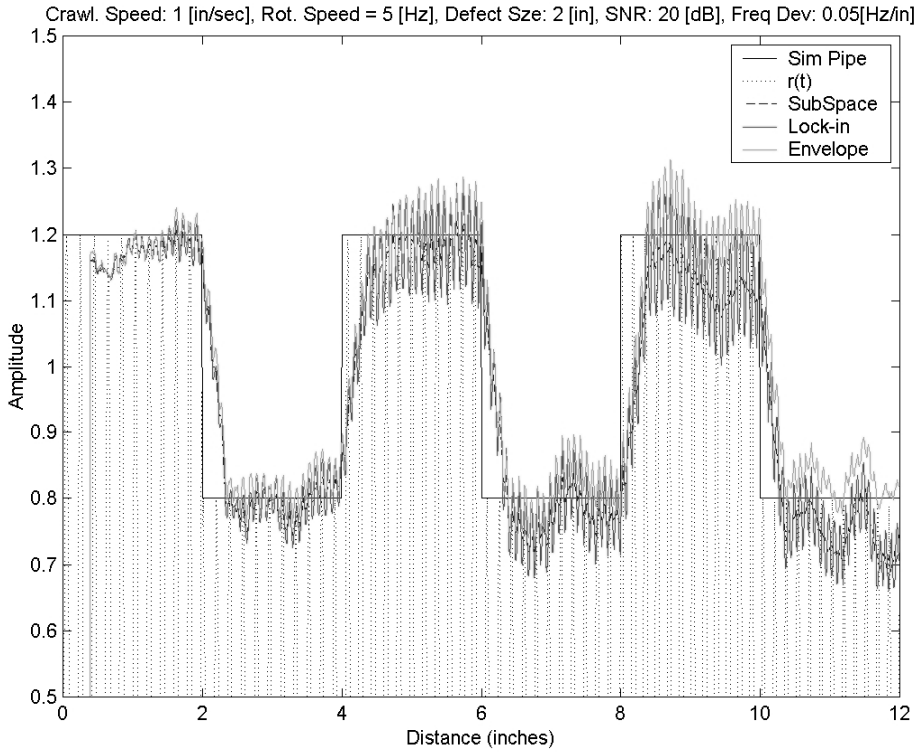

Figure B-7. Simulation 6 Results

APPENDIX C

Fundamental Studies of

Frequency and

Magnet Geometry

Using Seven Simple Metal Loss Anomalies

Appendix C
Fundamental Studies of Frequency and Magnet Geometry Using Seven Simple Metal Loss Anomalies

Experiments to gather data to investigate basic design parameters, including

1. Rotational frequency of the spinning magnet
2. Separation between the magnet and the inside of the pipe.
3. Size of the magnet

were conducted using the 8-inch diameter laboratory prototype system. To establish the optimum magnetizer geometry, a range of magnet lengths, widths, thicknesses and liftoffs were examined. The seven magnet configurations tested are given in Table C-1.

Table C-1. Optimization of magnet length, width, thickness, and liftoff variables

Length	Width	Thickness	Liftoff
(inches)			
2.0	1.0	0.5	0.5
1.0	1.0	1.5	0.5
1.0	1.0	1.5	1.0
1.0	1.0	0.5	0.5
1.0	1.0	0.5	1.0
1.0	0.5	0.5	0.5
1.0	0.5	0.5	1.0

The anomaly matrix was designed to investigate the effect of changing depths, lengths, and widths on the signal. The anomalies that were inspected during the development of this system are presented in Table C-2.

Table C-2. Range of Anomalies Evaluated

Anomaly	Depth	Length	Width
N1	30%	~1-inch	~3-inch
N2	70%	~1.25-inch	~3-inch
N3	50%	~1.125-inch	~3-inch
N4	50%	~1.125-inch	~2-inch
N5	50%	~2-inch	~2-inch
N6	50%	~1-inch	~1-inch
N7	50%	~3-inch	~1-inch

The raw data for the sensor with the maximum value of all 11 axial sensors was then plotted against the corresponding radial sensors raw data to produce the elliptical plots depicted in this Appendix.

The plots presented in Appendix C depict the maximum axial signal reading versus the corresponding radial signal reading over the range of rotational frequencies ranging from 3 to 20 hertz. The axial vs. radial plots are presented for the 7 different magnet configurations and 7

different anomalies evaluated in this experimental program. Plots of this nature are generally used to indicate if an anomaly has been detected for the specified magnet configuration and geometry. If the plot generates an elliptical pattern, the likelihood that an anomaly has been detected is good. Plots that do not generate an elliptical pattern when graphing the maximum axial and corresponding radial signals generally indicate that an anomaly has not been detected or is minor.

APPENDIX D

DATA FROM THE JANUARY 2006 BENCHMARKING

Appendix D
Data from the January 2006 Benchmark

The data collected during the benchmarking conducted in January 2006 are presented in two formats

- Amplitude time data waterfall plots for the axial and radial sensors and
- Axial versus radial plots with the maximum axial signal reading versus the corresponding radial signal reading

The 8 inch laboratory prototype system is configured with a 2-inch by 1-inch by 0.5-inch magnet configuration used during the benchmarking. Each plot has pictures of the anomalies evaluated during the benchmarking program. A blank indicates an area that does not have an anomaly. The axial radial plots are generally used to indicate if an anomaly is present. If the plot generates an elliptical pattern, the likelihood that an anomaly has been detected is good. Plots that do not generate an elliptical pattern when graphing the maximum axial and corresponding radial signals generally indicate that an anomaly has not been detected or is minor. The amplitude time plots were used for the sizing.

Several of the stronger signals from each anomaly were plotted from the 11 different axial and radial sensors used to collect data during the experimental pulls. Since the corrosion anomalies used in the benchmarking were irregular in shape it was not as straight-forward to select the maximum signal to determine the extent of the anomaly. Therefore several axial signals are plotted to determine trends in the signal strength and possible locations of deeper pitting. The plot in Figure 1 is an example showing the axial and radial signals for Defect p1-18, a 2-inch long 4-inch wide anomaly with a maximum depth of approximately 75 percent.

Defect p1-18:

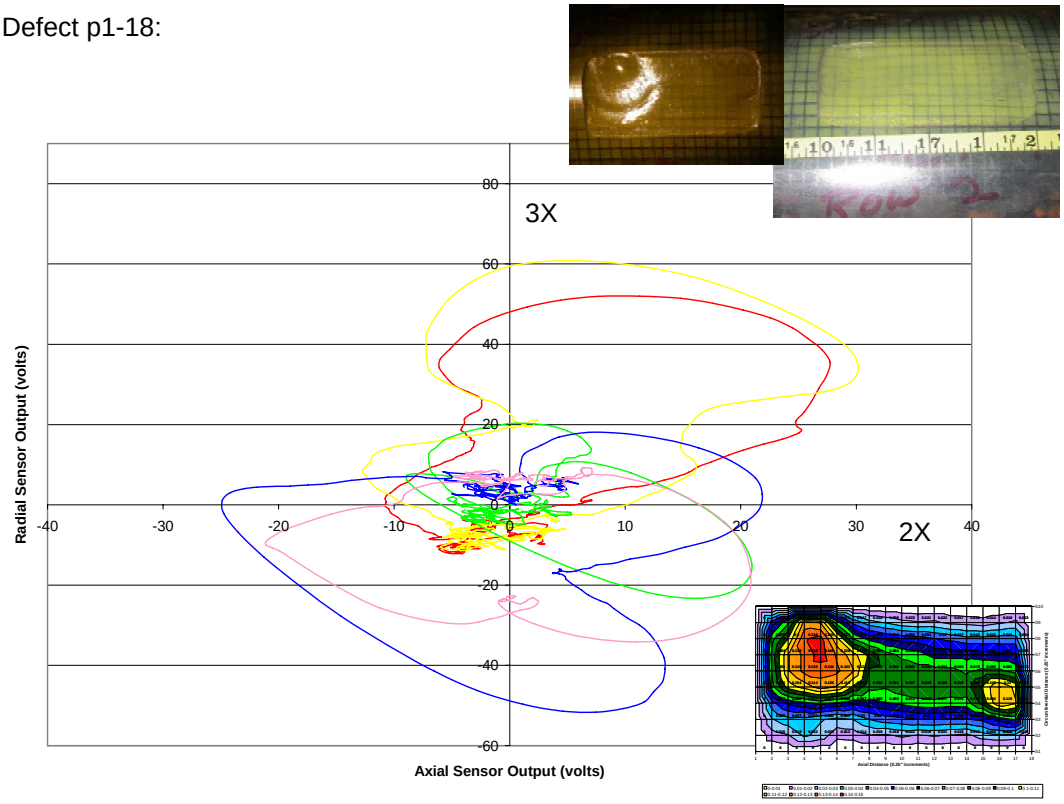

Figure D-1. Example Chart of Axial and Radial Signals for Defect p1-18

The raw data for several axial sensors were plotted against the corresponding radial sensors raw data to produce the elliptical plots depicted in this Appendix.